COHERENT FOURIER SCATTEROMETRY

Proefschrift

ter verkrijging van de graad van doctor aan de Technische Universiteit Delft, op gezag van de Rector Magnificus prof. ir. K. C. A. M. Luyben, voorzitter van het College voor Promoties, in het openbaar te verdedigen op maandag 1 december 2014 om 12.30 uur

door

Nitish KUMAR

Master of Science in Applied Physics geboren te Patna, India

Dit proefschrift is goedgekeurd door de promotor: prof. dr. H. P. Urbach

Copromotor Dr. S. F. Pereira

Samenstelling promotiecommissie:

Rector Magnificus. voorzitter prof. dr. H. P. Urbach, Delft University of Technology, promotor Dr. S. F. Pereira, Delft University of Technology, copromotor prof. dr. ir. L. J. van Vliet, Delft University of Technology prof. dr. W. M. J. Coene, Eindhoven University of Technology / ASML prof. dr. M. Kujawinska, Warsaw University of Technology Dr. ir. B. Bodermann, Physikalisch-Technische Bundesanstalt (PTB) prof. dr. X. C. Yuan, Shenzhen University

This research was supported by the Surface Physics for Advanced Manufacturing European project, within the FP7 Marie Curie Research and Initial Training Network Program (Project Number 215723) and by ASML.

Copyright © 2014 by N. Kumar

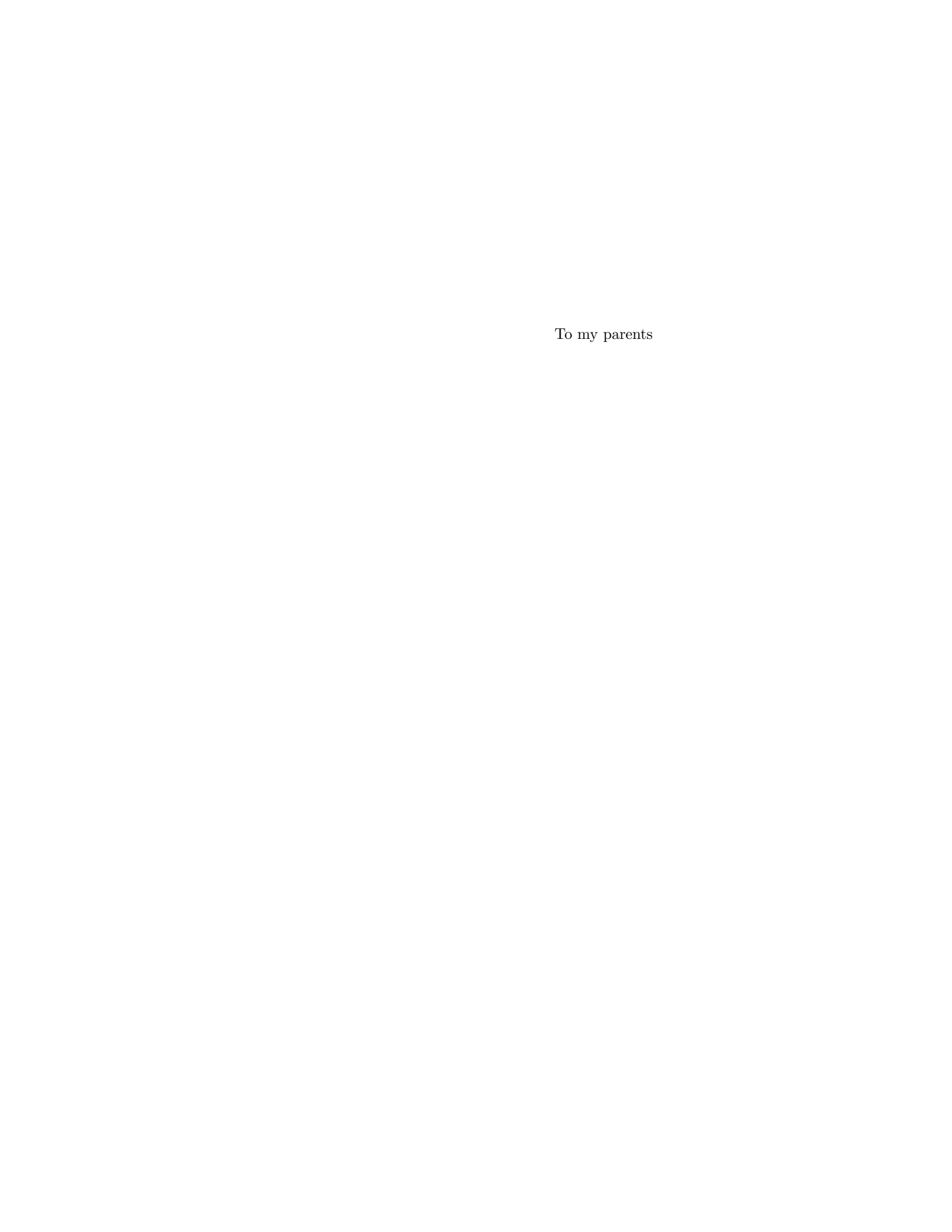
All rights reserved. No part of this publication may be reproduced, stored in a retrieval system or transmitted in any form or by any means: electronic, mechanical, photocopying, recording or otherwise, without prior written permission of the author.

ISBN 978-94-6259-468-5

Printed in the Netherlands by Ipskamp Drukkers, Enschede.

A free electronic version of this thesis can be downloaded from: http://repository.tudelft.nl

 $Author\ email:\ N. Nitishkumar-1@tudelft.nl,\ nitish.photonics@gmail.com$





Summary

The electronics which makes our lives easier like mobiles, computers, digital cameras contain chips with very small semiconductor components like transistors. When transistors can be made even smaller, the chip can accommodate a larger number of components, which gives more processing capacity, resulting in a faster device with an increased functionality. Industrial lithography, the art of making structures on wafers, follows Moores law (1970s), which states that the processor speed, or overall processing power for computers would double almost every two years, i.e., the number of transistors in an integrated circuit would double almost every two years. The implications of this law is clearly seen in the evolution of electronic devices where smaller, lighter and faster computers, high resolution imaging sensors, increased storage capacity are continuously being introduced in the market. But this also sets stringent requirements on lithography processes. The critical dimension printed on a wafer these days are in order of a few tens of nano-meters which in perspective is approximately 1000 times smaller than a strand of human hair.

The technology nodes and the uniformity of the line-width or critical dimension (CD) over the wafer as produced by lithographic scanners must be improved in future for an optimal yield and performance of the electronic components. Now, the question is how to design a measurement method that is able to quantify the printing quality of these small features in a fast, stable and non destructive way which can also be incorporated into the machine which makes these chips?

When you can measure something and express it in numbers, you know something about it. Lord Kelvin's statement is frequently paraphrased as "if you can measure something, you can make it better". The research work presented in the thesis is a step forward in that direction, regarding wafer inspection.

In the semiconductor industry, a robust, reliable and repeatable in-line control process is required to obtain the intended line shapes and sizes. This is achieved by printing special targets on the wafer, typically gratings, which are successively measured in order to adjust dose, exposure time, overlay/alignment and other relevant process parameters of the photo-lithographic machine. As the specifications get tighter, the measuring technique has to be more accurate. This is the primary reason for the continuous development of increasingly complex, advanced

and improved quantitative metrology techniques over the years. Currently, in the semiconductor industry, incoherent optical scatterometry (IOS) is the standard workhorse. Any degree of improvement in the present technique is worthwhile of scientific and technological interest.

In this thesis we develop, study, design and implement coherent Fourier scatterometry (CFS). The scatterometer is based on a coherent source of illumination, where a focused spot interacts with the sample. The performance of CFS is compared with IOS in terms of sensitivity to the change in grating shape parameters. The studies are done on grating as samples for the performance comparison. The grating reconstruction is proved with the experimental implementation of a CF scatterometer. Applications and improvements in CFS are also discussed in the thesis.

The thesis starts with an introduction to the research goals and scope of CFS in chapter 1. The grating diffraction formula, which predicts the angle of diffraction for a given incidence angle on the grating is explained and the relevance of rigorous coupled wave analysis popularly known as RCWA as a rigorous Maxwells solver for periodic structure are highlighted. A brief introduction to principle of the Shack-Hartmann sensor used in experiments is also mentioned. This chapter also contains a summarized description of the work done within the PhD period but are not in the scope of the description in the thesis.

In chapter 2 of the thesis, a framework to study the increment in sensitivity of CFS with respect to the IOS and the benefits of using a focused spot from a spatially coherent source (laser) is investigated on a theoretical viewpoint. A specific model of the grating and the illumination is presented, where the grating is defined in terms of a finite number of geometrical shape parameters (such as height, side-wall angles, midCD). The focused spot is scanned over the grating, and for each scan position, a far-field diffraction pattern is recorded. Through sensitivity analysis, we show that the use of coherence and multiple scanning makes CFS more sensitive than IOS under special circumstances. The role of the incident and output polarization, the position of the focused spot w.r.t. the grating and the effect of the number of scanning positions on the sensitivity analysis is also studied. There is an optimum number of scanning positions, which depends on the number of diffracted orders in the exit pupil.

Owing to the coherent illumination, the far field in CFS comprise phase information concealed in the complex reflection matrix of interaction. Intensity data with phase between scattered orders is the maximum information that can be extracted in CFS. Unravelling the complex reflection matrix in CFS requires the knowledge of the amplitude and phase of the individual components of the matrix. Intensity measurements provide the amplitude information but the phase information is absent. In chapter 3 of the thesis, we present a non interferometric partial phase retrieval method from the intensity measurements in CFS. The applicability of the principle of temporal phase shifting interferometry (TPSI) in CFS with a

scanning spot is presented. An analytical relation is derived and illustrated for the phase difference between two overlapping orders in the exit pupil. The analytic results are compared with the simulations from RCWA. Also, the polarization dependent phase sensitivity of grating parameters is studied for the overlap region of diffracted orders in the exit pupil.

In chapter 4, the implementation of an operational CFS instrument in the laboratory environment is reported for grating reconstruction. The setup is capable of illuminating and measuring the response of the sample simultaneously over a broad range of incident and reflected angles and for two orthogonal incident polarizations. The measurement for all radial and azimuthal angles can be performed within a few ms. The system, although currently operating at a relatively low numerical aperture (NA = 0.4) at wavelength 633 nm allows the reconstruction of the grating shape parameters with nano-meter accuracy, which is comparable to that of measured by atomic force microscopy (AFM) and scanning electron microscope (SEM) as the reference measurements. Additionally, nano-meter accuracy in lateral positioning is proven, which in the present used case corresponds to only 0.08% of the period of the grating.

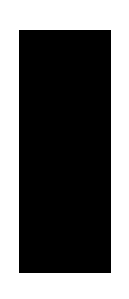
In semiconductor lithography, the desired pattern on the wafer is written layer by layer in several steps to realize the finished structure. The positional accuracy of new patterns on the existing ones decides the performance of the circuitry. Deviation of the consecutive layers is called overlay. The allowed deviation is $\leq 0.1\%$ of the critical dimension, which implies the measurement complexity. In chapter 5 of the thesis, a mathematical analysis of the overlay problem shows that the sum of the product of the reflection and transmission coefficients plays an important role in deciding the magnitude of the asymmetry signal. Here we observe that the overlay signal in CFS is larger in magnitude than that of IOS. With simulations, we have shown that CFS is more sensitive to the overlay as compared to an incoherent case. It is also inferred that, by pupil engineering for incident wavefront on the structure, the sensitivity of the overlay signal can be optimized for a given structure.

Optical resolution is limited by the incident wavelength and numerical aperture in a far field optical system. In principle, there are two principal parameters can be tuned to improve the resolution, either by decreasing the wavelength or by increasing the NA of the optical system. In chapter 6 of the thesis, we implement a micro solid immersion lens (SIL) to improve the resolution in a scanning near field microscope setup. Numerical and experimental results show the increased resolution, the improvement in the resolution is based on the focused spot size and visibility studies in the SIL based microscope compared to the confocal imaging. It has been shown that micro-SIL can be used for metrology applications with high NA requirement. The idea, implementation and challenges associated with a Fourier scatterometer with a micro-SIL is presented in the chapter.

The fabrication process for the grating involves chemical and plasma treatment

which can seldomly result in an unwanted surface over-layer on the nominal structure. When the feature size of the grating is in few tens of nano-meters, an additional layer of few nano-meters on the grating is expected to change the far field diffraction of the grating, compared to an absence of the surface over-layer. In CFS the shape parameters are determined inversely from the far field intensity in grating reconstruction. In the chapter 7 of the thesis, assuming that the distribution of the surface layers (for example: native silicon oxide, contamination and traces of resist removal) are identical on the wafer area with and without the structure, the effect of the thickness of oxide layer on the Si-etched grating is studied and investigated using inverse grating reconstruction. Optical properties of the surface over-layer are measured by ellipsometry and the error, and the accuracy in grating parameters reconstruction in presence of an oxide layer is presented. Finally the grating parameters reconstruction shows that effect of the surface over-layer is crucial for the determination of right set of grating parameters. The accuracy in determination of the refractive index of the over-layer is a critical issue for the actual height determination of the over-layer. Once determined, then CFS is able to resolve few nano-meters of unintentional surface over-layer on the grating structure.

Although the studies in the thesis are carried out for periodic structures such as gratings, the applications of CFS are not limited to periodic structures but can also can be applied to multilayer structures analysis, material sciences, photonics industry, bio-sensing, detection of isolated structures and other forms of non-contact metrology. Nevertheless, CFS can also be extended to the interferometric Fourier scatterometry and the ellipsometric Fourier scatterometry with slight modification in the design of the scatterometer for additional functionality and increased sensitivity.



Samenvatting

De elektronica die ons het leven gemakkelijker maakt, zoals mobiele telefoons, computers en digitale camera's, bevatten chips met zeer kleine halfgeleider onderdelen zoals transistors. Wanneer transistors nog kleiner kunnen worden gemaakt, kan de chip meer componenten bevatten, waardoor die meer verwerkingskracht krijgt, met als gevolg een sneller apparaat met meer functionaliteit. Industriële lithografie, de kunst van structuren aanbrengen op wafers, volgt de Wet van Moore, die zegt dat de processorsnelheid, of het totale processorvermogen voor computers bijna elke twee jaar verdubbelt, d.w.z. dat het aantal transistors op een geïntegreerde schakeling bijna elke twee jaar verdubbelt. De gevolgen van deze wet zijn duidelijk te zien in de ontwikkeling van elektronische apparaten, waarbij continu kleinere, lichtere en snellere computers, hoge-resolutie beeldsensoren, en vergrote opslagcapaciteit op de markt gebracht worden. Echter, dit brengt ook strengere eisen voor het lithografieproces met zich mee. De kritieke afmeting die tegenwoordig op een wafer geprint kan worden ligt in de ordegrootte van enkele tientallen nanometers, hetgeen, om het in perspectief te plaatsen, 1000 keer kleiner is dan een mensenhaar.

De technology nodes en de uniformiteit van de lijnbreedte of kritieke afmeting (CD, critical dimension) over de wafer zoals geproduceerd door lithografische scanners moeten in de toekomst verbeterd worden voor een optimale opbrengst en prestatie van elektronische componenten. De vraag is nu hoe een meetmethode kan worden ontworpen, die de printkwaliteit van deze kleine kenmerken snel, stabiel en niet-destructief kan kwantificeren, en bovendien kan worden geïntegreerd in het apparaat dat deze chips produceert.

Als je iets kunt meten en uitdrukken in getallen, dan weet je er iets van. Een uitspraak van Lord Kelvin die vaak wordt geparafraseerd als: 'Als je iets kunt meten, dan kan je het verbeteren'. Het onderzoek dat in dit proefschrift gepresenteerd wordt is een stap in die richting, met betrekking tot inspectie van wafers.

In de halfgeleiderindustrie is een robuust, betrouwbaar, inline controleproces vereist om de gewenste lijngroottes en -vormen te verkrijgen. Dit wordt bereikt door speciale merktekens op de wafer te printen, voornamelijk diffractieroosters, die opeenvolgend gemeten worden om de dosis, belichtingstijd, positionering/uitlijning en andere relevante parameters van het fotolithografie-apparaat bij te stellen. Als de specificaties strenger worden, moet de meettechniek nauwkeuriger worden. Dit is

de voornaamste reden dat al jarenlang voortdurend complexere, geavanceerdere and verbeterde kwantitatieve methoden in de metrologie ontwikkeld worden. Momenteel is incoherente optische scatterometrie (IOS) in de halfgeleiderindustrie het standaard werkpaard. Elke mate van verbetering van de huidige techniek is van wetenschappelijk en technologisch belang.

In dit proefschrift wordt coherente Fourier scatterometrie (CFS) ontwikkeld, bestudeerd, ontworpen en geïmplementeerd. De scatterometer is gebaseerd op een coherente belichtingsbron, waarbij interactie plaats vindt tussen gefocusseerd licht en het sample. De prestaties van CFS worden vergeleken met die van IOS in termen van gevoeligheid voor veranderingen in de vormparameters van het diffractierooster. Om de prestaties te vergelijken wordt onderzoek gedaan met roosters als samples. Reconstructie van het rooster wordt gedemonstreerd met de experimentele implementatie van een CF scatterometer. Tevens worden in dit proefschrift toepassingen en verbeteringen van CFS besproken.

Het proefschrift begint met een introductie van de onderzoeksdoelen en de omvang van CFS in hoofdstuk 1. De formule voor roosterdiffractie, die de diffractiehoek voorspelt voor een gegeven invalshoek met het rooster, wordt uitgelegd, en aan het belang van rigoureuze gekoppelde-golf analyse, wat bekend staat als RCWA (rigorous coupled wave analysis), als rigoureuze Maxwell solver voor periodieke structuren wordt speciale aandacht gegeven. Verder wordt een korte inleiding gegeven over het principe van Shack-Hartmann sensors die worden gebruikt in de experimenten. Dit hoofdstuk bevat ook een samenvattende beschrijving van het werk dat gedurende de PhD-periode gedaan is, maar dat niet binnen het kader van de beschrijving in dit proefschrift valt.

In hoofdstuk 2 van het proefschrift wordt beschreven hoe vanuit een theoretisch standpunt de toename van de gevoeligheid van CFS ten opzichte van die van IOS kan worden onderzocht, en wat de voordelen zijn van het gebruik van een spatieel coherente bron (laser). Er is een specifiek model opgesteld van het rooster en de belichting, waarbij het rooster gedefinieerd is in termen van een eindig aantal parameters die de geometrische vorm beschrijven (zoals hoogte, hoeken van de zijwanden, midCD). De gefocusseerde spot wordt over het rooster gescand, en voor elke scanpositite wordt het diffractiepatroon in het verre veld opgenomen. Met gevoeligheidsanalyse tonen we aan dat door het gebruik van coherentie en meervoudig scannen CFS onder bijzondere omstandigheden gevoeliger is dan IOS. De rol van de invallende en uitgaande polarisatie, de positie van de gefocusseerde spot ten opzichte van het rooster, en het effect van het aantal scanposities op de gevoeligheidsanalyse wordt eveneens bestudeerd. Er is een optimaal aantal scanposities, hetgeen afhangt van het aantal diffractieordes in de uitgangspupil.

Dankzij de coherente belichting bevat het verre veld in CFS fase-informatie die verborgen zit in de complexe reflectiematrix van de interactie. De maximale hoeveelheid informatie die met CFS kan worden verkregen bestaat uit intensiteitsdata en uit faseverschillen tussen tussen de verschillende diffractieordes ordes. Het onrafe-

len van de complexe reflectiematrix in CFS vereist kennis van de amplitude en fase van de afzonderlijke componenten van de matrix. Intensiteitsmetingen geven informatie over de amplitude, maar de informatie over de fase ontbreekt. In hoofdstuk 3 van het proefschrift presenteren we een niet-interferometrische methode waarmee een deel van de fase-informatie wordt verkregen uit de intensiteitsmetingen in CFS. De toepasbaarheid van temporeel fase-stappende interferometrie (TPSI) voor CFS met een scannende spot wordt gepresenteerd. Een analytisch verband wordt afgeleid en geïllustreerd voor het faseverschil tussen twee overlappende ordes in de uitgangpupil. De analytische resultaten worden vergeleken met simulaties van RCWA. Ook wordt de polarisatie-afhankelijke fasegevoeligheid van roosterparameters bestudeerd voor het overlappingsgebied van diffractieordes in de uitgangspupil.

In hoofdstuk 4 wordt de implementatie van een operationeel CFS instrument in een laboratoriumomgeving voor roosterreconstructie gerapporteerd. De opstelling is in staat om tegelijkertijd het sample te belichten en de respons ervan te meten voor een breed bereik van invalshoeken en reflectiehoeken, en voor twee orthogonale polarisaties van invallend licht. De meting voor alle radiale en azimutale hoeken kan worden uitgevoerd in enkele milliseconden. Hoewel het systeem momenteel werkt met een relatief kleine numerieke apertuur (NA=0.4) met een golflengte van 633 nm, kunnen er roosterparameters mee worden gereconstrueerd met nanometer nauwkeurigheid, hetgeen vergelijkbaar is met wat gemeten wordt met atoomkrachtmicroscopie (AFM, atomic force microscopy) en rasterelektronenmicroscopie (SEM, scanning electron microscopy) als referentiemetingen. Bovendien is nanometer nauwkeurigheid in laterale positionering aangetoond, wat in de huidige situatie overeenkomt met slechts 0.08% van de roosterperiode.

In halfgeleiderlithografie wordt het gewenste patroon laag voor laag op de wafer geschreven om zo de uiteindelijke structuur te realiseren. De prestatie van de geïntegreerde schakeling wordt bepaald door de nauwkeurigheid waarmee nieuwe patronen op de reeds aanwezige kunnen worden gepositioneerd. De afwijking tussen opeenvolgende lagen wordt overlap genoemd. De toegestane afwijking is $\leq 0.1\%$ van de kritieke afmeting, hetgeen een indicatie vormt voor de complexiteit van de meting. In hoofdstuk 5 van dit proefschrift laat een wiskundige analyse van het overlapprobleem zien dat de som van het product van de reflectie- en transmissiecoëfficienten een belangrijke rol speelt in het bepalen van de magnitude van het asymmetriesignaal. Hier zien we dat het overlapsignaal in CFS groter is in magnitude dan dat van IOS. Met behulp van simulaties hebben we laten zien dat CFS gevoeliger is voor overlap dan in het incoherente geval. Er wordt ook afgeleid dat de gevoeligheid voor het overlapsignaal geoptimaliseerd kan worden voor een gegeven structuur door het golffront dat invalt op de structuur te manipuleren (pupil engineering).

De optische resolutie in een verre-veld optisch systeem wordt beperkt door de invallende golflengte en de numerieke apertuur. In principe zijn er twee voornaamste parameters die bijgesteld kunnen worden om de resolutie te verbeteren: ofwel de golflengte kan worden verkleind, of de numerieke apertuur (NA) van het optische systeem kan worden verhoogd. In hoofdstuk 6 van het proefschrift implementeren we een micro-vaste-immersielens (SIL, solid immersion lens) om de resolutie van een opstellingvoor scanning nabije-veld microscopie te verbeteren. Numerieke en experimentele resultaten laten verbetering in de resolutie zien, gebaseerd op de grootte van de gefocusseerde spot en zichtbaarheidsonderzoeken in de SIL-gebaseerde microscoop vergeleken met confocale beeldvorming. Er is aangetoond dat micro-SIL kan worden gebruikt in metrologietoepassingen waarbij een hoge NA vereist is. Het idee, de implementatie en de uitdagingen behorend bij een Fourier scatterometer met een micro-SIL worden in dit hoofdstuk gepresenteerd.

Het fabricatieproces voor het rooster omvat chemische- en plasmabehandeling, hetgeen sporadisch resulteert in een ongewenste afdeklaag op de nominale structuur. Wanneer de feature size van het rooster enkele tientallen nanometers groot is, mag worden verwacht dat een laag van enkele nanometers op het rooster leidt tot een verandering van het diffractiepatroon van het rooster in het verre veld in vergelijking met het geval dat er geen afdeklaag is. In CFS worden tijdens de reconstructie van het rooster de vormparameters van het rooster bepaald door een inverse operatie op de intensiteitsverdeling in het verre veld. In hoofdstuk 7 van het proefschrift wordt het effect van de dikte van de oxidelaag op het Si-etched rooster bestudeerd, gebruik makend van inverse reconstructie van het rooster en onder aanname dat er geen verschil is tussen de verdeling van de oppervlaktelagen (bijvoorbeeld: oorspronkelijk siliciumoxide, vervuiling en sporen van verwijdering van resist) voor het waferoppervlak met en zonder het rooster. De optische eigenschappen van de afdeklaag worden gemeten met ellipsometrie en de fout, nauwkeurigheid van de reconstructie van de roosterparameters in de aanwezigheid van een oxidelaag wordt gepresenteerd. Tot slot laat de reconstructie van de roosterparameters zien dat het effect van de afdeklaag cruciaal is voor de reconstructie van de juiste set roosterparameters. De nauwkeurigheid van het bepalen van de brekingsindex van de afdeklaag is een kritiek punt voor het bepalen van de daadwerkelijke hoogte van de afdeklaag. Zodra deze is bepaald, is CFS in staat om een onbedoelde afdeklaag van enkele nanometers dik op de roosterstructuur te onderscheiden.

Hoewel de onderzoeken in dit proefschrift zijn uitgevoerd voor periodieke structuren zoals roosters, blijven de toepassingen van CFS niet beperkt tot periodieke structuren; CFS kan ook worden toegepast bij analyse van meerlaagsstructuren, in de materiaalwetenschappen, fotonica-industrie, bio-sensing, detectie van alleenstaande structuren en andere vormen van contactloze metrologie. Desalniettemin kan CFS ook uitgebreid worden naar interferometrische Fourier scatterometrie en naar ellipsometrische Fourier scatterometrie met kleine wijzigingen in het ontwerp van de scatterometer voor extra functionaliteit en verhoogde gevoeligheid.

Contents

Sı	ımm	\mathbf{ary}		\mathbf{v}
Sa	men	vatting	y o	ix
\mathbf{C}	ontei	$_{ m nts}$		xiii
1	Inti	oducti	ion	1
	1.1	Resear	rch goals, scope and the background	1
	1.2	Gratin	ng equation and propagating orders	2
	1.3	Rigoro	ous Coupled Wave Analysis (RCWA)	4
	1.4	Shack-	-Hartmann sensor	5
	1.5	Paralle	el work on the PhD timeline	6
		1.5.1	Demonstration of an optimised focal field with long focal depth and high transmission obtained with the Extended	
			Nijboer-Zernike theory	6
		1.5.2	Through-focus phase retrieval and its connection to the spatial correlation for propagating fields	6
		1.5.3	Experimental and numerical analysis of the super resolution near-field effect on an InSb sample	7
	1.6	Outlin	ne of the thesis	7
2	Per	formar	nce analysis of coherent Fourier scatterometry	9
	2.1	Abstra	act	10
	2.2	Introd	uction	11
	2.3	Model	of the grating	11
	2.4	Sensit	ivity analysis: Model and theory	13
	2.5	Effect	of scanning in CFS \hdots	14
	2.6	Estima	ated uncertainties: Simulations	16
		2.6.1	Effect of coherent illumination: polarization dependence	17
		2.6.2	Polarization dependent sensitivity	24
		2.6.3	Bias dependent CFS gain	26
	2.7	Concli	usions	29

	hase retrieval between overlapping orders in coherent Fouri atterometry				
3.1	1 Abstract				
3.2					
3.3	v				
	3.3.1 Pupil points with no overlapping orders				
	3.3.2 Pupil points where reflected orders overlap				
	3.3.3 Summary				
3.4	4 Phase difference between overlapping orders				
3.5	ı ı v				
3.6	r · · · · · · · · · · · · · · · · · · ·				
3.7	7 Discussion and Conclusions				
	Reconstruction of sub-wavelength features and nano-positionin				
	gratings using coherent Fourier scatterometry				
4.1					
4.2					
4.3	3 3/				
4.4	8				
4.5	r · · · · · · · · · · · · · · · · · · ·				
4.6					
	4.6.1 From CCD parameters to sample space: Through scaling in				
	Fourier domain				
	4.6.2 Role of the telescopic system				
4.7					
	4.7.1 Diffracted far field intensity maps				
	4.7.2 Bias correlation				
	4.7.3 Model based optimization				
	4.7.4 Parameters reconstruction and discussion				
4.8	8 Conclusions				
	iffraction based overlay analysis in coherent Fourier scatteror				
	ry				
5.1					
5.2					
5.3					
5.4	y				
	5.4.1 Complex amplitude from grating stacks:				
	Mathematical foundation				
	5.4.2 Symmetry-based relations				
	5.4.3 Asymmetry signal				
5.5	v v o				
	5.5.1 Complex amplitude of diffracted orders for multiple coherent				
	incident plane waves				
	5.5.2 Summary				
5.6	6 Simulations				

		5.6.1 Individual grating model	82				
		5.6.2 Rigorous simulations for real overlay target	83				
	5.7	Conclusions	84				
6	A no	plication of μ -solid immersion lens in coherent Fourier scat-					
U		phration of μ -solid infinersion lens in coherent Fourier scat- pmetry	- 85				
	6.1	Abstract	86				
	6.2	Introduction	87				
	6.2	Solid immersion lens	87				
	0.5	6.3.1 Focal spot measurement of a μ -SIL	90				
		- · · · · · · · · · · · · · · · · · · ·	92				
	6.4	6.3.2 Visibility studies	95				
	0.4		95 96				
	6.5	F	90 97				
	0.5	Conclusions	91				
7	Rec	construction of unintentional surface over-layer on Si grating	99				
	7.1	Abstract	100				
	7.2	Introduction	101				
	7.3	Native oxide over-layer effect	101				
	7.4	Characterization and reconstruction	106				
		7.4.1 Ellipsometry measurement	107				
		7.4.2 Reconstruction	110				
	7.5	Conclusions	112				
8	Cor	Conclusions and Outlook 113					
	8.1	Conclusions	113				
	8.2	Remarks and Future works	115				
		8.2.1 Interferometric CFS	115				
		8.2.2 Ellipsometric CFS	115				
		8.2.3 Pupil engineering in CFS	116				
٨	Bu	eket algorithm for analytical reconstruction of the phase dif-					
А		ence of overlapping orders	117				
В	Exp	perimental laboratory setup	119				
A	ckno	wledgements	129				
Αl	oout	the Author	131				

Introduction

1.1 Research goals, scope and the background

The research presented in the thesis has been carried out towards the goal of improving the current wafer metrology capabilities. This is done by introducing a new technique in order to solve some of the problems associated with chip making industry requirements. During any lithographic process, a good alignment and overlay among the layers in the wafer is required to get, possibly, reduced critical dimensions (CD), in order to improve speed performances and storage capabilities of microelectronic circuits. This work was done under the European funded project called Surface Physics for Advanced Manufacturing (S. P. A. M) within FP7 Marie-Curie research and initial training program and by ASM lithography, The Netherlands.

The demand for faster, smaller, lighter and, at the same time, high-data density electronic devices sets stringent requirements for nano-lithography, the science of writing small features into a photo-sensitive resist layer on top of a silicon wafer [1]. Already for the current 45 and 32 nm technology nodes, the uniformity of the linewidth or CD over the wafer as produced by lithographic scanners must be improved for an optimal yield and performance of the electronic components. In order to obtain the intended line shapes and sizes, a reliable in-line process control has to take place. This is achieved by printing special targets on the wafer, typically gratings, which are successively measured in order to adjust dose, exposure time, overlay/alignment and other relevant process parameters of the photo-lithographic machine [2,3]. Currently, the metrology task of this process control is achieved by means of Incoherent Optical Scatterometry (IOS).

Scatterometry is an optical dimensional metrology technique based on the light scattered from the object. In this technique, which is a very well established method for the inspection of periodic structures like gratings, an incoming beam is shone on the target and the part of the light which is scattered by it in reflection mode, is measured in the far field. Given some a priori knowledge of the target, one can achieve a high accuracy in the reconstruction of the shape of the grating. The advantage over other competing inspection techniques, such as imaging, Scanning Electron Microscopy (SEM) or Atomic Force Microscopy (AFM), is that IOS is a rapid, quantitative and non destructive technique which does not suffer

from the Rayleigh diffraction limit, is easily integrable in a lithographic machine. In contrast to near field techniques, where the probe and the signal from the sample are strongly coupled, the far field detection makes the interpretation of the data less complicated (but still non-linear), since any significant coupling between the optical probe, the target and the detector is completely absent. But, such advantages also have a price. In fact, scatterometry falls into the category of inverse problems in electromagnetism, which are known for being severely ill-posed. The inverse problem is to deduce the features of the scatterer from the detection of the scattered radiation. It occur in many other branches of science and technology as well. Ill-posedness in this context means that the successful reconstruction of grating parameters from the far field if possible may or may not be unique and stable [4,5]. This implies that even a very precise and accurate experimental far field signal does not always provide enough information content for reconstruction. It is the presence of some a priori information (as for example an approximate grating structure) that enormously reduces the impact of the ill-posedness and makes scatterometry feasible in practice.

Many variations of the idea behind a scatterometer have emerged in the last decades [6]. Some of the most widely used configurations are single incidence angle reflectometry, 2-Θ scatterometry, spectroscopic ellipsometry, Fourier scatterometry, interferometric Fourier scatterometry [7–13] with a wide range of applications [14–18]. In this thesis we present another scatterometry approach based on coherent light. This method named coherent Fourier scatterometry (CFS) has advantage of being more sensitive than currently used incoherent optical scatterometry method in lithography. In addition, CFS is not limited to measuring periodic structures but can be applied to multilayer structures analysis, material sciences, photonics industry, bio-sensing, detection of isolated structures and other forms of non-contact metrology.

1.2 Grating equation and propagating orders

When a grating is illuminated by an incident field, it gives rise to several diffracted orders either propagating in different directions or the evanescent ones. To compute the scattered energy in diffracted orders, one needs a rigorous Maxwell solver, but the direction of diffraction of propagating orders can be derived in a straightforward way.

Figure 1.1 shows a plane wave with wave vector (k^i) incident at a polar angle θ_0 and azimuthal angle Ψ on the grating. In Fig. 1.1, the incident plane wave is linearly polarized. For $\Psi=0$, the case of planar diffraction, the incident polarization can be decomposed into TE $(\phi=\pi/2)$, the incident electric field oscillates in the direction normal to the field of incidence) and TM $(\phi=0)$, the incident electric field oscillates in the plane of incidence) respectively. For the case $\Psi\neq 0$, it is called conical diffraction and the diffracted orders from the grating lie on the surface of a cone. Let a one dimensional grating with period Λ be illuminated by a plane wave of amplitude A_0 ($\Psi=0$, planar incidence). In this case the incident

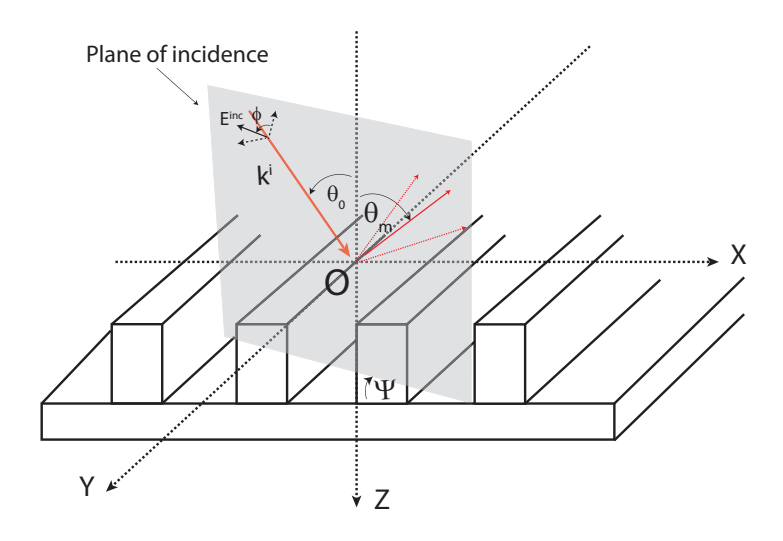


Figure 1.1: Plane wave incident on the grating at a polar angle θ_0 and azimuthal angle Ψ . The incident field with wave-vector k^i is decomposed into two orthogonal polarizations in TE ($\phi=\pi/2$, the incident electric field oscillates in the direction normal to the field of incidence) and TM ($\phi=0$, the incident electric field oscillates in the plane of incidence) respectively. θ_m is the angle of m^{th} diffracted order.

wave-vector lies in the xz plane, described by

$$E(x,z) = A_0 \exp\left[i\left(k^i x \sin\theta_0 + k^i z \cos\theta_0\right)\right],\tag{1.1}$$

The incident wave-vector lies in the xz plane. Here all the diffracted orders lie in the same plane. The grating is periodic along the x-axis and the grating is infinite along the y-axis. Within the reflection model, the grating can be modeled by,

$$r(x,y) = \sum_{m=-\infty}^{\infty} \hat{r}_m \exp\frac{i2\pi mx}{\Lambda},$$
(1.2)

where \hat{r}_m 's are the Fourier coefficients of r(x, y). For planar incidence, the wave vector of the diffracted fields does not contain the y-component. After interaction of the incident field and the grating, the field above the grating is,

$$U(x,y) = A_0 \sum_{m=-\infty}^{\infty} \exp\left[i\left(k^i \sin\theta_0 + \frac{2\pi m}{\Lambda}\right)x\right]. \tag{1.3}$$

From Eqn. 1.3, it follows that the total diffracted field is the sum of many individual fields with wave vector $(k^m = k_x^m, 0, k_z^m)$ diffracted in different directions depending upon the incidence angle θ_0 such that,

$$k^{m}\sin\theta_{m} = k^{i}\sin\theta_{0} + \frac{2\pi m}{\Lambda},\tag{1.4}$$

where $m = 0, \pm 1, \pm 2 \pm 3...$ is an integer. The direction of propagation of the m^{th} diffracted order is given by the Braggs law,

$$\sin \theta_m = \sin \theta_0 + m \frac{\lambda}{\Lambda}. \tag{1.5}$$

Here λ is the incident wavelength on the grating. Not all the diffracted orders are propagating orders. Only a finite number of diffracted orders satisfying the separation condition (Eqn. 1.6) propagate:

$$k_z^m = \sqrt{k^2 - (k_x^m)^2}. (1.6)$$

where $k = \frac{2\pi}{\lambda}$. When $k_x^m \leq k$, k_z^m are real, there exists propagating orders and when $k_x^m \geq k$, k_z^m are complex, giving rise to evanescent orders. Also, it can be seen from Eqn. 1.5 that the number of propagating orders depends on the ratio of incident wavelength to the period of the grating. This sets the minimum period of the grating, where the higher diffraction order exists at a given wavelength of incidence. For example, for the normal incidence on the grating $(\theta_0 = 0)$, the minimum period of the grating the light can see is λ , and for grazing incidence $(\theta_0 = 90^\circ)$, the minimum period of the grating which light can see is $\lambda/2$. When the period of the grating is larger then the incident wavelength, scalar theory can predict the complex amplitude of the diffracted orders. In grating theory, this is characterized by diffraction efficiency. For periods of the grating smaller or equivalent to the incident wavelength, one needs a rigorous approach to predict the complex amplitude of the m^{th} diffracted order.

1.3 Rigorous Coupled Wave Analysis (RCWA)

Rigorous computation of light interaction with periodic media is useful in numerous physical and engineering applications. There are several computational numerical modeling methods to solve the full electromagnetic problem of the light-grating interaction. RCWA is one of these methods particularly suited to compute the diffraction efficiency from periodic structures. The method was first developed for the rectangular structure but it was later extended to general shapes. RCWA algorithm is often used because of its good convergence and relatively simple implementation. The development, issues with implementation, speed and convergence of RCWA method can be found in Refs. [19–22].

RCWA rigorously solves Maxwell equations for periodic refractive index variation, by expressing it in a finite Fourier series. The idea is to divide the given structure into layers of rectangular stack. Each layer has different work cycle from the adjacent one, thereby realizing the shape of the final structure in form of discrete steps. Rectangular layer structure of the grating allows separation of space variables and by using Fourier expansion for the space periodic part of the solution, the problem described by the partial differential equation is transformed into ordinary differential equations for the Fourier amplitudes. The accuracy of RCWA is defined by the number of terms retained in the expansion. Maxwell equations are solved in any of these homogenous sub-domains and a collection of continuity and boundary conditions are applied. Also, all radiating fields should satisfy Sommerfeld's

condition [23]. The field above and below the grating is expressed in Rayleigh's expansion. For instance, the reflected field is expressed as,

$$E^{r}(r) = \sum_{m} R_{m} \exp\left[i\left(\tilde{k}_{y}y + \tilde{k}_{x}x - \tilde{k}_{z}z\right)\right]. \tag{1.7}$$

RCWA evaluates the coefficients R_m . In this thesis we use the modified routine which uses the basic kernel of RCWA from ASML, Veldhoven, which is an implementation of the method presented in [24] (also called Fourier Modal Method). To implement the focused spot interaction with the grating, a lens is used as a focusing element and we work with reflected fields, where the same lens is used for focusing and collecting the reflected light from the grating. The algorithm distinguishes between the X (TM) and Y (TE) polarization of the incident field above the focusing lens.

1.4 Shack-Hartmann sensor

To compute the diffracted far field of the grating and match it with the experimentally obtained far fields, the knowledge of the incident electromagnetic field is important. In order to obtain an accurate measurement of the field distribution both amplitude and phase, we apply a wavefront measurement technique based on the Shack-Hartmann principle (see Fig. 1.2) [25]. The device used to measure the wavefront is called Shack-Hartmann sensor (SHS). A SHS sensor consists

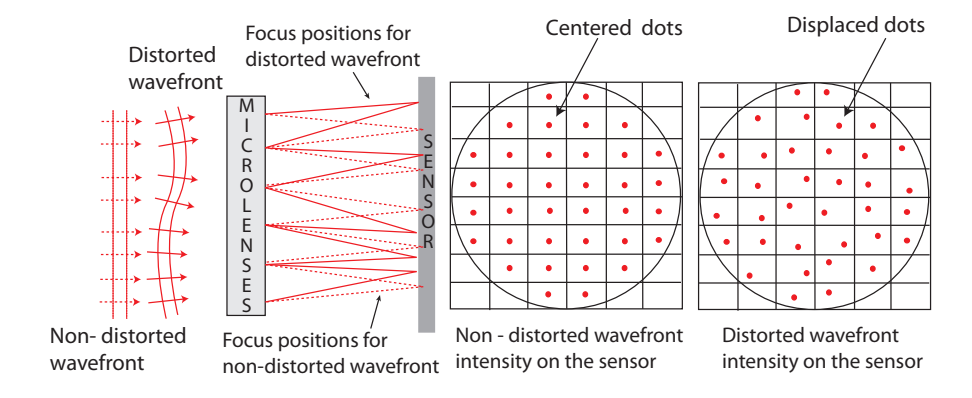


Figure 1.2: Schematic of a microlens array focusing a non-distorted and distorted wavefront on the CCD sensor.

of an array of micro-lenses, which divides the incident wavefront into many subdomains. Each sub-domain corresponds to the focused spot of a single micro-lens. The divided wavefront is then focused on to a CCD detector. When the beam is perfectly collimated then the focus spot is on the axis at the center of mass of the micro-lens. Depending upon the location of the focused spot on the sensor, it is possible to determine the local inclination of the incident wavefront. Subsequent analysis of all focal spot positions determines the overall incident wavefront form. The resolution of the reconstructed wavefront depends upon the size and the focal length of the micro-lenses. We use the SHS ¹sensor with micro-lenses of diameter 150 μ m and focal length of 4.62 μ m. The CCD sensor on which the microlenses focus is of 1600×1200 pixels with pixel width of 7.5 μ m each.

1.5 Parallel work on the PhD timeline

This section summarizes concisely some of the works carried out along the PhD timeline but are beyond the scope of description in the thesis. These studies can be attributed to an attempt to learn the behavior of the illumination-scatterer interaction by pupil engineering, and increasing the information content in the scattered data. Also, the use of coherent light opens a frontier on phase retrieval and this was studied by through focus scanning. The details can be found in the relevant references.

1.5.1 Demonstration of an optimised focal field with long focal depth and high transmission obtained with the Extended Nijboer-Zernike theory

In several optical systems, a specific point spread function (PSF) needs to be generated. This can be achieved by shaping the complex field at the pupil. The extended Nijboer-Zernike (ENZ) theory relates complex Zernike modes on the pupil directly to functions in the focal region [26–28]. We used the ENZ theory to obtain a focused field with elongated focal length (up to 18 Rayleigh distances) with diffraction-limited spot size, while keeping the transmittance over 60%. The theory presented in this work is based on the functions that can be pre-calculated, the optimisation parameters are reduced to a limited number of Zernike coefficients that compose the pupil, allowing fast calculation of the focal field. We have found not only a way to create elongated focal spots, but also we have shown more generally that ENZ theory has the potential to be used for pupil engineering. The theoretical predictions are demonstrated experimentally through three pupil functions generated by a spatial light modulator (SLM) that produce elongated focal spots [29].

1.5.2 Through-focus phase retrieval and its connection to the spatial correlation for propagating fields

Through-focus phase retrieval methods aim to retrieve the phase of an optical field from its intensity distribution measured at different planes in the focal region. We have described through-focus phase retrieval methods and their connection to the concept of spatial correlation for propagated fields. By making use of the concept of degree of spatially correlation for complex fields and intensities, we could

¹Optocraft GmbH

predict which intensity distributions can be fruitfully used to start a phase retrieval procedure in a through focus configuration. Experimentally, the phase of an optical focused field, generated by a microscope objective with NA = 0.4, has been recovered with excellent accuracy. Our analysis also reveals why all techniques based on measuring the intensity at two Fourier-conjugated planes usually lead to a good reconstruction of the phase. The findings presented in this work are important for aberration characterization of optical systems, adaptive optics and wavefront metrology. We firmly believe that the concept we have introduced here to approach a phase retrieval problem can be safely extended to many more situations, not only to through-focus configurations [30].

1.5.3 Experimental and numerical analysis of the super resolution near-field effect on an InSb sample

The super resolution near-field effect has attracted the attention of many researchers since it offers a relatively simple way to overcome the diffraction limit of optical systems. This work contributes to improve the general understanding of the super-resolution near-field structure (Super-RENS) effect on Indium antimonide (InSb), establishing ideas that advanced microscopy, laser writing, and lithography could take advantage of.

There is an open question of what happens to the focused spot after passing through a thin activated super resolution layer. We have measured and analyzed the Super-RENS focused spot on an InSb sample at low numerical apertures. Coherent Fourier scatterometry and near-field scanning microscopy techniques are employed to monitor both, the phase transition of the sample and to measure the transmitted super-resolved spots. The experimental results confirm the predictions of the simulations based on the rigorous threshold model. Particular features predicted by the model, such as the dip in the center of the super-resolved spot and the wings at its edge were observed in the measurements. Furthermore, the spot size behavior as a function of the laser power showed a good match with the simulations. These results show, from a practical standpoint, that the threshold model is accurate enough to describe the characteristics of the Super-RENS focused spot. If different materials are to be used as the active medium, the model could be readily applied to investigate the super-resolved spots, provided that the refractive indices in the crystalline and molten states of that material are known. Moreover, the usage of Fourier scatterometry gives a fast way to determine the experimental conditions in which the effect takes place [31].

1.6 Outline of the thesis

In the thesis we introduce coherent Fourier scatterometry (CFS) as a sensitive tool for semiconductor metrology. In chapter 2 of the thesis, a framework to study the increment in sensitivity of CFS with respect to the IOS and the benefits of using a focused spot from a spatially coherent source (laser) are investigated on a theoretical viewpoint.

Owing to the coherent illumination, the far field in CFS comprise phase informa-

tion concealed in the complex reflection matrix of interaction. Intensity measurements provide the amplitude information but the phase information is absent. In chapter 3 of the thesis, we present a non interferometric partial phase retrieval (phase difference between the diffracted orders in the overlapping region) method from the intensity measurements in CFS.

In chapter 4, the experimental implementation of an operational CFS instrument in the laboratory environment is reported for grating reconstruction. In this chapter of the thesis the sensitivity of grating position with CFS is also demonstrated. Overlay, i.e., the positional accuracy of new patterns written on the existing ones in a multi-step lithographic process decides the performance of the circuitry. In chapter 5 of the thesis, the performance of CFS in comparison to IOS for overlay measurement is mathematically studied and compared in simulations.

Optical resolution is limited by the incident wavelength and numerical aperture in a far field optical system. In chapter 6 of the thesis, we implement a micro solid immersion lens (SIL) to improve the resolution in a scanning near field microscope setup. In this chapter it has been shown that micro-SIL can be used for metrology applications with high NA requirement. The idea, implementation and challenges associated with a Fourier scatterometer with a micro-SIL is presented in the chapter.

The fabrication process for the grating involves chemical and plasma treatment which can seldomly result in an unwanted surface over-layer on the nominal structure. In the chapter 7 of the thesis, the effect of the thickness of an oxide layer on the Si-etched grating is studied and is investigated on a real experimental sample using inverse grating reconstruction.

Performance analysis of coherent Fourier scatterometry

2.1 Abstract

Incoherent optical Scatterometry (IOS) is a well established and successful tool for high accuracy nano-metrology in research and industrial applications, to retrieve the properties of a given scatterer (here the grating) by looking at how the incoming light from a certain source, of certain wavelength and at certain angle is diffracted in the far field. In IOS, the light source is often a discharge lamp that, after wavelength filtering, is a quasi-monochromatic, but spatially incoherent source. In the thesis, we introduced a new technique called Coherent Fourier Scatterometry (CFS), in which incoherent illumination is replaced by a spatially coherent one. In this chapter, we present a framework to study the increment in sensitivity of CFS with respect to the IOS and the benefits of using a focused spot from a spatially coherent source (laser) are investigated on a theoretical viewpoint. The grating is defined in terms of a finite number of geometrical shape parameters (such as height, side-wall angles, midCD). The focused spot is scanned over the grating, and for each scan position, a far-field diffraction pattern is recorded. Through sensitivity analysis using rigorous electromagnetic simulations, we show that the use of coherence and multiple scanning makes CFS more sensitive than IOS. Polarization dependent sensitivity of the grating parameters are presented and discussed. Also, the dependence of scanning positions on the sensitivity analysis is highlighted and the stability of the sensitivity with optimum number of scanning position is shown.¹

¹This chapter is based on the studies and results published in [32–34].

2.2. Introduction 11

2.2 Introduction

At present, Incoherent optical scatterometry (IOS), is the commonly used metrology technique for inverse grating reconstruction in semiconductor industry. We introduce coherent Fourier scatterometry (CFS) as a new metrology technique in this thesis, and in this chapter, the performance of CFS is compared to IOS in terms of their sensitivities for a small change in the grating shape parameters. The performance analysis is based on the comparison between the estimated uncertainties in the measurement of shape parameters, when the focused spot from a spatially coherent or a completely incoherent light is used as the source of illumination. The focused spot in CFS is scanned over the grating to register the far field at each scan position. Scanning the focused spot on the grating is used to get the phase information.

The chapter is organized as follows: In Section 2.3, the model for the diffraction grating, the grating parameters and the illumination scheme are discussed. The statistical model to estimate the uncertainties on the grating parameters is presented in Section 2.4. Effect of scanning on the complex amplitude of diffracted orders are discussed in Section 2.5. Section 2.6 presents the theoretical estimation of uncertainties in the grating parameters. Section 2.7 summarizes the results of the sensitivity analysis.

2.3 Model of the grating

Let us assume a periodic, one-dimensional, infinite and symmetric grating with period (Λ) as illustrated in Fig. 2.1. One-dimensional grating here refers to grating properties invariant along one direction (i.e., along the y-axis in Fig. 2.1), while periodic along the x-axis.

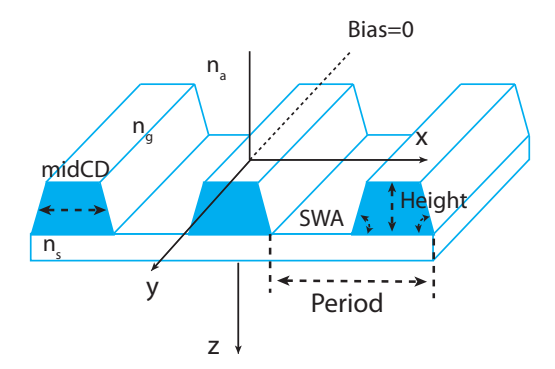


Figure 2.1: Geometrical representation of the periodic grating and the coordinate system with corresponding shape parameters: height, midCD, and SWA. Bias is also shown. Here n_g , n_a and n_s represent the refractive indices of the grating, air and the substrate.

In Fig. 2.1, n_g , n_a and n_s are the refractive indices corresponding to the grating material, surround medium (air) and the substrate. The refractive index can be complex valued but is real for a pure dielectric medium. For a defined pitch, the shape of the grating is described with a given number of parameters which is to be determined experimentally. Here, a trapezoidal grating is described by three parameters, namely: height, side wall angle (SWA) and midCD. MidCD is the critical dimension at half height of the grating. Additionally we also introduce bias as an additional parameter defined for absolute scan positions of the grating with respect to the x-axis as shown in fig. 2.1.

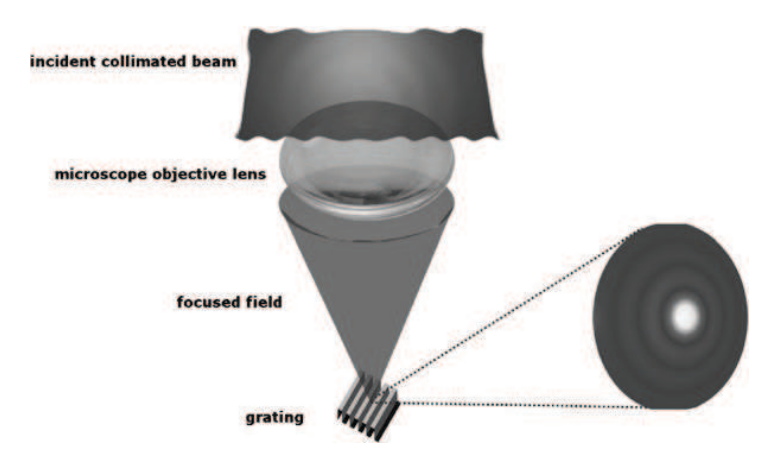


Figure 2.2: A simple graphical illustration of the illumination principle. A collimated beam from a coherent source is incident on the microscope objective and the focused spot interacts with the grating. Magnified focused spot structure is also shown. The figure dimensions are not in scale.

The illumination is characterized by the focused spot from a coherent source. Figure 2.2 shows a simple sketch of the illumination. An expanded collimated light is focused on the grating by a microscope objective (MO) of numerical aperture (NA). The field distribution is uniform in the back focal plane (BFP) of the MO and each point in this distribution converts the incoming beam into a plane wave impinging on the grating with an angle defined by the location of the point in the BFP. The maximum angle of incidence is given by the NA of the MO. Also, the focused beam interaction allows multiple incidence angle at once on the grating. After interaction of the focused beam and the grating, part of the scattered light is collected by the same MO and the far field is registered at a CCD camera. The dependence of the far field intensity distribution to the grating parameters are then analyzed.

2.4 Sensitivity analysis: Model and theory

Let the incident polarization at the entrance pupil be either along x-axis (TM) or along y-axis (TE) (see Fig. 2.1 for axis definition). The scattered light after interaction is measured (without polarizer) at the detector for either of the two orthogonal incident polarizations. Let I_x and I_y be the far field intensity for x (TM) and y (TE) polarized incident light in the entrance pupil of the microscope objective, respectively. Let I_i^m be the combined measurement (index m denotes the measurement data) containing I_x and I_y . Here i = 1, ...N. with $N = 2N_d$, N_d is the number of pixels on the detector. Let the shape parameters be denoted by \mathbf{a} and the fixed experimental parameters by \mathbf{p}_i (for example: incident wavelength, polarization etc). Due to the presence of noise, the corresponding intensity I_i^m have uncertainties given by σ_i , i = 1, ...N. For simplicity, only the random errors are considered and the systematic errors in the measurements are omitted. Following the approach suggested in [35], the noise of the measured data is independent and normally distributed with standard deviation given by measured uncertainties σ_i . Also, for simplicity $\sigma_i = \sigma, \forall i$.

To compute the sensitivity of coherent Fourier scatterometry (CFS) compared to the currently used incoherent optical scatterometry (IOS), the uncertainty in the grating shape parameters Δa is computed with a maximum likelihood estimate [36]. Given the set of observations, it is desired to summarize and apply the experimental data by fitting to a known model depending on the shape and fixed parameters (\mathbf{p}_i , \mathbf{a}). Rigorous coupled wave analysis (RCWA) is used for forward simulations of the diffracted far field intensity denoted by $I_i^s(\mathbf{p}_i, \mathbf{a})$ from the grating to match the experiments. When the set of shape parameters coincides with the real ones, within some accuracy, then the distance between the measurement and the simulation is minimum. In statistical theory, the difference between the measured and the simulated intensities can be defined by chi-square (χ^2) distribution [36] given as,

$$\chi^2 = \frac{1}{N} \sum_{i=1}^{N} \left[\frac{I_i^m - I_i^s(\mathbf{p}_i, \mathbf{a})}{\sigma_i} \right]^2. \tag{2.1}$$

In the ideal noiseless system, there would be perfect match between the experimental and simulated far field for the right set of grating parameters without any uncertainty. However, due to presence of noise in the real data, there is an uncertainty Δa in the parameters. In maximum likelihood approach, the uncertainty Δa can be derived by expanding Eqn. 2.1 in the Taylor series around the minimum. The gradient of χ^2 with respect to the parameters **a** is given by,

$$\frac{\partial \chi^2}{\partial a_j} = \frac{-2}{N} \sum_{i=1}^N \frac{1}{\sigma_i^2} \left\{ \left[I_i^m - I_i^s(\mathbf{p}_i, \mathbf{a}) \right] \frac{\partial I_i^s(\mathbf{p}_i, \mathbf{a})}{\partial a_j} \right\}. \tag{2.2}$$

In Eqn. 2.2, subscripts j, k refer to the grating shape parameter. Taking an additional partial derivative, the hessian is given by,

$$\frac{\partial^2 \chi^2}{\partial a_j \partial a_k} = \frac{2}{N} \sum_{i=1}^N \frac{1}{\sigma_i^2} \left\{ \frac{\partial I_i^s(\mathbf{p}_i, \mathbf{a})}{\partial a_j} \frac{\partial I_i^s(\mathbf{p}_i, \mathbf{a})}{\partial a_k} - \left[I_i^m - I_i^s(\mathbf{p}_i, \mathbf{a}) \right] \frac{\partial^2 I_i^s(\mathbf{p}_i, \mathbf{a})}{\partial a_j \partial a_k} \right\}.$$
(2.3)

In Eqns. 2.2 and 2.3, N is the total number of pixels while indices j and k refers to the grating shape parameters. In Eqn. 2.3, the term containing second order derivative is neglected, as for minimum χ^2 the term $[I_i^m - I_i^s(\mathbf{p}_i, \mathbf{a}_i)]$ is the random measurement error at each point, which when averaged over i should cancel. Hence Eqn. 2.3 can be written as,

$$\frac{1}{2} \frac{\partial^2 \chi^2}{\partial a_j \partial a_k} \approx \frac{1}{N} \sum_{i=1}^N \frac{1}{\sigma_i^2} \left[\frac{\partial I_i^s(\mathbf{p}_i, \mathbf{a})}{\partial a_j} \frac{\partial I_i^s(\mathbf{p}_i, \mathbf{a})}{\partial a_k} \right]. \tag{2.4}$$

The curvature matrix $[\alpha_{ik}]$ is defined as,

$$[\alpha_{jk}] = \frac{1}{N} \sum_{i=1}^{N} \frac{1}{\sigma_i^2} \left[\frac{\partial I_i^s(\mathbf{p}_i, \mathbf{a})}{\partial a_j} \frac{\partial I_i^s(\mathbf{p}_i, \mathbf{a})}{\partial a_k} \right]_{\chi^2 = \chi^2_{min}}, \tag{2.5}$$

where $j, k = 1, 2, 3, \dots$ The covariance matrix [36] $[C_{jk}]$ is given by,

$$[C_{jk}] = [\alpha_{jk}]^{-1}$$
. (2.6)

The estimated 3- σ uncertainties Δa_j in the grating shape parameter \mathbf{a}_j is then given as

$$\Delta a_j = 3\sqrt{C_{jj}} \tag{2.7}$$

An analysis of the estimated uncertainties of the grating shape parameters is fundamental to the performance analysis of coherent Fourier scatterometry. A low uncertainty value means the higher accuracy to retrieve the grating parameters, while a large Δa infers to a less sensitive technique. Large uncertainty implies that that there are several sets of $\bf a$, which are equally probable fits for the measurement and the technique cannot differentiate between them. Hence low uncertainty is desired for a highly sensitive method. It follows that the estimated uncertainty of grating shape parameters for various techniques, is the measure of the technique's sensitivity.

2.5 Effect of scanning in CFS

In IOS, a spatially incoherent light, when focused on the grating, generates a large focus spot (as compared to coherent illumination case), which illuminates a number of periods of the grating at once. However, for a spatially coherent source of identical wavelength and NA of the focusing lens, a diffraction limited focus spot

is generated of the order of the wavelength. The size of the focused spot depends on the incident wavelength and the NA. When a strongly focused spot is incident on the grating, a scanning scheme needs to be implemented in order to cover the grating period. In our case, there is always an overlap between the two adjacent scanning positions. This is in accordance with the recent scanning scheme used in phase retrieval from far field intensity data [37, 38]. The scanning scheme for data acquisition is shown in Fig. 2.3. Scanning plays an important role in sensitivity increase in CFS, which will be presented in the next section. Also, owing to the scanning, CFS is sensitive to the shift of the grating through a phase factor proportional to the shift. This can be used to retrieve the grating position (bias) along with the shape parameters.

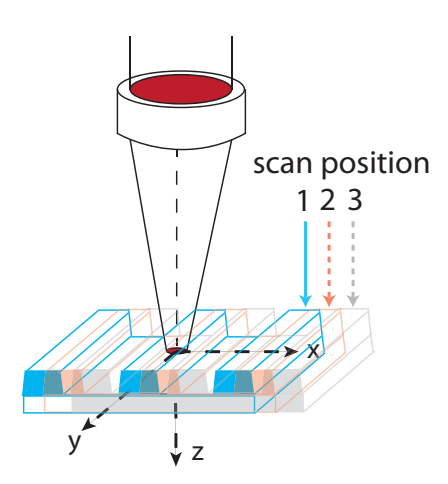


Figure 2.3: Scanning scheme in CFS. The grating is scanned over the focus spot and the far field intensity maps corresponding to several scanning positions within a period of the grating are registered at the detector in the far field. Three scan positions of the grating are illustrated by different colors in the figure.

From an experimental viewpoint, scanning is time consuming and slows down the measurement process, since a number of acquisition steps are required, but it also increases the sensitivity. From the computational viewpoint, the far fields at all the scan positions need to be computed, which is computationally extensive. This problem can be solved by using the effect of scanning on the diffracted orders. There is a constant phase shift in the diffracted field of all the non zero diffracted orders depending upon the relative distance between two scan positions. This property can be used in computation of far fields by RCWA for different scan positions. The consecutive position can be computed (without rigorous computation, by adding an additional phase term for the scanning distance) if the far field at the pre-adjacent position is computed rigorously and the distance between the consecutive positions are known. The relation between complex amplitudes at

successive positions for a one-dimensional grating with period Λ is given by [32],

$$R'_{m} = R_{m} \exp\left[i2\pi \frac{m\Delta x}{\Lambda}\right], \qquad (2.8)$$

where, R'_m is the complex amplitude for the m^{th} order after shifting Δx from its initial position R_m . When m=0 (zeroth order), the complex amplitude for the diffracted order is identical for all scan positions.

A typical CFS measurement acquires several far field intensity maps within a single period of the grating. From Eqns. 2.5, 2.6 and 2.7, the uncertainty scales with the total number of data points by $\frac{1}{\sqrt{N}}$ i.e., more points means smaller uncertainties. In order to make a fair comparison, the number of scan positions is taken into account as scanning in CFS adds more data. In estimated uncertainty analysis in the grating shape parameters, the far field for a single position in IOS is compared to the far fields for several positions in CFS (M) within a period of the grating and thus the uncertainty in CFS needs to be multiplied by \sqrt{M} for comparison to IOS. By the definition of χ^2 in Eqn. 2.1, the indifference in uncertainty with the number of data points is absent.

2.6 Estimated uncertainties: Simulations

Once the model of the grating, the rigorous Maxwell solver, and the statistical method to analyze the estimated uncertainties in grating shape parameters are available, the effect of coherence in scatterometry can be evaluated. In the remaining part of this chapter, we consider an etched silicon grating (Si), being the substrate. The surrounding medium to the grating is air $(n_a = 1)$. In simulations, we use an incident wavelength of $\lambda = 633$ nm and two distinct NA's of 0.4 and 0.95, respectively, to study the response of CFS at relatively low and high NA's. The complex refractive index for Si at 633 nm is 3.882 - 0.019i. The negative sign of the imaginary part the refractive index is in convention with RCWA algorithm implementation.

To compute the covariance matrix as in Eqn. 2.6, the derivatives are computed numerically. The derivatives in Eqn. 2.5 are computed by central finite difference method where the size of the grid is fixed to 0.1 nm for midCD, height and bias, while the angular grid is fixed at 0.1° degrees for SWA. The typical grating chosen for the sensitivity analysis is defined by the parameters vector [midCD, height, SWA] = [0.5, 0.25, 90] (in fraction of the pitch, in fraction of incident wavelength and degrees). The period of the grating is chosen for the value of $0.6 < \frac{\lambda}{NA\Lambda} < 2.2$, which gives the range of the periods (for simulations) [≈ 303 nm to ≈ 1110 nm], when the illumination wavelength is 633 nm and the numerical aperture is 0.95 and for NA=0.4, the range of periods are [≈ 720 nm to ≈ 2637 nm]. The number of diffracted orders inside the lens pupil is given by Eqn. 2.9, with u being a positive integer, the first u orders are collected by the lens:

$$\frac{\lambda}{NA\Lambda} < \frac{2}{u}.\tag{2.9}$$

For the given illumination wavelength (633 nm) and NA (0.95), the distribution of orders in the exit pupil of the microscope objective for different values of periods of the grating are as follows: There exists only the 0^{th} order for the period of the grating up to 296 nm ($\frac{\lambda}{NA\Lambda} > 2$), for the periods ranging from 296 nm to 333 nm, there exist the 0^{th} and the $\pm 1^{st}$ orders ($1 < \frac{\lambda}{NA\Lambda} < 2$), from 333 nm up to 666 nm there exist the 0^{th} , $\pm 1^{st}$ and $\pm 2^{nd}$ diffracted orders ($0.67 < \frac{\lambda}{NA\Lambda} < 1$) and then for periods up to 1110 nm there exit the 0^{th} , $\pm 1^{st}$, $\pm 2^{nd}$ and $\pm 3^{rd}$ ($0.6 < \frac{\lambda}{NA\Lambda} < 0.67$) in the exit pupil of the lens (Fig. 2.4).

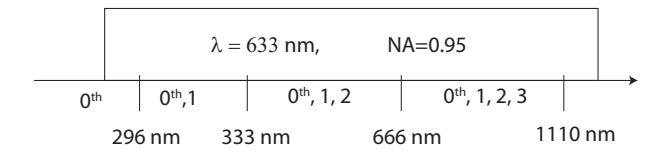


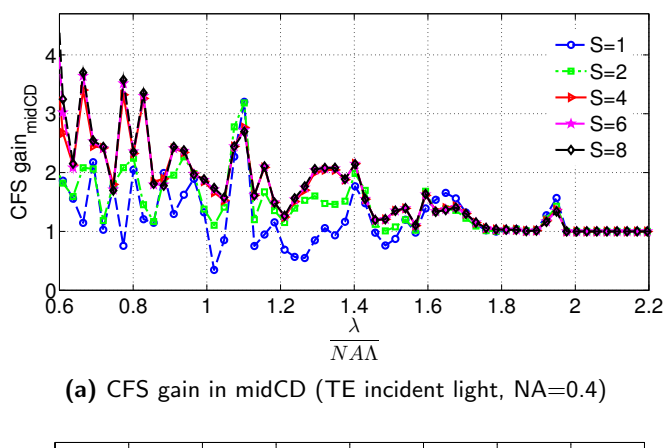
Figure 2.4: Diffracted orders captured by the lens for the range of periods of the gratings shown in the bottom row of the graph when illuminated at 633 nm with a microscope objective of NA=0.95.

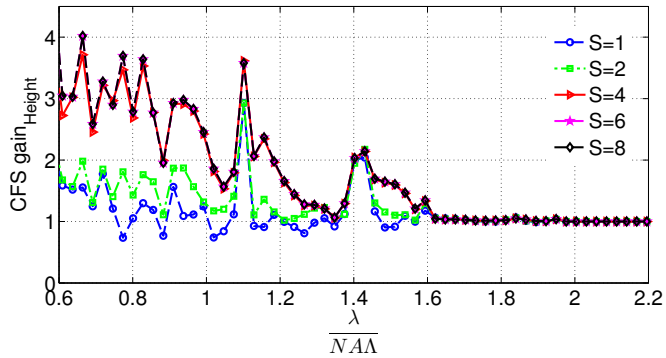
The uncertainties in the grating shape parameters are computed using Eqn. 2.7 and compared for the case of incident incoherent and coherent illumination. The uncertainty of grating parameters in IOS and CFS is expressed as the ratio $\frac{\Delta a_{inc}}{\Delta a_{coh}}$, which can be alternatively written as $\frac{3\sigma_{inc}}{3\sigma_{coh}}$ and is called CFS gain in the chapter. A systematic study for CFS gain is carried out for the grating parameters. In Section 2.6.1, the CFS gain is studied for the effect of coherence, number of scanning positions and its dependence on the incident polarizations. In Section 2.6.3, the bias dependence is studied.

2.6.1 Effect of coherent illumination: polarization dependence

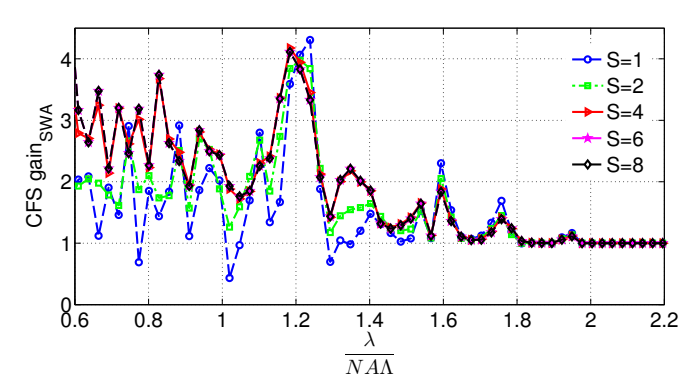
The sensitivity of the grating parameters in CFS compared to the conventional IOS is shown in this section. CFS gain is presented for the low (0.4) and high (0.95) NA respectively, when $0.6 \le \frac{\lambda}{NA\Lambda} \le 2.2$. The results have been summarized in terms of NA's (0.4 and 0.95), number of scan positions and the response of the grating parameters for two orthogonal incident polarizations in the entrance pupil of the focusing lens, namely along the x-axis (TM: incident electric field is along the direction of periodicity of the grating) and the y-axis (TE: incident electric field is along the grooves of the grating). In CFS a scanning focused spot scheme is employed as shown in Fig. 2.3, and the total number of independent scan positions considered within a period of the grating in the simulations are 1, 2, 4, 6 and 8. Figure 2.5 and 2.6 shows the CFS gain at low numerical aperture (NA=0.4) for the set of two orthogonal incident polarizations in the entrance pupil of the MO. Similarly, the graphs in Figs. 2.7 and 2.8 present the CFS gain for higher NA (0.95)

for grating parameters midCD, height and SWA. The different color coded graphs represents the number of scanning positions for CFS within a single period of the grating. The horizontal axes of the graphs represent the period of the grating expressed in the dimensionless quantity $\frac{\lambda}{NA\Lambda}$ and vertical axis is the CFS gain, the ratio of uncertainty in grating parameters for IOS and CFS. Here, CFS gain ≥ 1 infers that the sensitivity of grating parameter in CFS is higher compared to IOS. CFS gain is polarization dependent and to visualize the effect of polarization explicitly, Fig. 2.9 in section 2.6.2 presents the polarization dependent sensitivity of the individual grating parameters for single and 8 scanning positions.



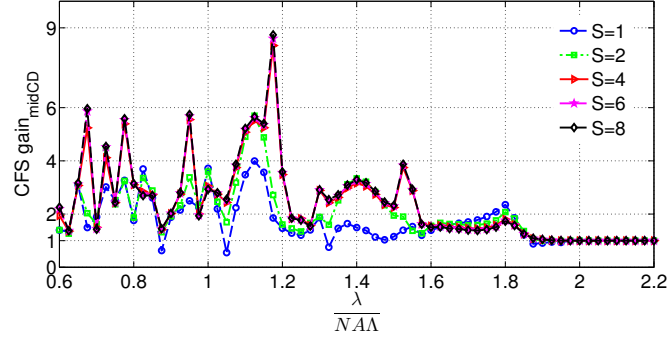




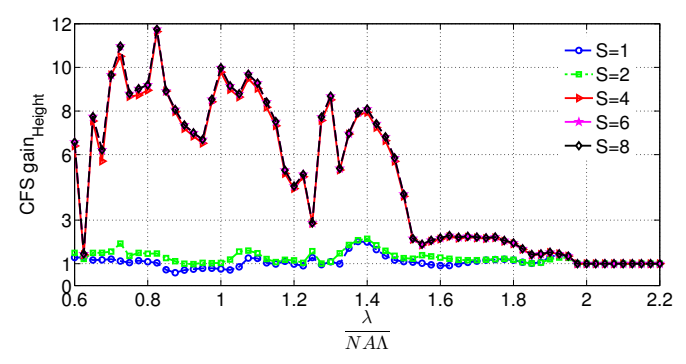


(c) CFS gain in SWA (TE incident light, NA=0.4)

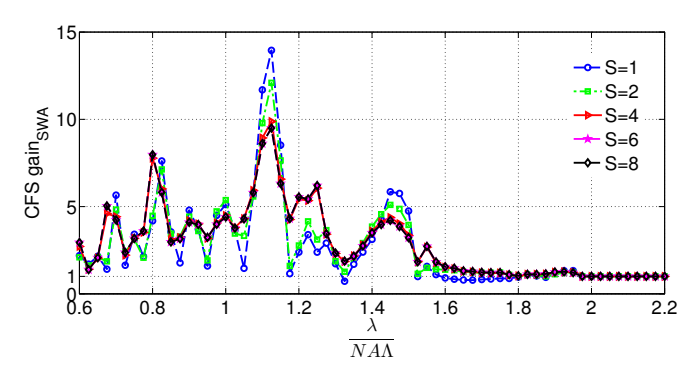
Figure 2.5: Ratio between uncertainty (CFS gain) in grating shape parameters in IOS compared to CFS for TE incident field and mixed output and low numerical aperture (NA=0.4). (a) Sensitivity analysis for midCD, (b) Sensitivity analysis for height (c) Sensitivity analysis for SWA. The graphs are obtained for $0.6 \le \frac{\lambda}{NA\Lambda} \le 2.2$. Color coded graphs in the figure represents the number of evenly distributed independent scanning positions within a single period of the grating in CFS. The number of independent scanning positions within a period of the grating are S = 1, 2, 4, 6 and 8.



(a) CFS gain in midCD (TM incident light, NA=0.4)

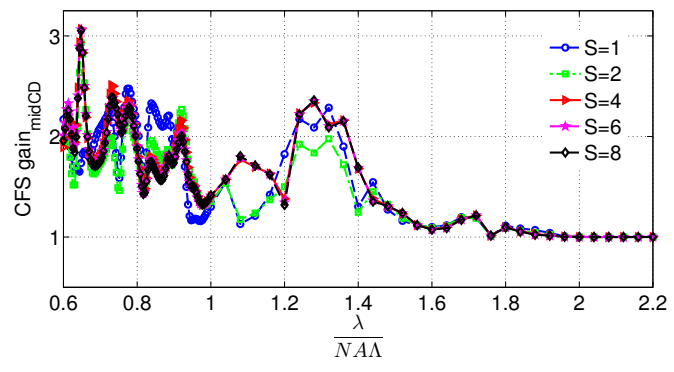


(b) CFS gain in height (TM incident light, NA=0.4)

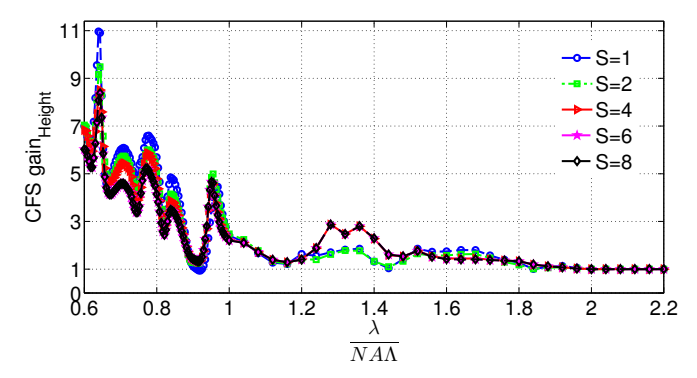


(c) CFS gain in SWA (TM incident light, NA=0.4)

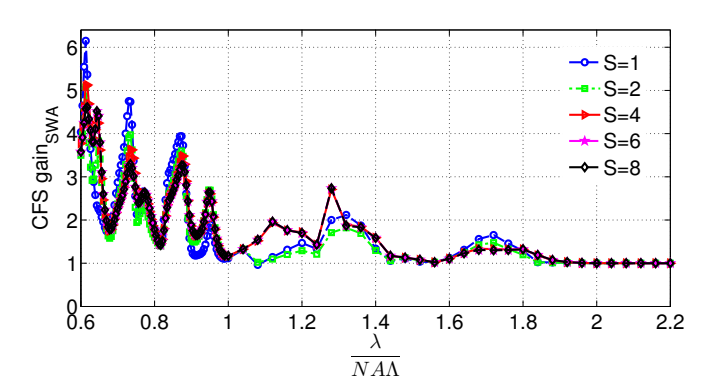
Figure 2.6: Ratio between uncertainty (CFS gain) in grating shape parameters in IOS compared to CFS for TM incident field and mixed output and low numerical aperture (NA=0.4). (a) Sensitivity analysis for midCD, (b) Sensitivity analysis for height (c) Sensitivity analysis for SWA. The graphs are obtained for $0.6 \leq \frac{\lambda}{NA\Lambda} \leq 2.2$. Color coded graphs in the figure represents the number of evenly distributed independent scanning positions within a single period of the grating in CFS. The number of independent scanning positions within a period of the grating are S = 1, 2, 4, 6 and 8.



(a) CFS gain in midCD (TE incident light, NA=0.95)

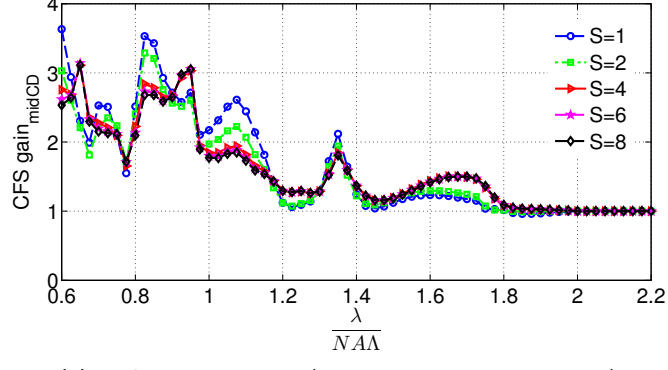


(b) CFS gain in height (TE incident light, NA=0.95)

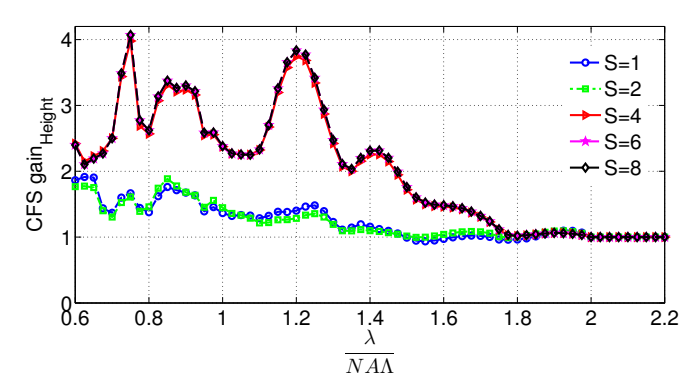


(c) CFS gain in SWA (TE incident light, NA=0.95)

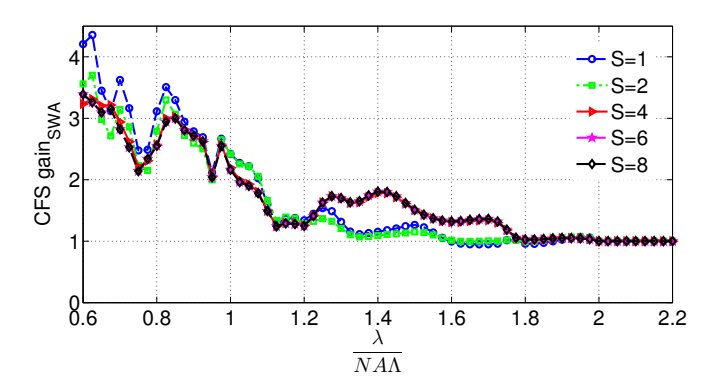
Figure 2.7: Ratio between uncertainty (CFS gain) in grating shape parameters in IOS compared to CFS for TE incident field and mixed output and high numerical aperture (NA=0.95). (a) Sensitivity analysis for midCD, (b) Sensitivity analysis for height (c) Sensitivity analysis for SWA. The graphs are obtained for $0.6 \le \frac{\lambda}{NA\Lambda} \le 2.2$. Color coded graphs in the figure represents the number of evenly distributed independent scanning positions within a single period of the grating in CFS. The number of independent scanning positions within a period of the grating are S = 1, 2, 4, 6 and 8.



(a) CFS gain in midCD (TM incident light, NA=0.95)



(b) CFS gain in height (TM incident light, NA=0.95)



(c) CFS gain in SWA (TM incident light, NA=0.95)

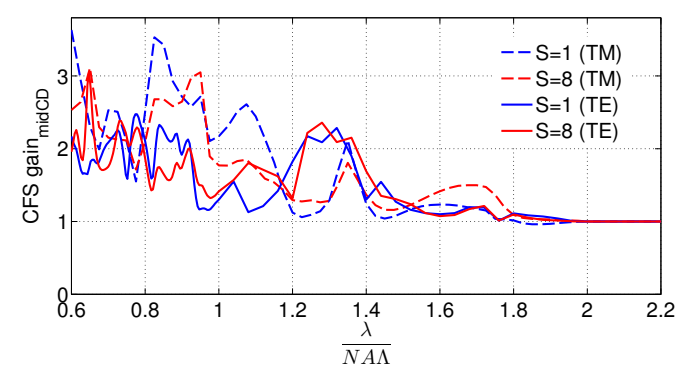
Figure 2.8: Ratio between uncertainty (CFS gain) in grating shape parameters in IOS compared to CFS for TM incident field and mixed output and high numerical aperture (NA=0.95). (a) Sensitivity analysis for midCD, (b) Sensitivity analysis for height (c) Sensitivity analysis for SWA. The graphs are obtained for $0.6 \le \frac{\lambda}{NA\Lambda} \le 2.2$. Color coded graphs in the figure represents the number of evenly distributed independent scanning positions within a single period of the grating in CFS. The number of independent scanning positions within a period of the grating are S = 1, 2, 4, 6 and 8.

A few key observations from the sensitivity analysis in the graphs can be summarized as follows:

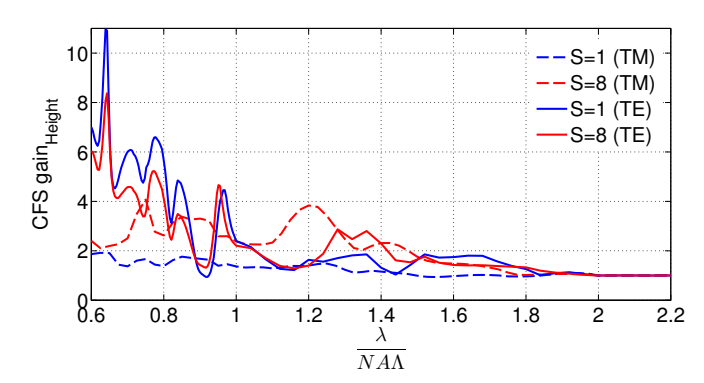
- 1. CFS gain is unity for $\frac{\lambda}{NA\Lambda} > 2$. In this region, there exists only specular (0^{th}) diffracted order in the far field, hence the effect of coherence and interference between the diffracted orders are absent. It is also to be noted that, the scanning plays no role in CFS. Hence, the performance of CFS and IOS are identical. It sets the limit on the minimum period of the grating investigated by CFS for CFS gain> 1.
- 2. For all values of $\frac{\lambda}{NA\Lambda} \leq 2$, the CFS gain varies with the period of the grating. The variation in the CFS gain is non linear. There exists higher diffracting orders in the exit pupil and the interference between the diffracted orders contribute to the the performance for CFS. In the region of $1 \leq \frac{\lambda}{NA\Lambda} \leq 2$, there are 0^{th} , and ± 1 in the exit pupil with an overlap between 0^{th} and ± 1 and for $0.67 \leq \frac{\lambda}{NA\Lambda} \leq 1$ the interference there is three beam interference in the exit pupil and so on.
- 3. In the regions $\frac{\lambda}{NA\Lambda}$ < 2, the CFS gain in Figs. 2.5, 2.6, 2.7 and 2.8 for a single scan position is < 1 for a few values of the grating periods. It illustrates that the CFS is less sensitive to the grating parameters, even in the presence of the higher diffracted orders interfering with each other. The possible explanation for this behavior in CFS gain is the destructive interference between the diffracted orders, which leads to the low signal to noise ratio in CFS far fields (at many pixels in the far field) compared to the far fields in IOS.
- 4. However, CFS gain also depends on the number of scanning positions in CFS. For more than one scanning position, the CFS gain is always greater than unity. This can also be explained by the above logic: by scanning, the contribution of these particular pixels with low signal-to-noise ratio is smeared out and the effective interference signal plays the prominent role in the CFS gain evaluation. This highlights the need of scanning spot implementation in CFS. Due to interference and scanning, sometimes more than four fold increase in CFS gain is obtained. The simulations are performed for a number of scanning positions within a single period of the grating. It can be seen that for scan positions ≥ 5, the variation in CFS gain is marginal. This can be understood from the fact that when two orders are present in the far field then the system works as a two beam interferometer and in the presence of higher orders, it acts as a multiple beam interferometer and hence requires only a few scanning positions to resolve the phase information in the CFS scanning scheme.
- 5. CFS gain depends on the incident polarization in the entrance pupil of the microscope objective. In Section 2.6.2, polarization dependent sensitivity in the grating parameters is shown explicitly.
- 6. CFS gain depends on the numerical aperture of the microscope objective.

2.6.2 Polarization dependent sensitivity

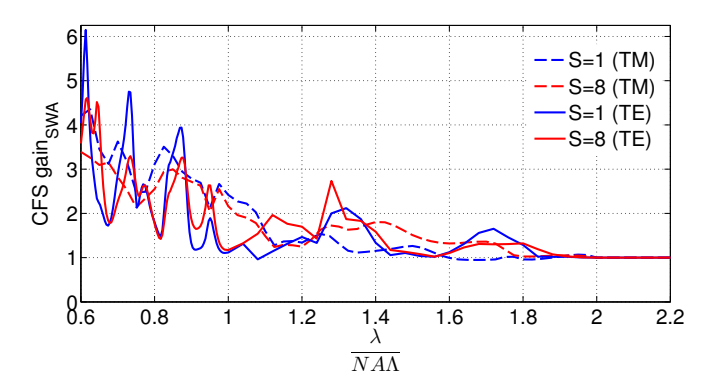
As shown in Figs. 2.5 and 2.6, CFS gain depends on the incident polarization. Figure 2.9 compares the polarization dependent CFS gain grating parameters midCD, height and SWA respectively for 1 and 8 independent scan positions within one period of the grating. We choose scanning positions 1 and 8 as this is the extremum of the CFS gain as illustrated in Figs. 2.5 and 2.6. The numerical aperture of the microscope objective is 0.95. CFS gain is plotted when the incident polarization is TE and TM respectively in the entrance pupil of the grating. The CFS gain for either TE or TM incident polarization follows a similar behavior for all the grating parameters, but the magnitude of CFS gain is polarization dependent. It can be seen that CFS gain magnitude is considerably higher for TM incident polarization, indicating the higher sensitivity of grating parameters for TM incident polarization.



(a) Polarization dependent sensitivity for midCD for total number of scan positions = 1 and 8



(b) Polarization dependent sensitivity for height for total number of scan positions $=1\mbox{ and }8$



(c) Polarization dependent sensitivity for SWA for total number of scan positions $=\,1$ and 8

Figure 2.9: Polarization dependent CFS gain, when the number of scanning positions in CFS are 1 and 8 respectively for NA=0.95. (a) Polarization dependent sensitivity for midCD (b) Polarization dependent sensitivity for height (c) Polarization dependent sensitivity for SWA. The graphs are obtained for $0.6 \leq \frac{\lambda}{NA\Lambda} \leq 2.2$.

2.6.3 Bias dependent CFS gain

In focused spot scanning CFS, the relative position of the grating with respect to the illumination axis is defined as bias in Fig. 2.1. Also, it has been shown in Figs. 2.7 and 2.8, that the CFS gain ≥ 1 with more than one scanning position and reaches its limit for higher number of scanning positions. The total number of scanning positions required is a function of the number of overlapping orders in the exit pupil.

Figure 2.11 plots the CFS gain with several initial bias values for the grating parameters of midCD, height and SWA. The color coded graphs represent the bias given by 0, $\Lambda/8$, $\Lambda/4$, $\Lambda/3$ and $\Lambda/2$ for the symmetric grating defined in Fig. 2.10, with a single scan position on the grating, while Fig. 2.12 represents the CFS gain when the initial bias values are different as in Fig. 2.11 but with a total of 8 scanning positions.

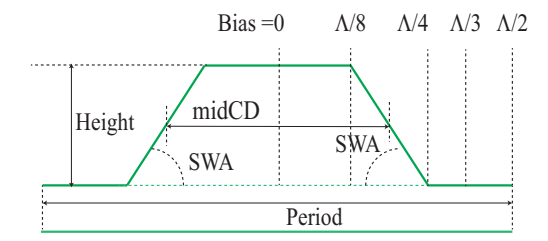
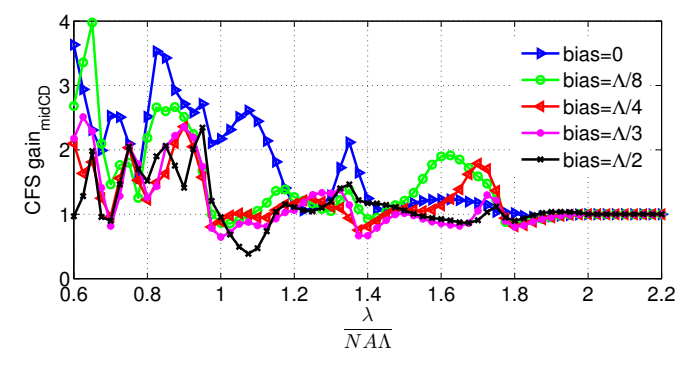
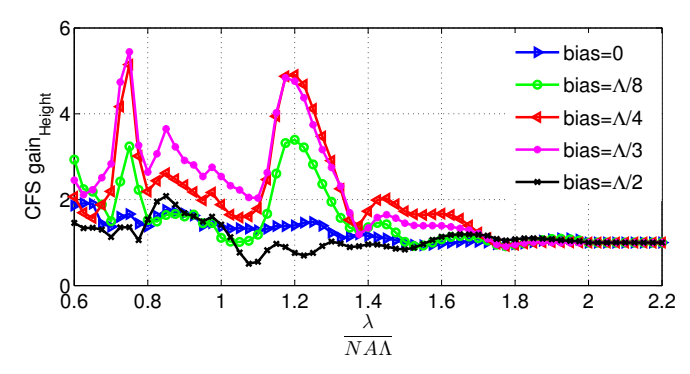


Figure 2.10: Cross-section of a single period of the grating where the scan positions in CFS are shown. The the grating is scanned over the focus spot for five scan positions given as bias =[0, $\Lambda/8$, $\Lambda/4$, $\Lambda/3$, $\Lambda/2$].

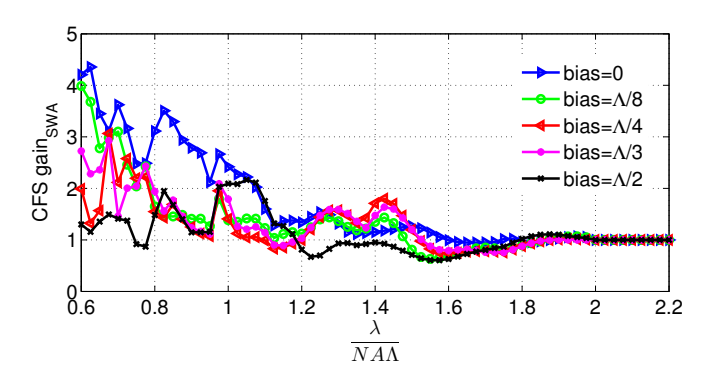
For a single scan position CFS gain is highly dependent upon the initial bias value. This can be explained from the fact that the grating interacts with the focused spot and the structure of the focused spot (Airy beam) is not of uniform amplitude on the grating. In contrast, when the scanning positions are increased, the CFS gain is independent of the initial bias, and it stabilizes to the best CFS gain possible. This indicates that exact positioning of the grating in experiment is not important when scanning is done and the pitch of the grating can be chosen irrespective of the effect of specific positioning of the grating. With sufficient scanning positions within one period of the grating, there is little correlation between the position and the grating shape parameters of the grating.



(a) Bias dependent sensitivity of midCD for a single scan position

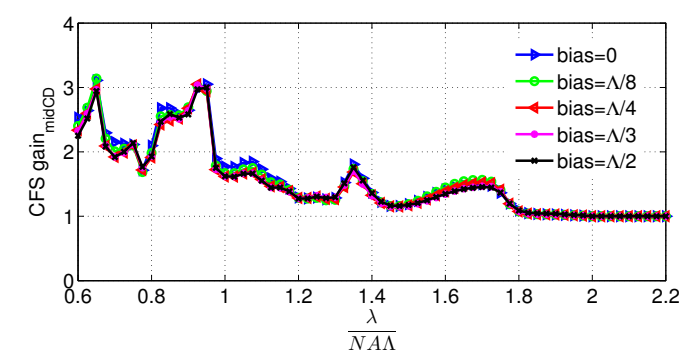


(b) Bias dependent sensitivity of height for a single scan position

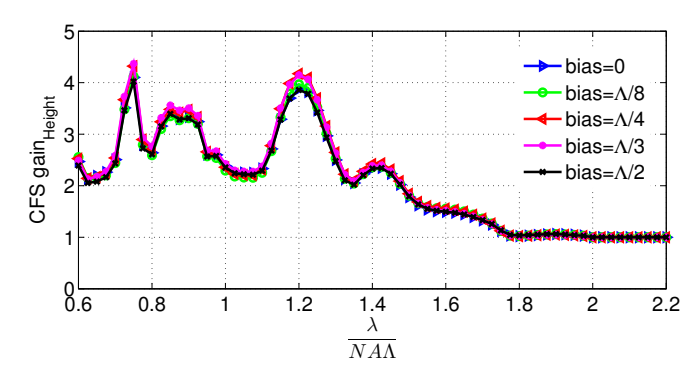


(c) Bias dependent sensitivity of SWA for a single scan position

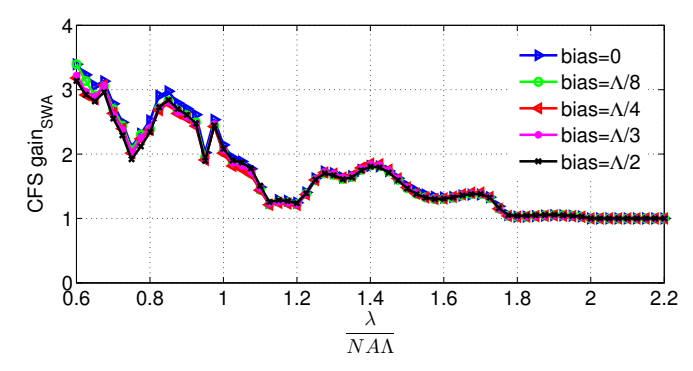
Figure 2.11: Position dependent sensitivity of grating parameters for a single scan position for TM incident polarization (a) Sensitivity analysis for midCD, (b) Sensitivity analysis for Height (c) Sensitivity analysis for SWA. The graphs are obtained for pitch varying from 0.4 μ m to 3 μ m. Color coded graphs in each figure represents the position of the grating which is given by bias 0, $\Lambda/8$, $\Lambda/4$, $\Lambda/3$, and $\Lambda/2$.



(a) Bias dependent sensitivity of midCD for 8 independent scan positions within $\Lambda.$



(b) Bias dependent sensitivity of height for 8 independent scan positions within $\Lambda.$



(c) Bias dependent sensitivity of SWA for 8 independent scan positions within $\Lambda.\,$

Figure 2.12: Position dependent sensitivity of grating parameters for for 8 independent scan positions within Λ for TM incident polarization. (a) Sensitivity analysis for midCD, (b) Sensitivity analysis for Height (c) Sensitivity analysis for SWA. The graphs are obtained for pitch varying from 0.4 μm to 3 μm . Color coded graphs in each figure represents the position of the grating which is given by bias 0, $\Lambda/8$, $\Lambda/4$, $\Lambda/3$ and $\Lambda/2$.

2.7. Conclusions 29

2.7 Conclusions

To summarize, a theoretical study on uncertainty analysis for IOS compared CFS has been performed. After considering a specific model for the grating and the illumination, the estimated uncertainties of IOS and CFS were compared under the assumption of the Gaussian distribution of the measurement noise with $\sigma = 2.7 \times 10^{-4}$). Based on the simulations, we can conclude that CFS is more sensitive to change in grating parameters compared to IOS under special circumstances, i.e., when there is an overlap between the diffracted orders in the exit pupil. Although, initial bias value influence the CFS sensitivity for a single scan position, this can be minimized with several scan positions within one period of the grating. Scanning is the most important aspect of CFS. There is an optimum number of scanning positions, which depends on the number of diffracted orders in the exit pupil. The CFS performance increases with scanning scheme. Also, the incident polarization plays an important role in the sensitivity analysis and the different grating parameters respond to it in a non linear, non-monotonic way.

Phase retrieval between overlapping orders in coherent Fourier scatterometry

3.1 Abstract

The far field in coherent Fourier Scatterometry (CFS) contains phase information owing to the coherent interaction of light with the scatterer. Finding the complex reflection matrix in CFS requires the knowledge of the amplitude and phase of the individual components of the matrix. Intensity measurements provide the amplitude information but the phase information is absent. We present here a non interferometric partial phase retrieval method from the intensity measurements in CFS. Formulae to determine the state of polarization of the scattered light and to retrieve the phase difference between overlapping scattered orders are given. The phase information of the elements of the reflection matrix is used to study the effect of polarization dependent phase sensitivity of grating parameters. The scattered far-field is rigorously computed and the effectiveness of the method is proved with experimental results.¹

 $^{^1{\}rm This}$ chapter is based on the studies and results published in [39]

3.2. Introduction 33

3.2 Introduction

In conventional incoherent optical scatterometry (IOS), light from an incoherent source interacts with the scatterer and the diffracted far field intensity distribution is recorded [10,11] at the detector. The intensity distribution in the diffracted far field depends on the material composition and the geometrical properties of the scatterer that one wants to reconstruct [12,40,41]. The scatterer in our application is a diffraction grating. In addition to intensity information in IOS, far fields in coherent Fourier scatterometry (CFS) also encodes the phase information because of the coherent nature of the interaction. Adding phase information to the far field measurements in CFS helps to improve accuracy as well as to reduce ambiguity in grating reconstruction. Generally, field oscillations in applications at optical frequency are far beyond the detector acquisition time and hence only amplitude of the field can be measured directly. The phase information is lost giving rise to the phase problem [5]. It is evident from Maxwell's equations that amplitude and phase are not independent and hence intensity measurements might be used to retrieve the phase information. Phase retrieval from intensity data is an independent area of research with efforts to find an efficient, fast and accurate method from minimum number of intensity measurements [30, 37, 42]. Examples of techniques available that transform the intensity measurements into phase information are:

- Interferometry [43–45],
- Constraints equation methods [46–48], and
- Iterative Fourier Algorithms [37, 42, 49].

These techniques are either very technically demanding or too time consuming for the real time implementation in the semiconductor industry.

As stated in earlier chapters, in CFS the light from a coherent source is focused onto the sample under test (here a grating) and the focused spot is scanned over the grating such that there is an overlap between the consecutive scan positions. For each scan position the far field intensity map is recorded and depending on the incident wavelength, numerical aperture of the focusing lens and period of the grating, there could be an overlap between one or several diffracted orders. In the last few years, we have investigated and implemented CFS, using a focused spot from a coherent source of light as illumination [32–34]. In Chapter 2 of the thesis it is shown that CFS is more sensitive than IOS provided that there is an overlap between the diffracted orders in the far field.

In this chapter, we show how the phase difference between overlapping diffracted orders of the grating for identical and orthogonal states of polarization can be retrieved. The setup resembles a common path interferometer and therefore the phase retrieval by our method is robust [44,50]. When there are overlapping orders present in the far field, the zeroth order diffracted beam acts as the reference beam and the higher diffracted orders act as the object beam. Phase shift between the zeroth and the higher diffracted order is achieved by scanning over the grating. We derive an analytic phase relationship between the diffracted orders of the reflected far field in terms of intensities acquired for different scan positions within

a single period of the grating. The situation is similar to Temporal Phase Shifting Interferometry (TPSI) [51,52]. TPSI requires capturing multiple interference patterns, generated at different times by shifting the phase of one of the interfering beams by a predetermined phase shift. In our case, the zeroth order diffracted beam acts as the reference beam and the phase shift between the zeroth and the higher diffracted order is achieved by translating the grating.

The content of the chapter is as follows: In Section 3.3, we present the mathematical formulation of the method. In Section 3.5 and in Section 3.6 the experimental setup is described and experimental and simulation results are given. Section 3.7 contains the conclusions.

3.3 Theoretical analysis

The geometrical representation of the periodic grating illuminated by a focused spot in CFS and the coordinate system in the entrance pupil and the focal plane of the the focusing objective are illustrated in Fig. 3.1. The shape of the grating is defined by the period, midCD, height and side wall angles (SWA) as shown in Fig. 3.2. As stated in the earlier chapter, the quantity 'bias' is defined as the position of the grating relative to the optical axis of the focusing system. The zero bias position here is taken as the position of the grating, when the optical axis bi-sects the midCD as indicated by the dotted vertical line in Fig. 3.2. It is to be mentioned that the choice of zero bias position is arbitrary. Throughout this chapter, we use a right-handed coordinate system (x, y, z) as shown in Fig. 3.1. The x-axis and y-axis are parallel and perpendicular to the spatial frequency vector \vec{q} of the grating, respectively, the z-axis is towards the optical axis of the focusing system with z increasing parallel to the direction of the incident field. A positive or negative bias value means that the grating is displaced in the direction of the positive or the negative x-axis, respectively over a distance specified by the absolute bias value. MidCD, height, SWA collectively are the grating parameters that we want to retrieve from the reflected data (see Fig. 3.2). In doing this we also have retrieved the bias value. In addition to the (x, y, z) system, we introduce the coordinate system (ξ, η, z) in the pupil of the focusing lens, where ξ is parallel to the x-axis and η is parallel to y-axis.

A focused light beam can be described conveniently by introducing a cylindrical coordinate system (ρ, φ, z) in the entrance pupil and a spherical coordinate system (θ, φ, z) at the focal plane represented by the Cartesian coordinate systems (ξ, η, z) and (x, y, z), respectively. While focusing an incident beam, a cylindrical coordinate system (incoming beam) is transformed into a spherical coordinate system (focused beam). Let (ξ^i, η^i) be a point in the entrance pupil of the lens and let $\vec{E}_{lens}^i(\xi^i, \eta^i)$ be the real electric field in the entrance pupil that is focused by the lens:

$$\begin{split} \vec{E}_{lens}^{i}(\xi^{i},\eta^{i}) &= \Re\left[\vec{a}^{i}\left(\xi^{i},\eta^{i}\right)\exp\left(-i\omega t\right)\right] \\ &= \Re\left\{\left[a_{\xi}^{i}\left(\xi^{i},\eta^{i}\right)\hat{\xi} + a_{\eta}^{i}\left(\xi^{i},\eta^{i}\right)\hat{\eta}\right]\exp\left(-i\omega t\right)\right\}, \end{split} \tag{3.1}$$

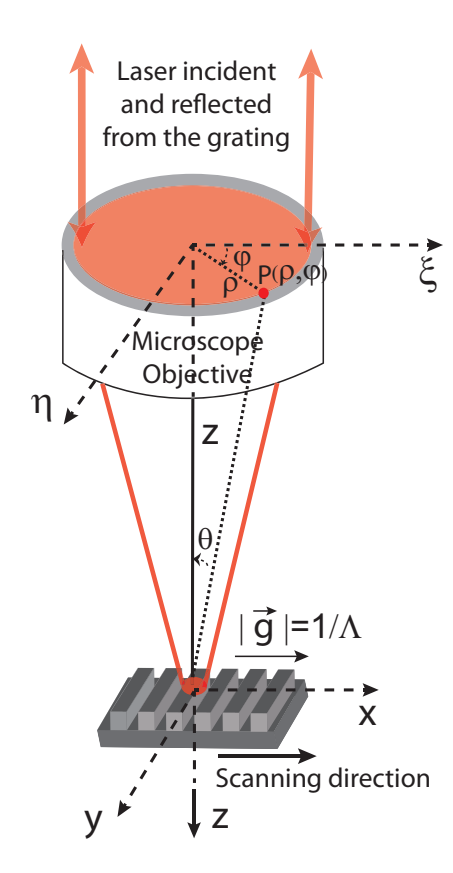


Figure 3.1: Geometrical representation of the periodic grating illumination using a focused spot in CFS and the coordinate system in the entrance pupil and the focal plane of the the focusing objective.

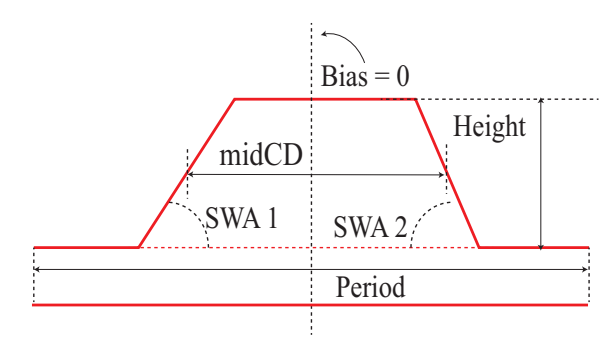


Figure 3.2: Cross-section along the (x-z) plane of a single period of the grating, showing the geometrical grating parameters: period, midCD, height and Sidewall angles (SWA).

where $\vec{a}^i(\xi^i, \eta^i)$ is the complex incident field in the entrance pupil. The field in Eqn. 3.1, is written as the sum of fields that are linearly polarized parallel to the $\hat{\xi}$ and $\hat{\eta}$ directions. We can also write the incident field $\vec{a}^i(\xi^i, \eta^i)$ as the sum of radially and azimuthally polarized fields:

$$\vec{a}^{i}(\xi^{i}, \eta^{i}) = a_{\rho}^{i}(\xi^{i}, \eta^{i})\,\hat{\rho} + a_{\varphi}^{i}(\xi^{i}, \eta^{i})\,\hat{\varphi}. \tag{3.2}$$

where, ρ and φ are polar coordinates and

$$\hat{\rho} = \cos \varphi \hat{\xi} + \sin \varphi \hat{\eta},
\hat{\varphi} = -\sin \varphi \hat{\xi} + \cos \varphi \hat{\eta},
\xi^{i} = \rho_{i} \cos \varphi^{i}, \quad \eta^{i} = \rho_{i} \sin \varphi^{i}.$$
(3.3)

The relation between the amplitude in the cylindrical and Cartesian coordinates is given by

$$\begin{pmatrix} a_{\xi}^{i} \\ a_{\eta}^{i} \end{pmatrix} = \begin{pmatrix} \cos \varphi^{i} & -\sin \varphi^{i} \\ \sin \varphi^{i} & \cos \varphi^{i} \end{pmatrix} \begin{pmatrix} a_{\rho}^{i} \\ a_{\varphi}^{i} \end{pmatrix} \equiv \underline{\underline{\Omega}} \left(\varphi^{i} \right) \begin{pmatrix} a_{\rho}^{i} \\ a_{\varphi}^{i} \end{pmatrix}. \tag{3.4}$$

To a given point (ξ^i, η^i) in the entrance pupil of the lens, there corresponds an incident plane wave with wavevector \vec{k}^i in the angular spectrum of the focused spot, which is given by

$$\vec{k}^{i} = k_{x}^{i}\hat{x} + k_{y}^{i}\hat{y} + k_{z}^{i}\hat{z}, \tag{3.5}$$

with:

$$k_{x}^{i} = -k_{0}n\frac{\xi^{i}}{f},$$

$$k_{y}^{i} = -k_{0}n\frac{\eta^{i}}{f},$$

$$k_{z}^{i} = \sqrt{k_{0}^{2}n^{2} - k_{x}^{i}^{2} - k_{y}^{i}^{2}},$$

$$(3.6)$$

where k_0 is the wavenumber in vacuum, f is the focal length of the focusing lens and n is the refractive index of the medium between lens and the grating (in our case n=1). Assuming an aplanatic lens [53], it follows from the theory of Ignatowski [54] and Richards & Wolf [55] that the radial and azimuthal components in the entrance pupil are transferred by the lens into P and S polarized electric field vectors, respectively. Let (θ, φ) be spherical coordinates, such that

$$k_x^i = k_0 n \cos \varphi^i \sin \theta^i,$$

$$k_y^i = k_0 n \sin \varphi^i \sin \theta^i,$$

$$k_z^i = k_0 n \cos \theta^i.$$
(3.7)

Then, the electric vector of the plane wave \hat{k}^i in the focal plane is,

$$\vec{E}^{i}(k_{x}^{i}, k_{y}^{i}) = \sqrt{\cos \theta^{i}} \left[a_{\rho}^{i} \left(\xi^{i}, \eta^{i} \right) \hat{\theta} + a_{\varphi}^{i} \left(\xi^{i}, \eta^{i} \right) \hat{\varphi} \right]. \tag{3.8}$$

The factor $\sqrt{\cos \theta^i}$ is due to the conservation of energy flux [53].

In the remainder of this chapter, we assume that the state of polarization, the amplitude and the phase of the incident pupil field have been determined. This means that $\vec{a}_{\xi}^{i}(\xi^{i},\eta^{i})$ and $\vec{a}_{\eta}^{i}(\xi^{i},\eta^{i})$ are known complex functions of position (ξ^{i},η^{i}) in the pupil. The incident plane wave with wavevector (Eqn. 3.7) is partially reflected by the grating giving rise to the reflected propagating orders with wavevector

$$\vec{k}^{s,m} = k_x^{s,m} \hat{x} + k_y^{s,m} \hat{y} - k_z^{s,m} \hat{z}$$

$$= \left(k_x^i + \frac{2\pi m}{\Lambda} \right) \hat{x} + k_y^i \hat{y} - k_z^{s,m} \hat{z}, \tag{3.9}$$

where the superscript s refers to the scattered field, Λ is the pitch of the grating, m is an integer representing the diffracted order such that

$$\left(k_x^i + \frac{2\pi m}{\Lambda}\right)^2 + k_y^{i^2} \le (k_0 n)^2, \tag{3.10}$$

and

$$k_z^{s,m} = \sqrt{k_0^2 n^2 - \left(k_x^i + \frac{2\pi m}{\Lambda}\right)^2 - \left(k_y^i\right)^2}.$$
 (3.11)

The electric field of the m^{th} diffracted order is written as

$$\vec{E}^{s,m}\left(k_x^{s,m}, k_y^{s,m}\right) = \underline{r}_{m}\left(k_x^{i}, k_y^{i}\right) \vec{E}^{i}\left(k_x^{i}, k_y^{i}\right), \tag{3.12}$$

where, $\underline{\underline{r}}_m(k_x^i, k_y^i)$ is a (2×2) matrix on the $(\hat{\theta}, \hat{\varphi})$ bases that relates the incident electric vector and the electric field vector of the m^{th} order. We can write

$$k_x^{s,m} = k_0 n \cos \varphi^{s,m} \sin \theta^{s,m},$$

$$k_y^{s,m} = k_0 n \sin \varphi^{s,m} \sin \theta^{s,m},$$

$$k_z^{s,m} = -k_0 n \cos \theta^{s,m}.$$
(3.13)

The information about the grating is contained in the matrices $\underline{r}_m(k_x^i, k_y^i)$, and hence it is important to retrieve as much information as possible (amplitude and phase) about these matrices to reconstruct the grating parameters. The reflected orders are collected back by the same focusing objective and the far field is captured by the CCD. By inverting Eqn. 3.8, we obtain the electric field $\vec{a}^{s,m}$ of the m^{th} reflected order in the exit pupil of the collimator:

$$\vec{a}^{s,m}\left(\xi^{s,m},\eta^{s,m}\right) = \frac{1}{\sqrt{\cos\theta^{s,m}}} \left[\vec{E}_{\theta}^{s,m} \left(k_x^{s,m}, k_y^{s,m}\right) \hat{\rho} + \vec{E}_{\varphi}^{s,m} \left(k_x^{s,m}, k_y^{s,m}\right) \hat{\varphi} \right], \tag{3.14}$$

where,

$$\xi^{s,m} = -\frac{k_x^{s,m}}{k_0 n} f,
\eta^{s,m} = -\frac{k_y^{s,m}}{k_0 n} f.$$
(3.15)

Using Eqns. (3.8, 3.12 and 3.14), we find that the (ξ, η) -components of the reflected and the incident fields in the pupil are related as follows:

$$\begin{pmatrix}
a_{\xi}^{s,m}(\xi^{s,m}, \eta^{s,m}) \\
a_{\eta}^{s,m}(\xi^{s,m}, \eta^{s,m})
\end{pmatrix} = \sqrt{\frac{\cos \theta^{i}}{\cos \theta^{s,m}}} \underline{\underline{\Omega}} (\varphi^{s,m}) \underline{\underline{r}}_{m} (k_{x}^{i}, k_{y}^{i}) \underline{\underline{\Omega}} (\varphi^{i})^{-1} \begin{pmatrix} a_{\xi}^{i}(\xi^{i}, \eta^{i}) \\ a_{\eta}^{i}(\xi^{i}, \eta^{i}) \end{pmatrix}$$

$$= \underline{\widetilde{r}}_{m} (k_{x}^{i}, k_{y}^{i}) \begin{pmatrix} a_{\xi}^{i}(\xi^{i}, \eta^{i}) \\ a_{y}^{i}(\xi^{i}, \eta^{i}) \end{pmatrix}, \tag{3.16}$$

where.

$$\underline{\widetilde{r}}_{m}\left(k_{x}^{i}, k_{y}^{i}\right) = \sqrt{\frac{\cos\theta^{i}}{\cos\theta^{s,m}}} \underline{\underline{\Omega}}\left(\varphi^{s,m}\right) \underline{\underline{r}}_{m}\left(k_{x}^{i}, k_{y}^{i}\right) \underline{\underline{\Omega}}\left(\varphi^{i}\right)^{-1}.$$
(3.17)

Here $\widetilde{\underline{\underline{r}}}_m(k_x^i, k_y^i)$ is the reflection matrix that relates the field of the m^{th} reflected order in the pupil of the objective to the incident field in the pupil.

Let us now look at a fixed scattering direction given by the wave vector $\vec{k}^s = k_x^s \hat{x} + k_y^s \hat{y} - k_z^s \hat{z}$. The corresponding point (ξ^s, η^s) in the exit pupil is

$$\xi^{s} = \frac{-k_{x}^{s}}{k_{0}n}f, \quad \eta^{s} = \frac{-k_{y}^{s}}{k_{0}n}f.$$

It has been shown that, when there is no overlap between diffracted orders, CFS and IOS are equivalent [32]. When there is an overlap between diffracted orders, CFS gives better sensitivity and more accurate reconstruction of the grating parameters provided scanning is applied [32, 33]. The number of overlapping orders is determined by the value of the so called overlap parameter defined as:

$$F = \frac{\lambda}{\Lambda \cdot NA}.\tag{3.18}$$

The smaller the value of F, the more orders overlap. In particular, for $1 \le F \le 2$ only the zeroth and first order overlaps in part of the exit pupil while the first and minus first diffracted orders never overlap and all higher diffracted orders are either evanescent or not captured by the lens. For simplicity, in the remainder of this paper we assume that $1 \le F \le 2$ but the analysis can be extended to other values of F when more orders overlap.

3.3.1 Pupil points with no overlapping orders

For a particular point (ξ^s, η^s) in a region without overlapping orders, only the specular reflected wave contributes to the measured intensity. Hence the total field in such a pupil point is given by

$$\begin{pmatrix}
a_{\xi}^{s,0}(\xi^{s},\eta^{s}) \\
a_{\eta}^{s,0}(\xi^{s},\eta^{s})
\end{pmatrix} = \widetilde{\underline{r}}_{0}\left(k_{x}^{i},k_{y}^{i}\right) \begin{pmatrix}
a_{\xi}^{i}(\xi^{i},\eta^{i}) \\
a_{\eta}^{i}(\xi^{i},\eta^{i})
\end{pmatrix},$$
(3.19)

where (k_x^i, k_y^i) is linked to (ξ^i, η^i) by Eqn. 3.6, and

$$\begin{cases}
\xi^s = -\xi^i, \\
\eta^s = -\eta^i.
\end{cases}$$
(3.20)

We write the complex matrix $\underline{\widetilde{r}}_0$ on the (ξ, η) basis as:

$$\widetilde{\underline{\underline{r}}}_{0} = \begin{pmatrix}
\widetilde{\underline{\underline{r}}}_{0,\xi\xi} & \widetilde{\underline{\underline{r}}}_{0,\xi\eta} \\
\widetilde{\underline{\underline{r}}}_{0,\eta\xi} & \widetilde{\underline{\underline{r}}}_{0,\eta\eta}
\end{pmatrix}.$$
(3.21)

The first index in the subscripts of the matrix elements corresponds to the input polarization while the second index corresponds to the output polarization. In order to retrieve the amplitudes of all four elements of the matrix $\tilde{\underline{r}}_0$ and their phase differences, two polarizers are used in the setup. In this way, the complex specular reflection matrix in the direction of a pupil point in a region without overlap can be completely retrieved except for an ambiguous common constant phase. We explain the procedure here briefly.

First, we use a linear polarizer in the incident beam just before the pupil and a linear polarizer in the reflected beam at the detector. By setting these polarizers alternatively parallel to the ξ and η axis and measuring the intensity, the moduli $|\underline{\widetilde{r}}_{0,\mu,\nu}|, \mu,\nu=\xi,\eta$ of all four elements of the reflection matrix are found. Then the phase difference between the elements of the reflection matrix are determined in the following way: we choose the polarizer in the incident beam parallel to the ξ axis and η axis alternatively and the polarizer in the reflected beam at 45^0 to the ξ and η axis and measure the intensity. From this, the phase difference between $\underline{\widetilde{r}}_{0,\xi\xi}, \underline{\widetilde{r}}_{0,\eta\xi}, \underline{\widetilde{r}}_{0,\eta\eta}$ are found. Then we put the input polarizer at 45^0 w.r.t ξ axis and the reflected intensity is measured with the polarizer parallel to ξ and η axis respectively at the detector. From this measurement the phase differences between $\underline{\widetilde{r}}_{0,\xi\xi}, \underline{\widetilde{r}}_{0,\eta\xi}$ and $\underline{\widetilde{r}}_{0,\xi\eta}, \underline{\widetilde{r}}_{0,\eta\eta}$ are found. In this way, the complex reflection matrix $\underline{\widetilde{r}}_{0}$ is determined except for an overall constant phase.

3.3.2 Pupil points where reflected orders overlap

Let (ξ^s,η^s) now be a point of the lens pupil where two reflected orders overlap (since we have assumed that 1 < F < 2, no more than two orders overlap). To be specific, let (ξ^s,η^s) be in the region of overlap of the 0^{th} (the specular reflected wave) and the 1^{st} reflected order. In this case, there is an incident wave with wave vector $\vec{k}^{i,0} = k_x^{i,0}\hat{x} + k_y^{i,0}\hat{y} + k_z^{i,0}\hat{z}$, such that $\left|\vec{k}^{i,0}\right| = \left|\vec{k}^s\right|$ and the corresponding pupil point $(\xi^{i,0},\eta^{i,0}) = (-\xi^s,-\eta^s)$, of which the specular reflected order is in the direction of \vec{k}^s . Furthermore there is an incident wave vector $\vec{k}^{i,1} = k_x^{i,1}\hat{x} + k_y^{i,1}\hat{y} + k_z^{i,1}\hat{z}$ with corresponding pupil point $(\xi^{i,1},\eta^{i,1}) = \left(-\frac{f}{k_0n}k_x^{i,1}, -\frac{f}{k_0n}k_y^{i,1}\right)$ of which the 1^{st} reflected order is in the direction of \vec{k}^s . There holds:

$$\vec{k}^{i,1} = \vec{k}^s - \frac{2\pi}{\lambda}\hat{x}.$$
 (3.22)

The total reflected electric field in point (ξ^s, η^s) of the exit pupil is the coherent sum of the field of the zeroth reflected order of incident wave vector $\vec{k}^{i,0}$ and the 1^{st} reflected order of the incident wave vector $\vec{k}^{i,1}$. Hence:

$$\vec{a}^{s}\left(\xi^{s},\eta^{s}\right) = \underbrace{\widetilde{\mathbb{E}}}_{0}\left(\xi^{i,0},\eta^{i,0}\right) \vec{a}^{i}\left(\xi^{i,0},\eta^{i,0}\right) + \underbrace{\widetilde{\mathbb{E}}}_{1}\left(\xi^{i,1},\eta^{i,1}\right) \vec{a}^{i}\left(\xi^{i,1},\eta^{i,1}\right). \tag{3.23}$$

This relation is valid for zero bias. When the grating is translated over the distance Δx with respect to the zero bias position, the phases of the reflection matrices change and then $\tilde{\underline{r}}_1$ gets an additional phase with respect to $\tilde{\underline{r}}_0$ given by,

$$\Delta\Phi = \frac{2\pi\Delta x}{\Lambda}.\tag{3.24}$$

The total reflected field in point (ξ^s, η^s) is then

$$\vec{a}^{s,\Delta x}\left(\xi^{s},\eta^{s}\right) = \underline{\widetilde{r}}_{0}\left(\xi^{i,0},\eta^{i,0}\right)\vec{a}^{i}\left(\xi^{i,0},\eta^{i,0}\right) + \underline{\widetilde{r}}_{1}\left(\xi^{i,1},\eta^{i,1}\right)\vec{a}^{i}\left(\xi^{i,1},\eta^{i,1}\right)\exp\left(\frac{i2\pi\Delta x}{\Lambda}\right).$$

$$(3.25)$$

We use again two polarizers in the setup: one in the incident beam immediately before the entrance pupil and the other in the reflected beam. First, suppose that both polarizers are parallel to ξ -direction. The measured reflected intensity for bias Δx is given by

$$I_{\xi\xi}^{\Delta x}(\xi^{s},\eta^{s}) = \left| \vec{a}^{s,\Delta x}(\xi^{s},\eta^{s}) \cdot \hat{\xi} \right|^{2}$$

$$= \left| \widetilde{\underline{\underline{r}}}_{0,\xi\xi}(\xi^{i,0},\eta^{i,0}) a_{\xi}^{i}(\xi^{i,0},\eta^{i,0}) \hat{\xi} \right|^{2} + \left| \widetilde{\underline{\underline{r}}}_{1,\xi\xi}(\xi^{i,1},\eta^{i,1}) a_{\xi}^{i}(\xi^{i,1},\eta^{i,1}) \hat{\xi} \right|^{2}$$

$$+ 2\Re \left[\widetilde{\underline{\underline{r}}}_{0,\xi\xi}(\xi^{i,0},\eta^{i,0}) a_{\xi}^{i}(\xi^{i,0},\eta^{i,0}) \hat{\xi} \times \widetilde{\underline{\underline{r}}}_{1,\xi\xi}(\xi^{i,1},\eta^{i,1})^{*} a_{\xi}^{i}(\xi^{i,1},\eta^{i,1})^{*} \hat{\xi} \right]$$

$$\times \exp \left(\frac{-i2\pi\Delta x}{\Lambda} \right), \qquad (3.26)$$

where the subscript $\xi\xi$ corresponds to ξ input and ξ output polarization respectively. As the incident field is assumed to be known, the unknown absolute values $|\underline{\widetilde{r}}_{0,\xi\xi}|$, $|\underline{\widetilde{r}}_{1,\xi\xi}|$ and the phase difference of $\underline{\widetilde{r}}_{0,\xi\xi}$ and $\underline{\widetilde{r}}_{1,\xi\xi}$ can be determined from measuring $I_{\xi\xi}^{\Delta x}$ for (at least) three scan positions Δx . By setting the linear polarizers alternatively parallel to the ξ - and η -axis we obtain the moduli and phase differences of all elements of the two reflection matrices in the same row and column, i.e., of all $\underline{\widetilde{r}}_{0,\mu\nu}$ and $\underline{\widetilde{r}}_{1,\mu\nu}$ for $\mu,\nu=\xi,\eta$. Note that when Δx is such that the corresponding phase change $\Delta\Phi$ is in steps of

Note that when Δx is such that the corresponding phase change $\Delta \Phi$ is in steps of $\pi/2$, we can implement the bucket algorithm for phase retrieval [52]. Let the 0^{th} and 1^{st} diffracted orders be the reference and the object beam respectively in the shear interferometer. The phase retrieval is thus very similar to TPSI, where one of the interfering beams is shifted by a phase difference of $\pi/2$.

Generalizing the preceding scanning method to the case of more than two overlapping orders is straightforward. Due to a translation over Δx , the reflection matrix of the m^{th} reflected order obtains a relative phase change with respect to the reflection matrix of the spurious (i.e. 0^{th}) order matrix given by:

$$\Delta \Phi_m = \frac{2\pi m \Delta x}{\Lambda}.\tag{3.27}$$

When there are in total M overlapping orders contributing to the total reflected field in a particular point of the lens pupil, we need at least (2M+1) scan positions to retrieve all amplitudes and phase differences of the reflection matrices.

By the described scanning procedure we have retrieved the absolute values of all elements in the same row and column of the contributing reflection matrices $\underline{\tilde{r}}_0$ and $\underline{\tilde{r}}_1$ and the phase differences between them. Next, we want to determine the phase differences between elements in different rows and columns. This is done as described previously. By setting the polarizer in the incident beam parallel to the ξ axis and that in the outgoing beam under 45° to the ξ axis, we can retrieve the phase difference between the total field components

$$\underline{\widetilde{\underline{r}}}_{0,\xi\xi}(\xi^{i,0},\eta^{i,0})a_{\xi}^{i}(\xi^{i,0},\eta^{i,0}) + \underline{\widetilde{\underline{r}}}_{1,\xi\xi}(\xi^{i,1},\eta^{i,1})a_{\xi}^{i}(\xi^{i,1},\eta^{i,1}), \tag{3.28}$$

and

Since the complex incident field \vec{a}^i is assumed known and the amplitudes and phase difference of $\underline{\widetilde{r}}_{0,\mu\xi}$ and $\underline{\widetilde{r}}_{1,\mu\xi}$ have already been determined for $\mu=\xi,\eta$, we can retrieve the phase differences of all four reflection coefficients.

By repeating this procedure for a linear polarizer parallel to the η axis in the incident beam, we retrieve similarly the phase differences between $\underline{\widetilde{r}}_{0,\mu\eta}$ and $\underline{\widetilde{r}}_{1,\mu\eta}$ for $\mu=\xi,\eta$. Hence the phase differences between all elements of the reflection matrices $\underline{\widetilde{r}}_0$ and $\underline{\widetilde{r}}_1$ that are in different rows but the same column are retrieved. Finally, we insert a polarizer in the reflected beam and subsequently use in the incident beam a polarizer at 45^0 to obtain the phase differences between the elements of the two reflection matrices that are in different columns but the same row. We conclude that the complex reflection matrices $\underline{\widetilde{r}}_0$ and $\underline{\widetilde{r}}_1$ can be retrieved except for a common phase.

3.3.3 Summary

In summary, for points in the region of the pupil without overlapping of reflected orders, only the specular reflected field contributes. Hence only the reflection matrix $\widetilde{\underline{r}}_0$ influences the measurements. Using linear polarizers and a half wave plate, the polarization of the field is rotated and with the procedure described above, the complex elements of this reflection matrix are retrieved except for a common phase.

For points in the pupil for which several orders overlap, a number of reflection matrices $\widetilde{\underline{r}}_j$, $j=1,\ldots,M$ contribute. By using 2M+1 scan positions and using the procedure with the linear polarizers and the half wave plate in the incident and reflected beams, we can retrieve all contributing complex reflection matrices except for a common constant phase.

In case F>2, for all points of the pupil of the lens, only the specular reflected wave contributes. Hence when F>2 there is no region of overlap of reflected orders inside the pupil and scanning of the spot is superfluous.

3.4 Phase difference between overlapping orders

For the forward problems in CFS, in which the far field intensity pattern generated by computing the interaction of an incident field and the grating, a rigorous numerical method for Maxwell's equations must be used. To simulate the far field intensity, we use rigorous coupled wave analysis (RCWA) as the Maxwell solver [56]. The complex field amplitude of the diffracted orders in the far field are obtained from the RCWA computation, of which the squared modulus gives the diffraction efficiency of the individual orders. Hence with RCWA computation phase differences between diffracted orders are known and can be used to validate the theory presented in Section 3.3. In experiments only intensities are measured and consequently there is no explicit phase information available.

As shown in Section 3.3, phase differences between the overlapping orders in CFS can be retrieved from intensity measurements by scanning the sample with a focused spot. Figures 3.4 and 3.6 show simulated far field intensity maps for incident field with uniform illumination and constant phase in the entrance pupil of the focusing objective. The four far field intensity maps $I^{\Delta x_0}$, $I^{\Delta x_1}$, $I^{\Delta x_2}$ and $I^{\Delta x_3}$ as shown in Figs. 3.4 and 3.6 correspond to four distinct scanning positions of the focused spot on the grating within a single period for a defined incident polarization in the entrance pupil and the polarizer orientation at the detector. The input and output polarization are represented namely by ξ_{in}/ξ_{out} and η_{in}/η_{out} . The grating vector \vec{q} is defined parallel to the ξ axis as shown in Fig. 3.1. The scan positions are separated by a quarter of the period $(\Lambda/4)$ of the grating. Figures 3.5 and 3.7 presents the phase difference between the diffracted overlapping orders in the exit pupil of the lens for ξ_{in}/ξ_{out} and η_{in}/η_{out} set of polarizations. Figures 3.5a and 3.7a show the phase difference computed directly from RCWA phase information, while Figs. 3.5b and 3.7b show the phase difference between overlapping orders retrieved from only intensity data.

The simulation parameters for the silicon grating (Fig. 3.3) are the following:

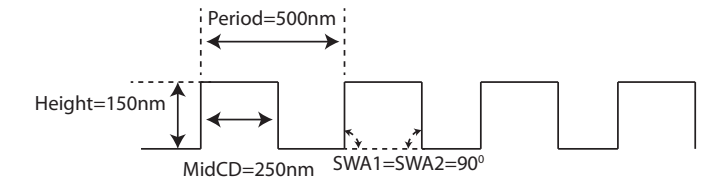


Figure 3.3: Grating parameters.

1. Illumination conditions

- (a) Incident wavelength (λ): 633 nm
- (b) Numerical Aperture of the focusing lens: 0.95
- (c) Input/Output polarization: ξ/ξ , η/η

2. The grating shape parameters

- (a) Period of the grating (Λ): 500 nm
- (b) midCD of the grating: 250 nm
- (c) Height of the grating: 150 nm
- (d) Sidewall angles (SWA1 and SWA2) of the grating: 90 degrees

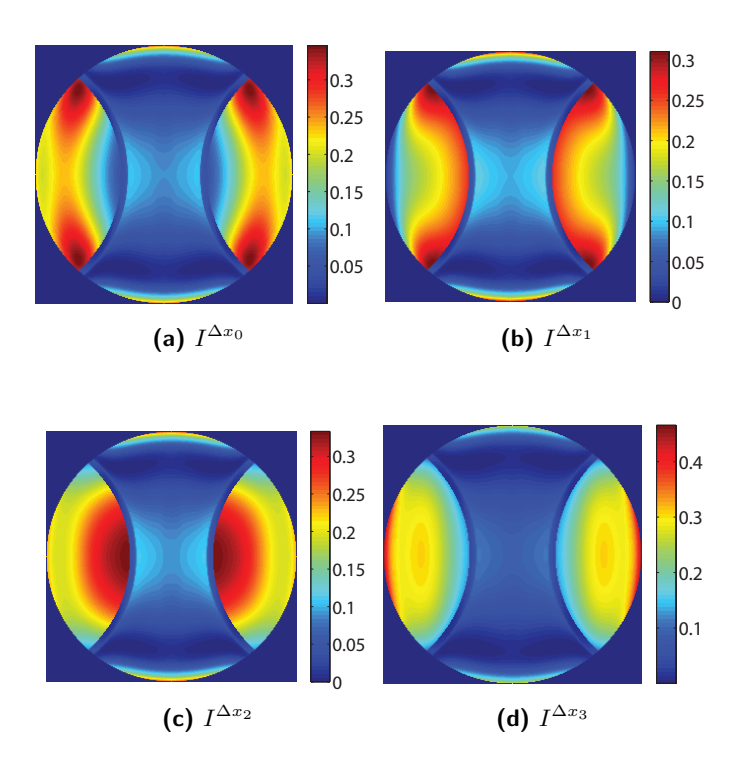


Figure 3.4: Far field intensity maps for focus positions separated by $\Lambda/4$ within a single period of the grating. The input and output polarizations in the entrance and exit pupil are along ξ (see Fig 3.1, ξ input and ξ output polarization).

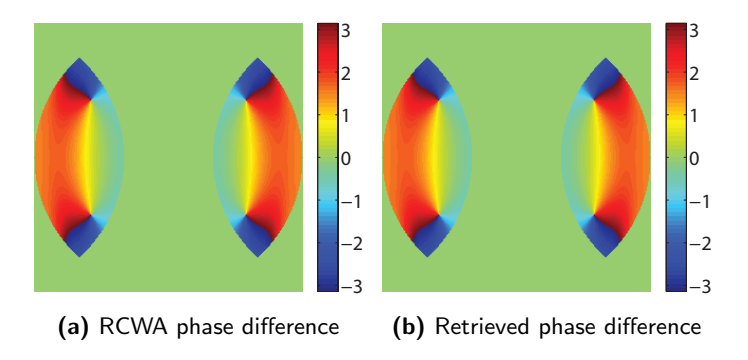


Figure 3.5: Phase difference between the overlapping orders for ξ input and ξ output polarizations, respectively.

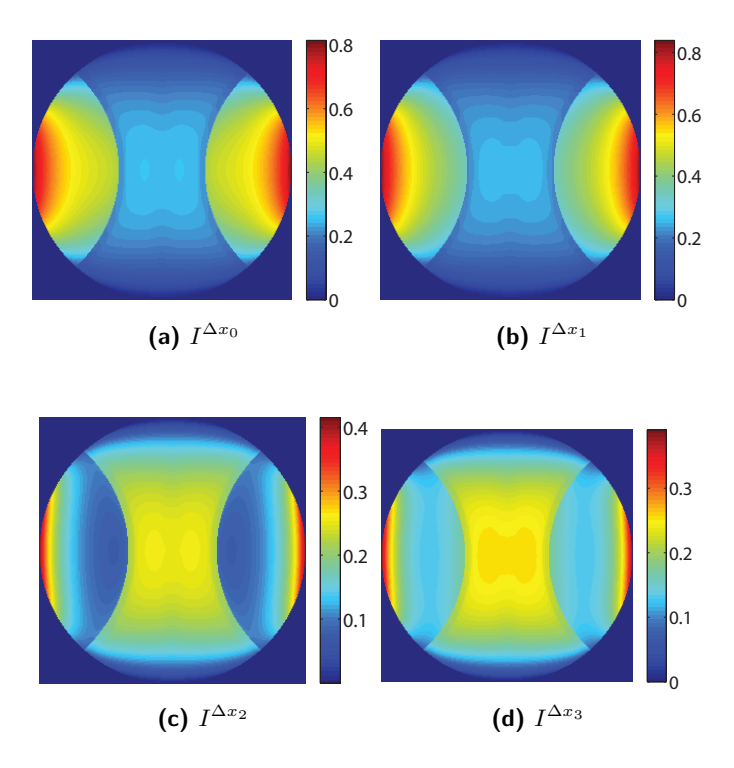


Figure 3.6: Far field intensity maps for focus positions separated by $\Lambda/4$ within a single period of the grating. The input and output polarizations in the entrance and exit pupil are along η (see Fig 3.1, η input and η output polarization).

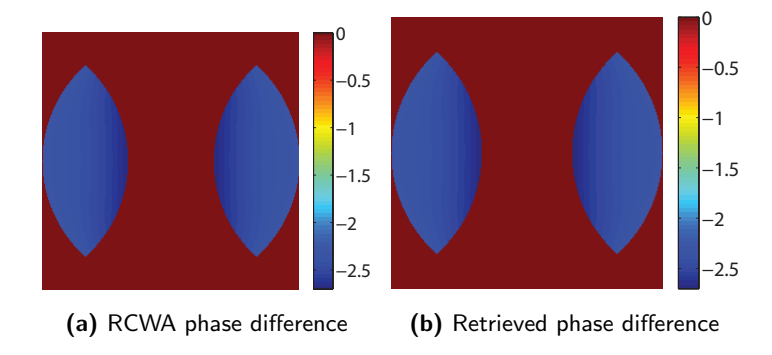


Figure 3.7: Phase difference between the overlapping orders for η input and η output polarizations, respectively.

The results from analytic phase retrieval from far field intensity maps are shown. It is to be observed that, the phase difference between the overlapping orders has more structural variations for polarization configuration ξ_{in}/ξ_{out} compared to η_{in}/η_{out} for the chosen grating. Also, with change in grating parameters the sensitivity to phase difference is different for all parameters depending upon the nominal grating parameters and the polarization configuration. Polarization dependent specific phase sensitivity of grating parameters is discussed in Section 3.5.

3.5 Polarization specific phase sensitivity

When the illumination conditions and refractive index of the grating materials are well known in advance then the far field intensity maps are characteristics of the grating parameters only. Change in the shape parameters of the grating results in variation of diffraction efficiency of the propagating orders. There is a non linear change in far field intensity and the retrieved phase with the change in the shape parameters.

Figure. 3.8 summarizes the polarization specific phase sensitivity for the grating parameters, midCD, height, SWA and bias for the phase retrieved between overlapping orders from the far field intensity maps. The nominal values of the grating parameters are listed in Table. 3.1. In the computation of the sensitivity, individual grating parameters are varied over $\pm 5\%$ ($\pm 10\%$ for bias) from their nominal values. The phase map is then computed from the intensity maps for the nominal and the modified grating parameters for different set of input and output polarization given by ξ_{in}/ξ_{out} , ξ_{in}/η_{out} , η_{in}/ξ_{out} and η_{in}/η_{out} . Peak to Valley (PV) difference of the retrieved phase map corresponding to nominal and nonnominal parameters are plotted against the change in grating parameters. The PV difference is shown on the vertical axis of Fig. 3.8, while the horizontal axis represent the "%" change in grating parameters.

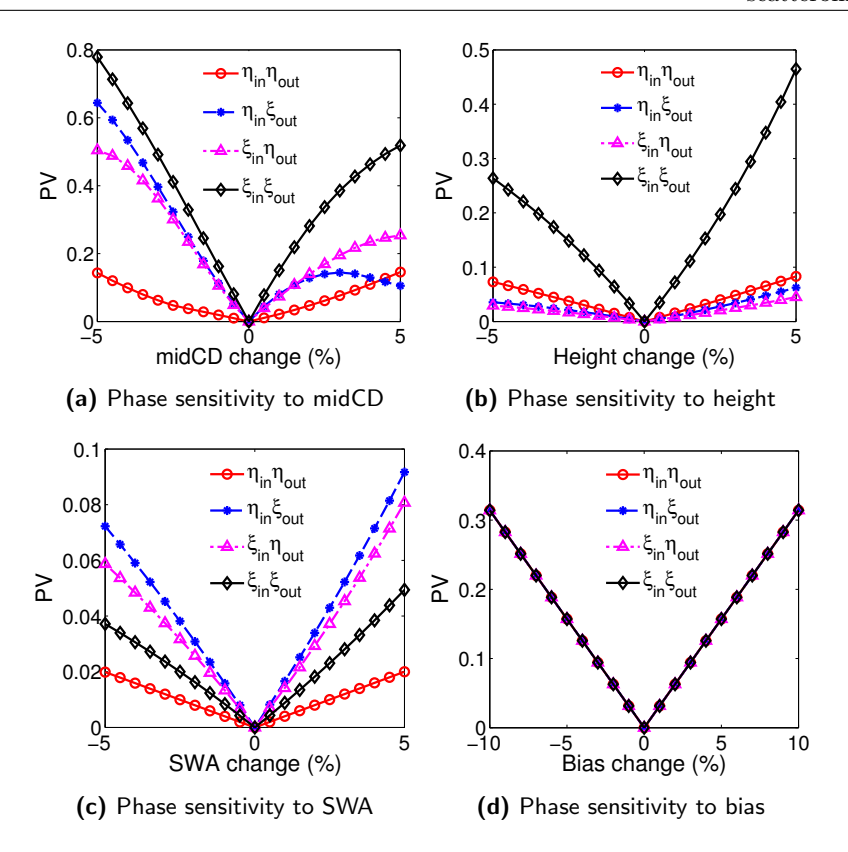


Figure 3.8: Polarization dependent phase sensitivity for grating parameters midCD, Height, SWA and Bias for different set of input and output polarizations.

Grating Parameters	Nominal values
Period	$1~\mu\mathrm{m}$
MidCD	425 nm
Height	158 nm
SWA	90^{0}

Table 3.1: Nominal grating parameters used in experiment and simulation

We observe that the grating parameters midCD (3.8a) and height (3.8b) are most sensitive for ξ_{in}/ξ_{out} polarization, while SWA (3.8c) sensitivity is maximum for crossed polarization namely η_{in}/ξ_{out} . Position dependency i.e., bias (3.8d) shows identical sensitivity to all sets of incident and output polarizations. These results can be explained as follows: As discussed in Section 3.4, the phase between overlapping orders have more structural variation for set ξ_{in}/ξ_{out} compared to the η_{in}/η_{out} polarizations. A constant phase in the far field is added to all the

respective orders depending upon the translation of the grating, which explains the identical response of bias to the polarization dependent phase sensitivity.

3.6 Experimental realization

In Section 3.3, the theory for analytic phase retrieval between the overlapping scattered orders was derived and compared to direct RCWA computation of the phase of the diffracted field in Section 3.4 to validate the theory. In the present section, we retrieve the phase from measured intensities and compare it to the phase retrieved by the intensity maps computed by a RCWA solver. Figure 3.9

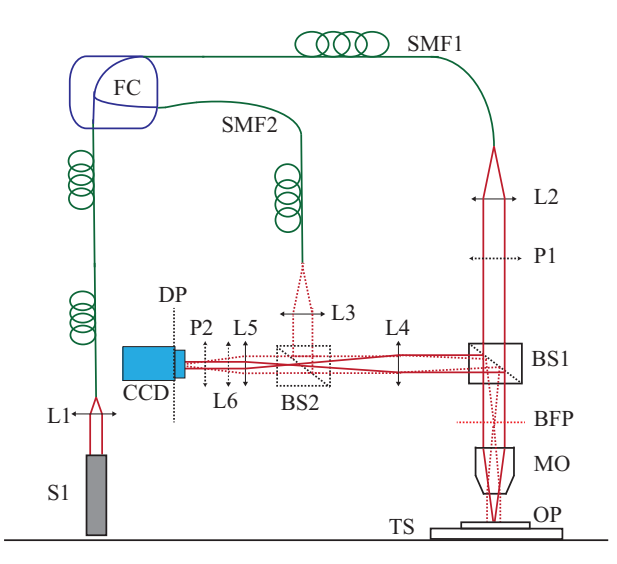


Figure 3.9: Schematics of the experimental setup. S1: He-Ne laser, FC: Fiber coupler, SMF: Single mode fiber, BS: Beam splitter, P: polarizer, L: lens, DP: Detector Plane, BFP: Back focal plane, OP: Object plane (grating),MO: Microscope objective, TS: Translation stage.

shows the experimental setup. Linearly polarized light from a He-Ne laser (S1) is coupled to a fiber beam splitter (FC). The two output channels from the fiber coupler are indicated in the Fig. 3.9 as SMF1 and SMF2. SMF1 is the illumination arm and SMF2 is the alignment arm in the setup. The polarizer (P1) selects the incident polarization of the collimated beam from SMF1. The polarized beam is then focused on the grating with a microscope objective (MO) of numerical aperture 0.4 (Leica: N PLAN L 20x/0.40). The radius of the focused spot is $\approx 0.95 \mu m$. The grating is placed on a piezo-controlled translation stage that is used to scan the bias positions. After interaction, the scattered light is collected by the same microscope objective. The far field is registered at the CCD plane after passing through the telescopic lens system L4 and L5. The telescopic system de-magnifies the beam and also images the far field in the back focal plane of the MO to the

CCD. The output polarization of the reflected wave is selected by polarizer (P2) placed before the CCD. A collimated beam from SMF2 is used for alignment of L4 of the telescopic system. Focal point of L4 is aligned to the back focal plane of the microscope objective. L5 is aligned by measuring the collimation after the telescopic system, when the collimated beam from SMF1 is focused on the plane of the Si wafer acting as the mirror. The present telescopic system is a de-magnifier of 2.5 X. L6 can also be used for imaging the wafer with SMF2 illumination, and it is removed in the process of data acquisition. The grating parameters used in the simulations and experiment are given in Table. 3.1. The far field intensity maps registered at the CCD, along with the phase retrieved between the overlapping orders are compared to the RCWA simulations.

To predict the output with the RCWA solver, we use the known incident field

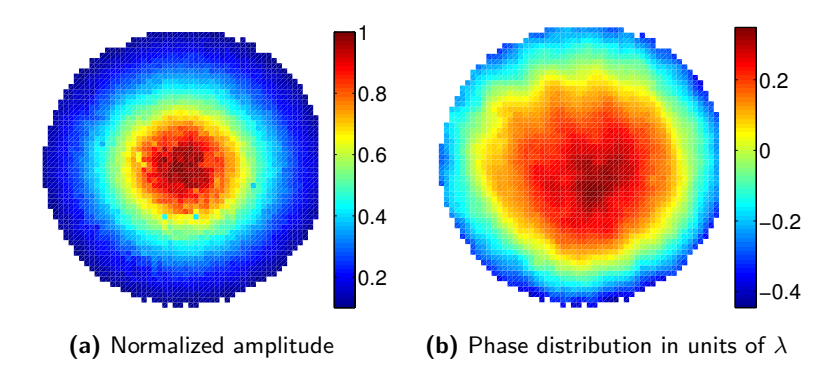


Figure 3.10: Shack-Hartmann measurement of the incident field above the microscope objective (MO). Radius of the entrance pupil is 4 mm.

over the entrance pupil of the focusing lens. The amplitude and phase of the incident field is measured with a Shack-Hartmann sensor as shown in Fig. 3.10. The measured amplitude and phase is then used for simulation of far field intensity maps for a set of known grating parameters for all sets of input and output polarization. The experimental results shown in Fig. 3.11 are restricted to the case of the η_{in}/η_{out} polarization.

In the top row of Fig. 3.11, the measured far field intensities corresponding to the five scan positions within a single period of the grating and the phase map computed analytically from the far field intensity maps are shown. In the bottom row the simulated data is shown. The separation between two adjacent scanning positions is $\Lambda/4$, hence the fifth and the first far fields are almost identical. Based on simulation studies, it is observed that the phase map is robust to the noise of the system. We assume that the intensity is normally distributed with standard deviations given by $\sigma=2.7\times10^{-3}$ from the measured data. Experimental and the simulated far fields correspond to a fixed bias value of the grating. As one can see, most features predicted in simulations are observed in the experiment. The

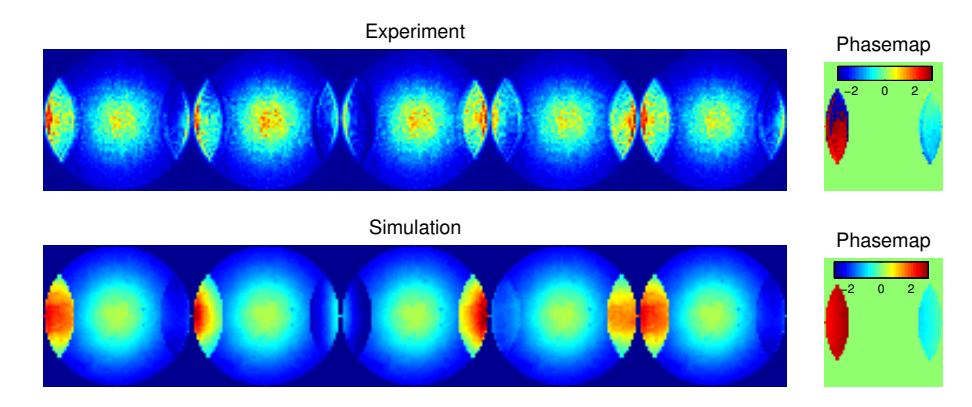


Figure 3.11: Comparison between experimental and simulation results (for NA 0.4). The top row shows the experimental far fields corresponding to five scan positions within a single period of the grating and the phase map computed from the far fields. In the bottom row shows the corresponding simulated data. Simulations and experiments were performed for η_{in}/η_{out} polarization.

phase map on the right side of the Fig. 3.11 are obtained by the analysis given in appendix. We also see that the information content of the phase map is limited to the overlap regions of the diffracted orders, as expected.

3.7 Discussion and Conclusions

The distribution in phase map is dependent upon the geometrical parameters of the grating and the bias. The phase dependency on the geometrical parameters can be used in grating reconstruction in addition to the intensity data. The combined effect of intensity and phase map can be used to more robust grating reconstruction. Also the bias dependency on the phase map can be utilized for very accurate positioning of the gratings in for example, alignment, overlay metrology and nanopatterning. Intensity data with phase between scattered orders is the maximum information that can be extracted in CFS, as we have the amplitude and phase of all the four components of the scattering matrix except for an overall phase. This overall phase can be retrieved with CFS in combination with, for example interferometry.

In conclusion, the applicability of Temporal Phase Shifting Interferometry in Coherent Fourier Scatterometry with a scanning spot is presented. An analytical relation is derived and illustrated for the phase difference between two overlapping orders in the exit pupil. An experimental set up was built to demonstrate the principle and the results were compared with rigorous simulations. The polarization dependent phase sensitivity of the grating parameters is presented. The importance of phase information in inverse problem of grating reconstruction is highlighted and the maximum information content of the CFS with a scanning

spot is discussed.

Reconstruction of sub-wavelength features and nano-positioning of gratings using coherent Fourier scatterometry

4.1 Abstract

In this chapter, we report on the implementation of an operational CFS instrument, which confirms the predicted performances discussed in earlier chapters. The system, although currently operating at a relatively low numerical aperture (NA = 0.4) and long wavelength (633 nm) allows already the reconstruction of the grating parameters with nanometer accuracy, which is comparable to that of AFM and SEM measurements on the same sample, used as reference measurements. Additionally, 1 nm accuracy in lateral positioning is proven, which corresponds to only 0.08% of the pitch of the grating used in the actual experiment.¹

 $^{^1{\}rm This}$ chapter is based on the studies and results published in [57].

4.2. Introduction 53

4.2 Introduction

Grating reconstruction in CFS requires to solve direct and inverse problems. When the feature size of the grating is either of the order of wavelength or sub-wavelength, then the grating reconstruction is particularly complicated. The direct problem is the prediction of the scattered intensity on the basis of known or assumed material and geometrical parameters of the grating and the inverse problem is to reconstruct these parameters from the scattered fields. Solving the direct problem requires a rigorous Maxwell solver. For the inverse problems there are the inherent issues of the uniqueness and stability of the solutions [5]. For example, the grating parameters can be highly correlated. Due to the ill posedness of the inverse problems in optical scattering, there are still open questions to its accuracy, implementation, usability and stability. Although, CFS has an additional phase information in the scattered light, we will address the following questions:

- Can the geometrical profile of the grating be reconstructed from noisy experimental data?
- Is speckle a critical issue in CFS?
- Is phase information useful and to what extent?
- Being a phase sensitive technique, can it CFS be used for nano positioning instead of interferometry?
- Can CFS be used for characterizing unintentional surface over-layers (for example: native oxide layer) on the wafer?

4.3 Model of the grating, illumination and data acquisition scheme

In CFS, here light from a coherent source is focused on periodic targets (for example: a gratings) on the wafer. The focused spot interacts with the grating and the far field is recorded [58]. In this way, the angular spectrum of the scattered fields are recorded at once for all the incident plane waves within the extent of the focused spot. The basic principle of data acquisition is illustrated in Fig. 4.1. In the event of overlapping reflected orders in the lens pupil, there is an interference between them and some phase information is automatically registered [39]. The phase difference between the overlapping orders can be retrieved by scanning the grating with the spot. The number of scanning positions required to resolve the phase depends upon the maximum number of overlapping orders in scattering direction i.e., at any point of the pupil of the objective lens. Since the technique relies on the acquisition of the diffracted far field, methods to model the interaction between incident focused spot and the grating, which gives rise to such far field, must be implemented. This task, which is modeling of the forward problem, is typically performed by means of a rigorous electromagnetic solver (Fig. 4.1). For the physical model of the grating, let us consider an infinitely long (along the x-axis) one-dimensional grating with period Λ , which is invariant along the y-axis as shown in Fig. 4.1. The grating profile can be described as:

$$z = f(x). (4.1)$$

where z denotes the height of the grating at position x. The geometrical shape of the grating is defined by the parameters height, midCD (width of the grating lines at half of the height) and side wall angle (SWA). Since, we use a focused spot, the position of the spot with respect to the grating is to be determined as well. The bias is the displacement of the spot with respect to a nominal position. The bias is also determined from the scattering data and the scanning is then done with respect to the bias. Defined in this way, the bias directly provides information on the alignment of the wafer which the grating has been printed on. The nominal zero bias position can be chosen arbitrarily, and in our case, we choose it at the position where the optical axis of the microscope objective bisects the midCD. The grating parameters to be reconstructed are shown in Fig. 4.2.

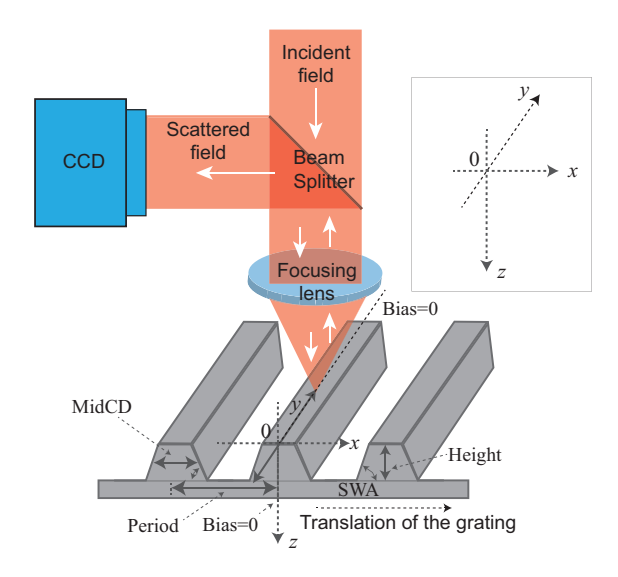


Figure 4.1: Scheme of the CFS illumination, data acquisition system and the grating parameters.

An incident collimated light beam with a well-defined polarization state in the entrance pupil of the lens is focused on the grating. Subsequently after interaction, propagating reflected orders within the extent of the numerical aperture of the lens are captured and collimated. The collimated light called far field is then relayed to the CCD camera.

The total number of diffracted orders in the exit pupil of the lens depends upon the wavelength (λ) of the incident light, the numerical aperture (NA) of the lens and the period (Λ) of the grating. The amount of overlap between the diffracted

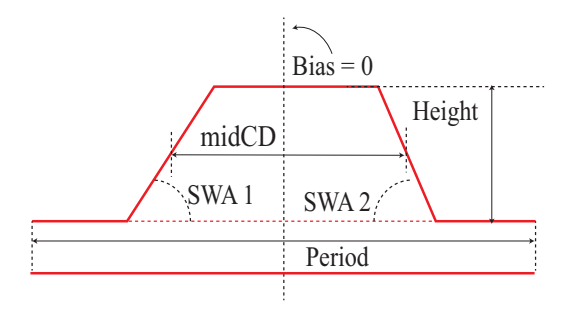


Figure 4.2: Grating parameters shown for crossection of the grating along x-z plane of a single period of the grating.

orders in the exit pupil of the focusing lens is defined by F,

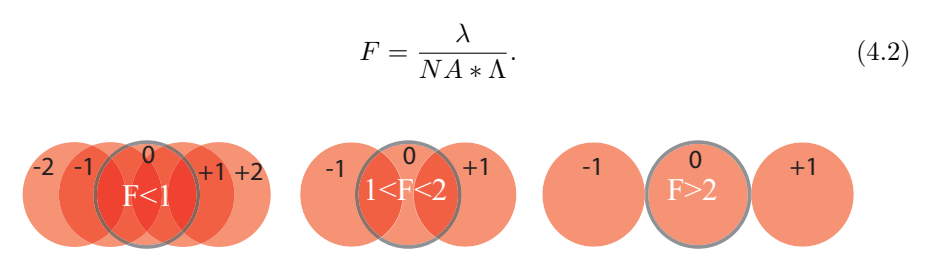


Figure 4.3: Overlap between the diffracted orders depending upon the value of the overlap parameter F. The NA of the lens is marked with black circles.

As shown in Fig. 4.3, at the lens pupil, for 1 < F < 2 there is an overlap between the 0^{th} and $\pm 1^{st}$ orders of the grating but no overlap between the -1^{st} and $+1^{st}$ reflected orders. For F < 1, however, there is an overlap between higher diffracted orders, while for F > 2, there is no overlap between the orders. To benefit from the phase sensitivity of CFS, there should be some overlap of reflected orders, hence, F < 2. Therefore if Λ is small, λ/NA should be reduced to make F < 2. In this chapter we will assume 1 < F < 2.

4.4 Grating fabrication

The periodic structure used in the experiment is an etched silicon grating. The grating was fabricated at VLL facility, TU delft. Fabrication steps for the grating are outlined in Fig. 4.4. In the first step, an electron beam sensitive resist is spin coated on a cleaned silicon wafer. The resist used was poly methyl methacrylate (PMMA, a synthetic polymer of methyl methacrylate). The grating pattern is then written into the resist using electron beam lithography. After development of the resist in a suitable developing agent (for example: MIB, Pentyl acetate etc.), the grating pattern is etched on the silicon wafer using a reactive ion etching system (F1 Leybold Fluor ethna), with SF_6 gas as the etchant. The remaining resist layer

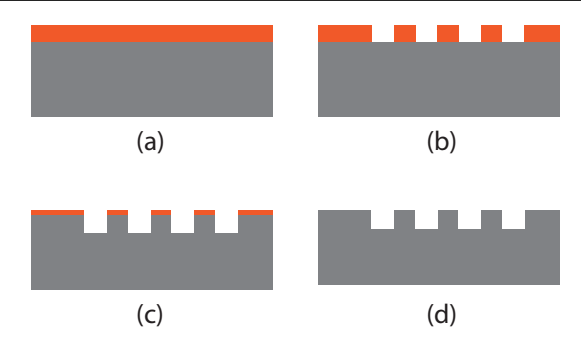


Figure 4.4: Schematic representation of the basic steps used for grating fabrication. (a) Spin coating of resist on the Si wafer, (b) Electron beam exposure and development, (c) Reactive ion etching and (d) Dry oxygen plasma etch.

is finally removed using dry oxygen plasma etch. The target parameters of the grating fabrication are period = 1300 nm, midCD = 560 nm, height = 115 nm and SWA = 90 degrees.

4.5 Experimental implementation

Figure 4.5, represents the schematics of the coherent Fourier scatterometer. Light from a He-Ne laser ($\lambda = 633$ nm), is coupled into a fiber which is then divided into two arms by a fiber coupler (FC). SMF1 and SMF2 are the illumination and the alignment arm, respectively. Light from SMF1 is collimated and polarized to provide a well-defined illumination of the sample through the microscope objective (MO). The incident light is selected to be either in TE or TM polarization configuration in the entrance pupil of the lens. The denomination TE (TM) here refers to the incident electric (magnetic) field in the entrance pupil being oriented parallel to the grooves of the grating. The incident focused spot can be decomposed into plane waves with varying incident angles. The maximum angle of incidence is limited by the numerical aperture NA of the microscope objective MO. In the actual experiment, we used an objective with NA = 0.4. The maximum angle of incidence is then $\approx 26^{\circ}$. Each allowed incident angle contributes to the reflected diffraction order(s) which propagate back through the MO to the CCD. The diameter of the collimated reflected beam is reduced by a telescopic system, which images the back focal plane (BFP) of the MO onto the CCD with a de-magnification of 2.5X to fit into the CCD area (1600×1200 pixels, size of $3.75 \ \mu m \times 3.75 \ \mu m$ per pixel). In the Fourier or back focal plane (BFP) there is an interference between the overlapping reflected orders for the chosen F number (1 < F < 2, see Fig. 4.3). The polarizer P2 in the experimental setup can be used to detect a selected polarization at the CCD. SMF2 is used to align the telescopic system. The red LED light source is only used to image the grating on the CCD camera for alignment purposes during the preparation of the experiment. Components BS2 and L6 are removed during data acquisition. The solid red line in the

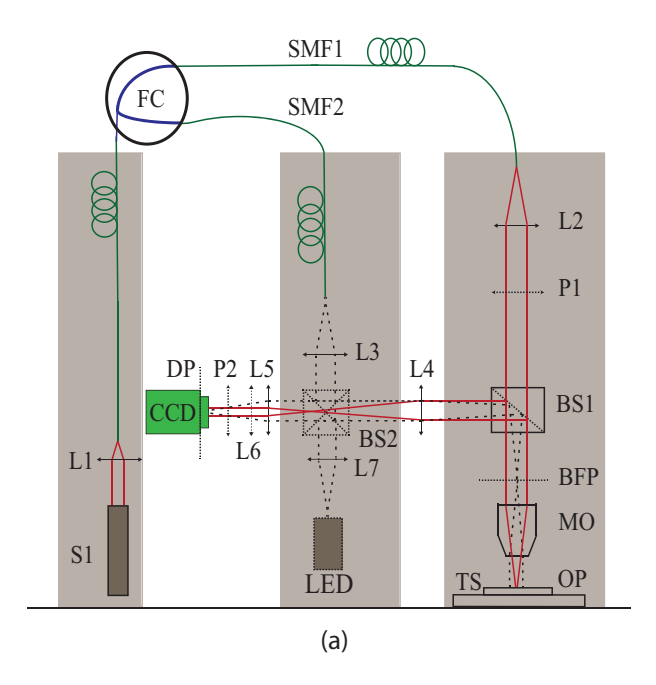


Figure 4.5: Schematics of the experimental setup. S1: He-Ne laser, FC: Fiber splitter, SMF: Single mode fiber, LED: Light emitting diode, BS: Beam splitter, P: Polarizer, L: lens, DP: Detector plane, BFP: Back focal plane, OP: Object plane (grating), MO: Microscope objective, TS: Piezo-controlled translation stage.

ray diagram of Fig. 4.5 is the data acquisition path and the black dotted paths are used only for alignment and imaging. Figure 4.6 is an artistic impression of the laboratory setup.

The quality of far field intensity is subjected to errors namely:

- Tip tilt error of the translation stage
- Focus error
- Scanning system error
- Sample fabrication error

The tip tilt error alters the effective period of the grating and also causes the interaction of the grating with a different field distribution compared to the expected focus spot on the sample. The sample holder stage is aligned to prevent tip tilt error with the help of a piezo controlled system. The collimation is then evaluated with a shear interferometer (or a by SHS wavefront sensor) for the collimated beam in the return path to detector, when the focus is at the sample surface. Figure 4.7, shows the simultaneous imaging of the grating and the focused spot. The focus error can also be addressed by confocal imaging of the grating and the focused spot. Confocal imaging of the focused spot and the grating surface assures the

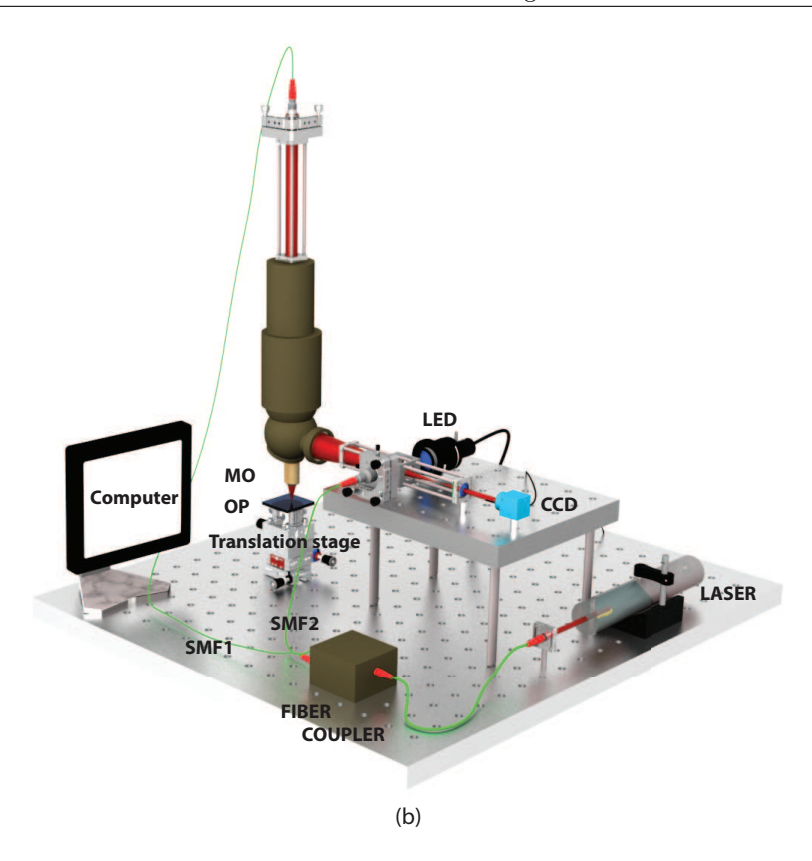


Figure 4.6: 3D illustration of the laboratory setup.

plane of the wafer and the focal plane coincide. A piezo controlled translation stage is used to scan the grating. The grating is scanned over the focused spot as shown in the Fig. 4.7 and the far field is recorded at the CCD. To check that, till what extent the far fields are same when scanned over a period of the grating in the experiment, Fig 4.8 shows the far field for fixed illumination conditions and defined grating parameters for scan positions difference of Λ . In principle the two far fields shown in Fig. 4.8a and Fig. 4.8b should be identical. The difference is shown in Fig. 4.8c.

4.6 From grating to CCD camera in the experimental setup

In the experimental setup, the detection plane is defined by the CCD camera, which captures the far field. The relation between the coordinates in the object plane, Fourier plane and the detection plane is derived and the effect of the telescopic system in the experimental setup is described.

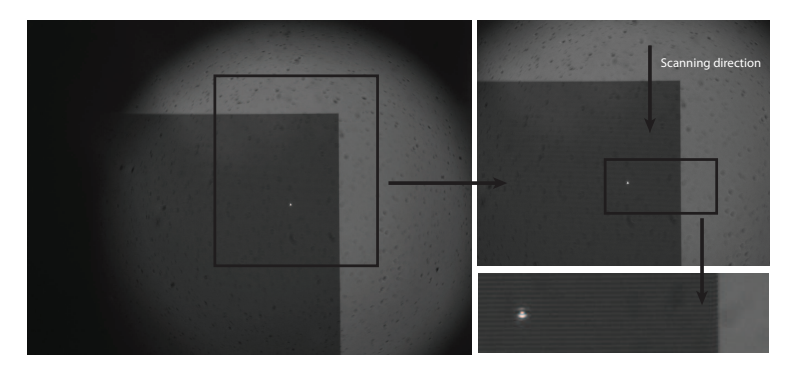


Figure 4.7: Focused spot imaged on the grating surface. Right hand side of the figure is zoomed at the focus spot on the grating.

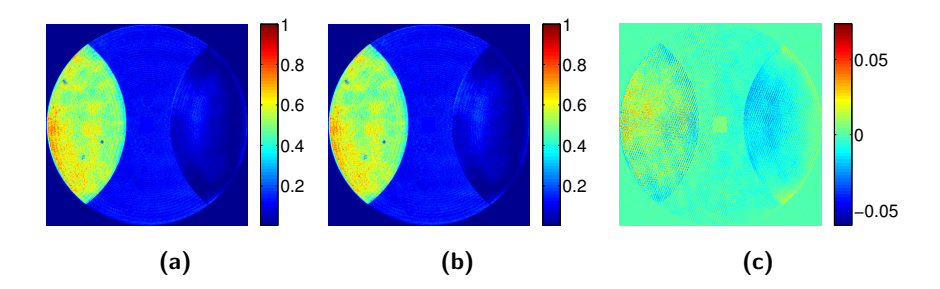


Figure 4.8: Far field intensity maps for scan positions separated by Λ of the grating for a grating of period of 1.3 $\mu \rm m$, midCD = 562 nm, height = 116 nm and SWA = 90 degrees for planar illumination with $\lambda = 633$ nm and NA = 0.4. The incident light is TE polarized in the entrance pupil and the scattered field is detected without the polarizing filter. (a) Far field intensity at zero bias (b) Far field intensity at bias = Λ (c) Far field intensity difference for bias 0 and Λ .

4.6.1 From CCD parameters to sample space: Through scaling in Fourier domain

Let us consider the coordinate system as defined in Fig. 4.9. Let the object plane, Fourier plane and the detection plane be represented by the parallel co-ordinate system (ξ, η) , (f_x, f_y) and (x, y), respectively. Let $\Delta \xi$ and $\Delta \eta$ be the pixel width in the CCD along the ξ and η axis (see Fig. 4.9). let the total number of pixels along ξ and η be N_{ξ} and N_{η} , respectively, with $\Delta \xi = \Delta \eta$. The CCD specifications in the experimental setup are: $N_{\xi} = 1600$, $N_{\eta} = 1200$, $\Delta \xi = \Delta \eta = 3.75~\mu\text{m}$. Hence the total physical detection area, which registers the scattered far field intensity data is given by: $-\xi_{max} \leq \xi \leq \xi_{max}$, $-\eta_{max} \leq \eta \leq \eta_{max}$,

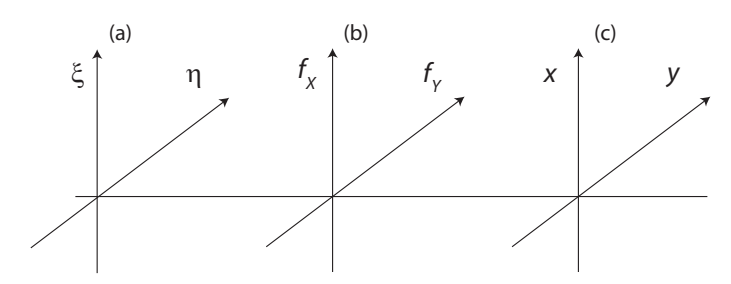


Figure 4.9: (a) CCD or Image plane (ξ, η) , (b) Fourier plane (f_x, f_y) and (c) Object plane (x, y).

where,

$$\xi_{max} = \frac{\Delta \xi \left(N_{\xi} - 1 \right)}{2},
\eta_{max} = \frac{\Delta \eta \left(N_{\eta} - 1 \right)}{2}.$$
(4.3)

The physical space of the CCD corresponds to the Fourier domain of the experimental data. For a microscope objective with focal length f, the spatial frequency of the scattered plane wave (f_x, f_y) and the corresponding point (ξ, η) in the CCD plane are related by:

$$\begin{cases}
f_x = \frac{\xi}{\lambda f}, \\
f_y = \frac{\eta}{\lambda f},
\end{cases} (4.4)$$

The grid spacing in the Fourier space is thus given by:

$$\Delta f_x = \frac{\Delta \xi}{\lambda f},$$

$$\Delta f_y = \frac{\Delta \eta}{\lambda f},$$

$$\tag{4.5}$$

The total number of pixels in the Fourier domain is identical to that in the space domain i.e., $(N_{f_x} = N_{\xi})$ and $(N_{f_y} = N_{\eta})$.

Let E(x,y) and $E_{ff}(\xi,\eta,z)$ denote the field in the object plane and far field, respectively. The relationship holds for the field in the object plane and the CCD plane [59].

$$E_{ff}(\xi,\eta) = \left[\int \int E(x,y) \exp\left(-i2\pi x f_x - i2\pi y f_y\right) dx dy \right]_{f_x = \frac{\xi}{\lambda f}, f_y = \frac{\eta}{\lambda f}}$$
(4.6)

where, x and y are the spatial coordinates in the object plane. The near field is transformed into far field by using fast Fourier transform using the conditions,

$$\Delta f_x \Delta x N_{\xi} = 1, \Delta f_y \Delta y N_{\eta} = 1.$$
(4.7)

and, imposing the far field length constraint,

$$\sqrt{\left|f_x\right|^2 + \left|f_y\right|^2} \le \frac{NA}{\lambda} \tag{4.8}$$

subsequently,

$$\Delta x = \frac{\lambda f}{\Delta \xi N_{\xi}},$$

$$\Delta y = \frac{\lambda f}{\Delta \eta N_{\eta}}.$$
(4.9)

This implies that the pixel size in the sample plane is a function of the incident wavelength, focal length of the microscope objective and the physical space of the CCD. Hence, once the far field is measured on the CCD plane (ξ, η) , the Fourier domain (f_x, f_y) can be computed and finally the object space (x, y).

4.6.2 Role of the telescopic system

The radius of the exit pupil of the microscope objective is 4 mm, whereas the phyical size of the CCD is 6 mm \times 4.5 mm. The scattered collimated beam from the grating does not fit the CCD chip so that a telescopic system with a de-magnification factor of 2.5X is used. As shown in Fig. 4.5, L4 and L5 are the telescopic lenses. This implies that when going from the spatial frequencies (f_x, f_y) to the object plane (x, y), an additional scaling factor is required. Let the new scaled frequencies be denoted by \tilde{f}_x and \tilde{f}_y , such that $\tilde{f}_x = 2.5 f_x$ and $\tilde{f}_y = 2.5 f_y$. Then the final spectrum is given by,

$$A\left(\tilde{f}_{x},\tilde{f}_{y}\right) = \left[\int\int E\left(x,y\right)\exp\left(-i2\pi x\tilde{f}_{x} - i2\pi y\tilde{f}_{y}\right)dxdy\right]_{f_{x} = \frac{2.5\xi}{\lambda f},f_{y} = \frac{2.5\eta}{\lambda f}}.$$

$$(4.10)$$

The scaling of frequencies results in the scaling of the pixel size in the object plane,

$$\Delta x = \frac{\lambda f}{2.5 \Delta \xi N_{\xi}},$$

$$\Delta y = \frac{\lambda f}{2.5 \Delta \eta N_{\eta}}.$$
(4.11)

4.7 Results and Discussion

4.7.1 Diffracted far field intensity maps

Along with the acquisition of experimental data, scatterometry also requires an accurate modeling of the interaction between field and sample. We used the rigorous coupled wave analysis (RCWA) as rigorous solver to compute the field diffracted by the grating [19–21]. In order to make the simulations as accurate as possible, the measured amplitude and phase distribution of the incident field are included

in the RCWA simulations. The amplitude for the incoming beam is practically uniform (measured by SHS and CCD) but the phase in the entrance pupil is not and was measured with a Shack-Hartmann wavefront sensor (SHS) [25]. In Figs. 4.10(a) and (e) the measured wavefronts for TE and TM polarizations on the lens pupil expressed in units of wavelength of the incident light are shown without the polarizer in the reflected field. The far field intensity maps for a fixed bias shown in Fig. 4.10 are the simulated and measured data obtained for a silicon etched grating having overlap parameter F = 1.2 (see Fig. 4.3) for NA = 0.4 at the wavelength of 633 nm. Far field intensity maps b, c and d (f, g and h) represent respectively the simulation, experiment and the difference between them for best matched fit for TE (TM) incident light on the lens pupil and mixed output polarization (i.e., no polarizer is used in the detection path). In the simulations, the measured wavefront with a Shack-Hartmann sensor (SHS) is used to compute the diffracted far field intensity maps by multiplying the measured incident field on the entrance pupil with the reflected spectrum from the grating. This is valid assuming the aberration of the microscope objective to be negligible. The spectrum is computed when the incident light is of unity amplitude and constant phase on the entrance pupil of the lens. The camera has been tested for noise measurements, where each far field intensity map is averaged over 10 frames. Also, we consider the measured noise of the CCD camera as normally distributed with standard deviation given by measured uncertainties of $\sigma = 1 \times 10^{-3}$. While the energy in the diffracted order depends upon the grating parameters, the extent of overlap between the diffracted orders in the far field is given by the overlap parameter F. It is to be noted that the energy distribution in the far field intensity maps are different for TE and TM incident polarized light. In the overlap region there is interference between the diffracted orders. There is a phase change in the overlap region with the translation of the grating along x-axis in the sample plane, due to the change in phase of the non zero diffracted orders with translation of the grating. This causes the change in the interference region with change in bias value. The amount of phase shift $(\delta \phi)$ in the non-zero order with order number m, due to translation distance δx is given by,

$$\delta\phi = \frac{2\pi m \delta x}{\Lambda}.\tag{4.12}$$

4.7.2 Bias correlation

Wafer positioning is an important issue in the industrial manufacturing process. Being a phase sensitive technique, CFS introduces a change in the far fields with scanning position on the grating. In the experiments, far field intensity maps for consecutive scan positions (bias) of 20 nm difference were recorded over the length of several periods of the grating. The ability to distinguish between the intensity maps defines the sensitivity to bias of the present experimental setup. The degree of correlation 'r' (correlation coefficient) in Eqn. 4.13 is used as a measure to

distinguish experimental images:

$$r = \frac{\sum_{\xi} \sum_{\eta} \left(I_{\xi\eta}^{ref} - \bar{I}^{ref} \right) \left(I_{\xi\eta} - \bar{I} \right)}{\sqrt{\left(\sum_{\xi} \sum_{\eta} \left(I_{\xi\eta}^{ref} - \bar{I}^{ref} \right)^{2} \right) \left(\sum_{\xi} \sum_{\eta} \left(I_{\xi\eta} - \bar{I} \right)^{2} \right)}}$$
(4.13)

Here, $I_{\xi\eta}^{ref}$ and $I_{\xi\eta}$ are the far field intensities corresponding to the starting bias position called reference and the other scanning positions. $\bar{I}_{\xi\eta}^{ref}$ and $\bar{I}_{\xi\eta}$ are the corresponding mean values.

The correlation coefficient 'r' has values between -1 to 1. When the intensity maps are completely correlated r=1, while r=0 implies no correlation and there is complete anti correlation between the intensity maps for r=-1. In Fig. 4.11, value of the correlation coefficient derived from the experimental far field intensity maps is shown for bias values ranging from 0 to 3 μ m. Usually the period of the grating is known with very high accuracy. Here the period of the grating is 1.3 μ m. Figure 4.11a plots values of 'r' for a scanning range of 3 μ m, while Fig. 4.11b plots the correlation coefficients for scanning positions within one period of the grating. Figure 4.11c is the colorlabel adjusted plot of Fig. 4.11b to highlight the sensitivity of bias, otherwise not visible in full scale colorbar representation. In Fig. 4.11a the correlation pattern is repeated for bias value equal to the period of the grating as expected.

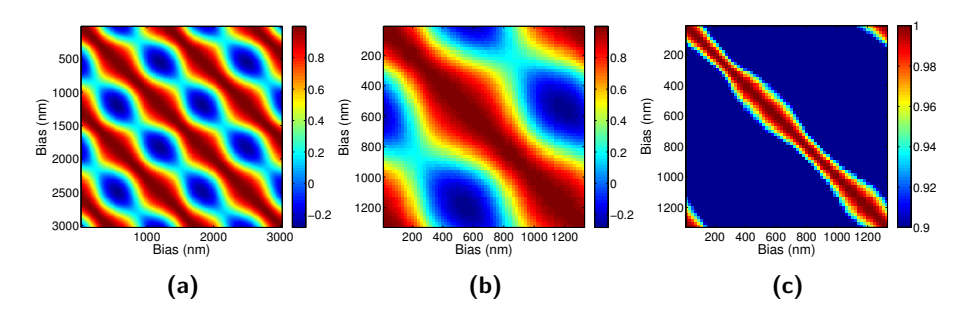


Figure 4.11: Degree of correlation between experimental far field intensity maps. (a) Correlation coefficients for positions separated by 20 nm for bias values ranging from 0 to 3 μ m (b) Correlation coefficients for positions separated by 20 nm for bias values within one period of the grating (c) same as b), but only showing the range points where 0.9 < r < 1.

From the above analysis of the experimental data, it is evident that CFS is highly sensitive to grating position. However for a symmetric grating, absolute position may also be determined regarding the symmetric position within a period of the grating (like the center of the midCD, corresponding to which far fields are also symmetric). In CFS, nm and sub-nm positioning within a single period of the grating can be reached in wafer alignment in semiconductor industry. It can also be used in other application as in imprint technology.

4.7.3 Model based optimization

Solving the inverse problem of grating reconstruction with CFS amounts to the determination of the values of the grating parameters for which the computed scattered far field maps fit best the experimentally measured images.

Figure 4.12 describes the model-based optimization flowchart for grating parameters reconstruction via non-linear gradient based optimization technique by solving non linear least squares problems. The physical model of the grating and the illumination scheme are defined. The incident wavefront is measured experimentally by a SHS sensor. The forward problem is solved by defining the nominal grating parameters to compute the simulated far field intensity maps, using the experimentally measured incident field. Based on the input and output polarization, the far field data is selected to be compared with the experimentally obtained far field intensity maps. For the real grating under test and the known experimental conditions, the experimental far field intensities data are registered. The intensity maps are then averaged over a range of few pixels to match the simulated data sets (we use 32×32 pixels over the lens pupil). Averaging of data is done to match the size of the simulated far field intensity maps. The merit function defined in Eqn. 4.14, compares the difference between the simulated and experimental far field intensity maps [36]. The merit function is minimized through solving linear least squares problems by updating the grating parameters in simulation. The grating parameters corresponding to the minimum value of the merit function gives the final estimated parameters of the grating.

The grating parameters defined in Fig. 4.1 lie in certain intervals obtained from a priori information and from the design specification. The parameters value of the design are called nominal values. Starting from the nominal values, the deviation between the experimental and simulated images are minimized, using a least square function (merit function) by varying the grating parameters. The diffracted far field of the grating depends on the known experimental conditions and the unknown grating parameters. Let \mathbf{a} be a vector consisting of the grating parameters and the bias and $I_{i,j}^{(m)}$ and $I_{i,j}^{(s)}$ the measured and simulated far field intensities at the i^{th} CCD pixel and j^{th} scan position. The merit function to be minimized is the difference between the simulated and experimental far field intensities summed over all the incident angles in the entrance pupil and pixels over the detector. The merit function is thus given by

$$f(\mathbf{a}) = \sum_{pol} \sum_{i=1}^{S} \frac{1}{N} \sum_{i=1}^{N} \left[I_{i,j}^{(m)}(\mathbf{a}) - I_{i,j}^{(s)}(\mathbf{a}) \right]^{2}, \tag{4.14}$$

where S is the total number of scan positions and N is the total number of pixels at the detector for a single far field intensity map.

The merit function can be minimized using library search or real time optimization methods [60]. In library search, several sets of far fields for approximate grating parameters lying in the defined intervals are computed. Subsequently, the set of grating parameters for the minimal value of the merit function (Eqn. 4.14) is selected as the desired value of the grating parameters. It is to be noted that the

optimization algorithm finds only the local minima. Here we use a gradient based non-linear least squares optimization method implemented in MATLAB as the function called "lsqnonlin". As a priori information in optimization, the target parameters of grating fabrication are used. Figure 4.13 shows a set of simulated and experimental far fields for bias values lying within a single period of the grating obtained with TE incident light on the lens pupil and no polarizer at the detector for the grating parameters corresponding to the minimized merit function. The noise in the experimental system is computed to be $\sigma = 1 \times 10^{-3}$. Consecutive far fields (numbered 1 to 12) correspond to consecutive grating positions for a bias difference of 100 nm.

4.7.4 Parameters reconstruction and discussion

The reconstructed grating parameters are listed in Table 4.1 (all the grating parameters including bias are fitted together in the optimization). The far field intensities used for the reconstruction algorithm is a set of data such as shown in Fig. 4.13 for TE polarized incident fields. A similar set of data from TM polarized incident field was also used. There was no polarizing filter at the detector side. To verify the results, the grating was also measured by SEM and AFM. The SEM measurement was performed with a Hitachi S 400 scanning electron microscope at 4 kV with a magnification of 35000. The uncertainties of the CFS and SEM were determined from repeated evaluations. In the case of the SEM, the uncertainty of the measured midCD was determined from measurements at different parts of the image (so the uncertainties are partly caused by line edge roughness). The bright edges of the grating lines were the main cause of the uncertainties. This edge is clearly seen in Fig. 4.14(a). The uncertainty of the height measurement with the AFM can be estimated using the histogram of Fig. 4.14(c). The uncertainties are in the "few nanometers" range for all techniques. A low-uncertainty measurement with AFM (without the 3D option) and SEM (without cutting the sample and measure the grating sidewall angles) is only possible for height and CD, respectively. The 3σ uncertainty in the grating parameters reconstruction by using CFS is lower compared to that obtained through SEM and AFM measurements. We furthermore notice higher relative uncertainties in SWA reconstruction as compared to height and midCD uncertainties, which are also reported by others [13]. The results are compiled in Table 4.1 for NA = 0.4 and at $\lambda = 633$ nm. Interestingly, the lateral position of the grating can be retrieved with an accuracy at ± 1 nm level, which is an impressive accuracy, considered the numerical aperture of the system and the wavelength used. Actually, an accurate retrieval of the alignment parameter bias is a fundamental pre-requisite for CFS to work. We have also performed simulations studies, in order investigate to which level of accuracy the alignment can be obtained through CFS measurements. We have found that, by using an incident field with $\lambda = 250$ nm, NA = 0.95 and a grating with pitch 200 nm positioning accuracy at 10 pico-meter level is attainable. Simulation studies show that at such high NA and shorter wavelength, the uncertainty in reconstruction of the grating parameters can be further decreased as well. All these benefits

Table 4.1: Comparative measurements of the grating parameters using different techniques.

Parameters	CFS	SEM	AFM
MidCD (nm)	563±2	562±4	_
Height (nm)	116±1	_	116±3
SWA(°)	89±3	_	_
Bias (nm)	1190±1	_	_

can be attributed to the phase sensitive signal, because for F<2 CFS can be seen as a common path interferometer.

4.8 Conclusions

Grating reconstruction with coherent Fourier scatterometry (CFS) has been demonstrated. The setup is capable of illuminating and measuring the response of the sample simultaneously over a broad range of incident and reflected angles and for two orthogonal incident polarizations. The measurement for all radial and azimuthal angles can be performed within one second. Due to the coherent illumination, the measuring spot can be focused to a size smaller than one micron. Compared to incoherent scatterometry the advantage of coherent Fourier scatterometry is that the measured response in the pupil plane includes interference patterns caused by overlapping orders. The interference changes when the spot is scanned perpendicularly to the grooves of the grating, and consequently the phase information contained in the overlapping orders can be determined accurately. The capabilities of the tool were demonstrated by reconstructing the parameters of grating with 1300 nm pitch using a wavelength of $\lambda = 633$ nm and an objective lens of NA = 0.4. The reconstruction was performed by non-linear least squares gradient fit of the grating parameters to minimize the difference between the measured and rigorously computed pupil images. The sensitivity of coherent Fourier scatterometry was found to be comparable with the applied reference metrology techniques (SEM and AFM). Simulation studies shows that positioning accuracy of the order of 10 picometer with NA = 0.95 and λ in the UV can be achieved. Also, accurate nano-positioning in combination with the reconstruction shape parameters of the grating can be done in a single tool which is not possible in conventional optical scatterometry.

4.8. Conclusions 67

Figure 4.10: Simulated and experimental far field intensity maps for a fixed bias value and the difference between the simulation and experiments. Wavefront for TE (a) and TM (e) incident polarizations on the lens pupil. Far field intensity maps b, c and d (f, g and h) represent the simulation, experiment and the difference between them for best matched fit for TE (TM) incident light on the lens pupil and mixed output polarization. The diameter of the entrance pupil is $8\,$ mm.

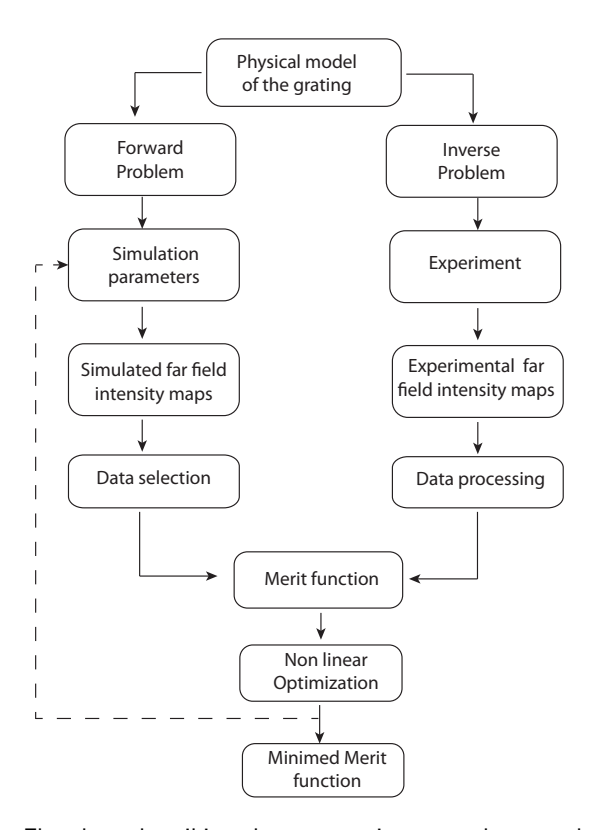


Figure 4.12: Flowchart describing the systematic approach to model based optimization for grating reconstruction.

4.8. Conclusions 69

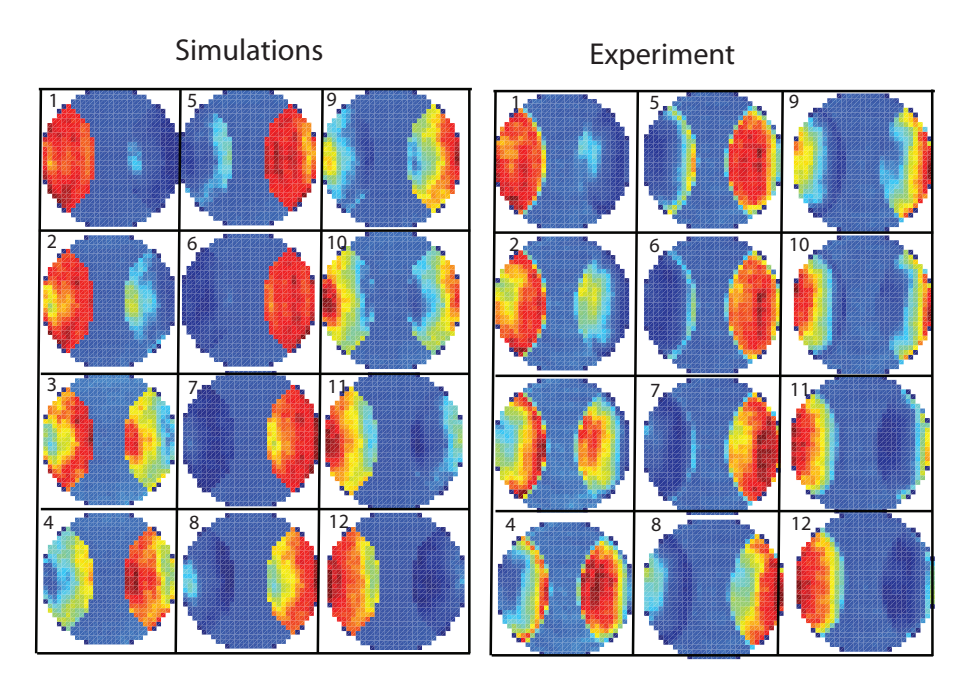


Figure 4.13: Simulated and experimental far field for TE incident polarization on the lens pupil and no polarizer at the detector for the grating parameters corresponding to the minimized merit function. The bias position is changed by 100 nm between consecutive far fields (numbered 1 to 12). Incident wavelength is 633 nm with NA= 0.4 and the period of the grating is 1.3 μ m.

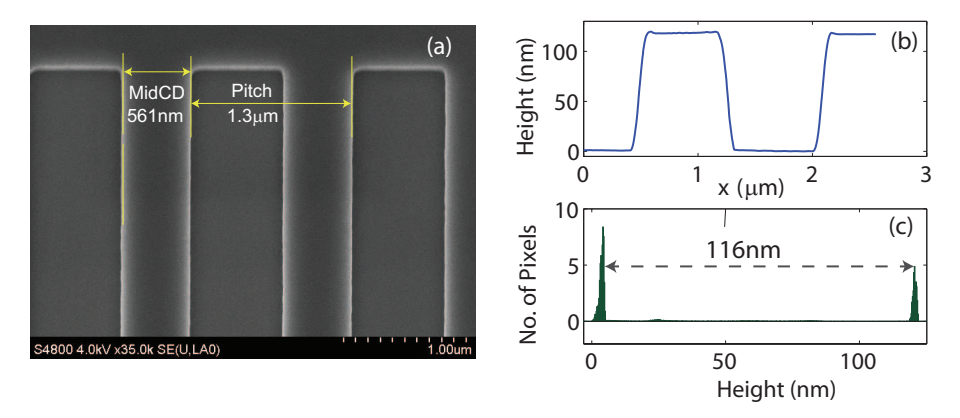


Figure 4.14: (a) Top view of the SEM image. (b) AFM cross section in the direction perpendicular to the grating lines. (c) Histogram of heights for each pixel of the AFM measurement.

Chapter



Diffraction based overlay analysis in coherent Fourier scatterometry

5.1 Abstract

Structures on the wafer for integrated circuit are built by lithographic process. Any pattern on the wafer is written layer by layer to realize the final structure. The positional accuracy of new patterns on the existing ones decides the performance of the circuitry. Deviation of the consecutive layer is called overlay. To determine the overlay signal, several targets on the wafer are measured by IOS. In the present work, we use CFS to improve the overlay signal. Mathematical analysis and simulations show increased sensitivity of CFS to an overlay, with possibility of decreasing the overlay target size.

5.2. Introduction 73

5.2 Introduction

In photo-lithography, the absolute coordinate grid is defined for the lithographic pattern to be printed on the wafer. This is called registration. Positional accuracy of features on a photo-mask to be printed on the wafer is governed by the registration process. The intended features on the wafer for an integrated circuit is then written by a sequence of patterning steps (layer by layer in succession). Overlay is a measure of the positional accuracy between the new lithographic layers printed on the existing pattern (pre-printed) at every point on the wafer. With the continuous decrease in size of the features on the wafer, the measurement of overlay is critical for the lithographic quality and yield.

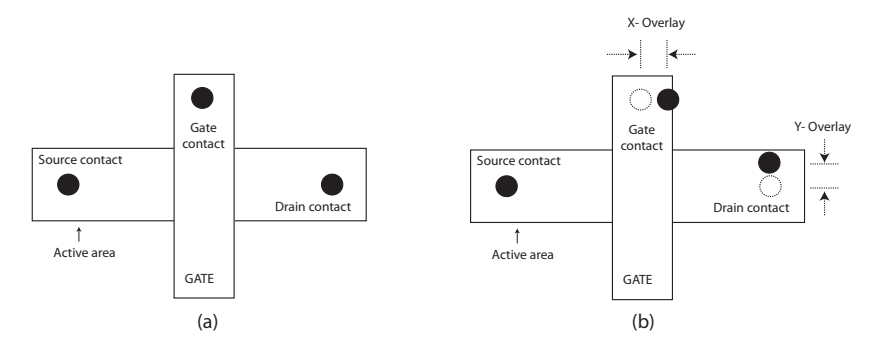


Figure 5.1: The contacted transistor (a) No overlay errors (b) Overlay errors.

Figure 5.1 shows a transistor as an end product of a photo-lithography process. Figure 5.1 (a) and (b) shows a contacted transistor without and with overlay errors¹. Overlay has direct consequences on the performance of the transistors. For example, the electrical problems due to overlay errors can be categorically stated: when the gate contact is shifted towards the active area, leakage current rises leading to a rise in power consumption or even failure of the circuit. Also, due to overlay, the change in amount of overlap between the contact hole and the underlying conductor layer can cause either increase or decrease in resistance or even short-circuit. Minimizing overlay errors can lead to enhancement in design and performance of the integrated circuit.

In order to measure and control the overlay, specific targets are printed on the wafer simultaneously with the actual desired features on the wafer. These specific targets are box in box structure, a part of the structure is printed with one layer and the other part of the structure is printed in the subsequent layer patterning. The printed patterns are then imaged layer by layer to deduce overlay for the patterning process. This is the principle of imaging-based overlay [62]. For overlay analysis, several alignment systems, overlay models and process-dependent overlay effects have been analyzed and studied in detail [61,63].

Another approach for an overlay analysis is a diffraction-based [64–66]. For a grat-

 $^{^{1}}$ Figure adapted from [61] (pg199-200)

ing stack structure (two gratings on top of each other separated by an intermediate layer), the overlay between the two gratings leads to an asymmetry in the $+1^{st}$ and -1^{st} diffracted orders from the grating stack. The asymmetry is the measure of an overlay between the gratings, while the direction of the overlay is determined by using two known shifts between the gratings in the stack.

In this chapter, we present diffraction based overlay (DBO) analysis for coherent Fourier scatterometry and compare the result with an existing model of overlay analysis in incoherent scatterometry. The model of the grating structure is presented, the mathematical basis for the analysis is derived and finally simulation results are discussed.

5.3 Model of the grating stacks

The geometry of the grating stack is shown in Fig. 5.2. Grating 1 and 2 are the top and bottom grating, respectively in the stacks separated by an intermediate layer (Medium 2). Medium 1 and Medium 3 are the upper and lower half spaces.

Identical periodicity of the grating imposes coupling between the gratings through the diffracted orders, given by the grating equation. Let us consider grating 1 and grating 2 as one dimensional infinite gratings with period Λ , with the direction of periodicity defined as the x axis as in Fig. 5.2. The response of the individual gratings to the incident field is given by complex reflection and transmission matrices \hat{r} and \hat{t} for every incident plane wave. Furthermore, the top grating in the

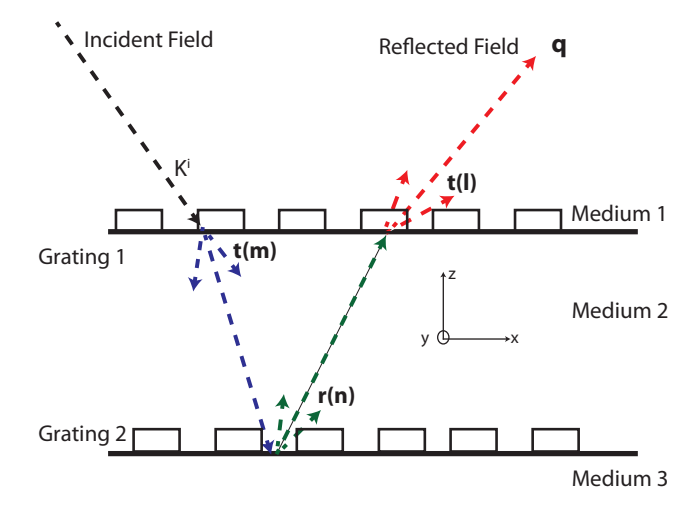


Figure 5.2: Geometry of grating stacks. Grating 1 and 2 are the top and bottom grating, respectively in the stacks separated by an intermediate layer (Medium 2). Medium 1 and Medium 3 are the upper and lower half spaces. t(m) and t(l) are the transmission matrices related to the top grating and r(n) is the reflection matrix related to the bottom grating, corresponding to the incident and scattered wave from the gratings.

stack acts in transmission and $\hat{t}(m)$ is the transmission matrix characterizing the m^{th} order transmission of grating 1 for light incident from medium 1 to medium 2 and medium 2 to medium 1, respectively. Furthermore, $\hat{r}(n)$ is the reflection matrix for the n^{th} order reflection from the bottom grating. The incident and the scattered fields are analyzed in medium 1. Although, light can be incident at any arbitrary angle on the grating, we analyze the case of planar diffraction for simplicity. The interaction between the incident field and the grating stack involves:

- 1. Scattering at interfaces, characterized by
 - (a) Transmission matrix
 - (b) Reflection matrix
- 2. The scattered waves as
 - (a) Propagating waves
 - (b) Evanescent waves

For simplicity, the propagation effect of the diffraction orders inside the intermediate layer is not considered. Hence, effectively, the two gratings are considered as separate. Also, the evanescent coupling is ignored.

5.4 Asymmetry signal in incoherent optical scatterometry

In the grating stack defined in Fig. 5.2, the period Λ of the gratings are such that there exists the first diffracted orders ± 1 , for an illumination wavelength λ and the numerical aperture (NA) i.e., 1 < F < 2 (F is defined in Eqn. 4.2 in Chapter 4). For different incident angles on the grating stack, the output direction of the diffracted orders may coincide. In incoherent optical scatterometry, the contribution of all different incident angles contributing to the identical diffracted direction is obtained by adding the diffracted field intensities. Instead, in coherent scatterometry, the electric fields of individual contributions are summed up and then their modulus gives the total intensity in that output direction. The mathematical basis for the diffraction based overlay analysis is presented in the next section.

5.4.1 Complex amplitude from grating stacks: Mathematical foundation

For a planar incident wave on the grating stack, the scattered wave is analyzed in the direction of the diffraction vector \mathbf{q} . Let the incident field on the gratings stack be given by:

$$E(x) = \exp(ik_x^i x),\tag{5.1}$$

where k_x^i is the x-component of the incident wave-vector on grating 1. The field transmitted by the grating is given by:

$$U_1(x) = t_{k_x^i}(x) \times \exp(ik_x^i x), \tag{5.2}$$

The transmitted field $U_1(x)$ from grating 1 propagates to grating 2 in the stack and is then partially reflected. Neglecting the phase factor due to propagation, the field $U_2(x)$ reflected by grating 2 is:

$$U_2(x) = t_{k_x^i}(x) \times r_{k_x^i}(x) \times \exp(ik_x^i x),$$
(5.3)

This field $(U_2(x))$ is partially transmitted by grating 1 into medium 1, resulting in field distribution $U_3(x)$:

$$U_3(x) = [t_{k_x^i}(x)]^2 \times r_{k_x^i}(x) \times \exp(ik_x^i x), \tag{5.4}$$

The functions $t_{k_x^i}(x)$ and $r_{k_x^i}(x)$ are Λ periodic and thus can be expressed as:

$$t_{k_x^i}(x) = \sum_{m} \hat{t}_{k_x^i}(m) \exp\left(\frac{i2\pi mx}{\Lambda}\right),$$

$$r_{k_x^i}(x) = \sum_{n} \hat{r}_{k_x^i}(n) \exp\left(\frac{i2\pi nx}{\Lambda}\right),$$

$$(5.5)$$

where,

$$\hat{t}_{k_x^i}(m) = \frac{1}{\Lambda} \int_0^{\Lambda} t_{k_x^i}(x) \left(\frac{-i2\pi mx}{\Lambda}\right) dx,
\hat{r}_{k_x^i}(n) = \frac{1}{\Lambda} \int_0^{\Lambda} r_{k_x^i}(x) \left(\frac{-i2\pi nx}{\Lambda}\right) dx.$$
(5.6)

Now, if the bottom grating (grating 2) in the stack is shifted by an amount $\Delta \xi$ in the x-direction, then the field $U_3(x)$ above the stack becomes:

$$U_{3,k_x^i,\Delta\xi}(x) = \left[t_{k_x^i}(x)\right]^2 \times r_{k_x^i,\Delta\xi}(x) \times \exp(ik_x^i x). \tag{5.7}$$

where,

$$r_{k_x^i,\Delta\xi}(x) = r_{k_x^i}(x - \Delta\xi), \tag{5.8}$$

and we have,

$$\widehat{r_{k_x^i,\Delta\xi}}(n) = \widehat{r_{k_x^i}}(n) \exp\frac{-i2\pi n\Delta\xi}{\Lambda}.$$
(5.9)

In the sequel, we will omit the subscript '3' and write $U_{3,k_x^i,\Delta\xi}(x)$ as $U_{k_x^i,\Delta\xi}$. Hence the complex amplitude of the q^{th} diffraction order is,

$$\widehat{U_{k_x^i,\Delta\xi}}(q) = \widehat{\left[t_{k_x^i}\right]^2} \widehat{r_{k_x^i,\Delta\xi}}(q)$$

$$= \sum_{n} \widehat{\left[t_{k_x^i}\right]^2} (q-n) \widehat{r_{k_x^i,\Delta\xi}}(n)$$

$$= \sum_{n} \widehat{\left[t_{k_x^i}\right]^2} (q-n) \widehat{r_{k_x^i}}(n) \exp \frac{-i2\pi n \Delta\xi}{\Lambda}.$$
(5.10)

5.4.2 Symmetry-based relations

According to the model, top and bottom gratings of the stack are individually symmetric gratings. Thus,

$$\hat{r}_{-k_x^i,\Delta\xi}(m) = \frac{1}{\Lambda} \int_0^{\Lambda} r_{-k_x^i}(x - \Delta\xi) \exp\left(\frac{-i2\pi mx}{\Lambda}\right) dx$$

$$= \frac{1}{\Lambda} \int_0^{\Lambda} r_{k_x^i}(\Delta\xi - x) \exp\left(\frac{-i2\pi mx}{\Lambda}\right) dx$$

$$= \frac{1}{\Lambda} \int_0^{\Lambda} r_{k_x^i}(\Delta\xi + x) \exp\left(\frac{i2\pi mx}{\Lambda}\right) dx$$

$$= \hat{r}_{k_x^i,-\Delta\xi}(-m). \tag{5.11}$$

5.4.3 Asymmetry signal

In addition to the incident wave with x-component of the wave vector given by k_x^i , we also consider an incident wave of which the x-component of the wave vector then is opposite and we consider then the $-q^{th}$ diffracted order, instead of the q^{th} diffracted order. The complex amplitude of this $-q^{th}$ diffracted order is:

$$\widehat{U_{-k_x^i,\Delta\xi}}(-q) = \left[t_{-k_x^i}\right]^2 r_{-k_x^i,\Delta\xi}(-q)$$

$$= \sum_n \widehat{\left[t_{-k_x^i}\right]^2} (-q-n) \widehat{r_{-k_x^i,\Delta\xi}}(n)$$

$$= \sum_n \widehat{\left[t_{k_x^i}\right]^2} (q+n) \widehat{r_{k_x^i,-\Delta\xi}}(-n)$$

$$= \sum_n \widehat{\left[t_{k_x^i}\right]^2} (q-n) \widehat{r_{k_x^i,-\Delta\xi}}(n)$$

$$= \left[t_{k_x^i}\right]^2 \widehat{r_{k_x^i,-\Delta\xi}}(q). \tag{5.12}$$

Furthermore, we can write,

$$\widehat{U_{-k_x^i,\Delta\xi}}(-q) = \widehat{[t_{k_x^i}]^2} \widehat{r_{k_x^i,-\Delta\xi}}(q)$$

$$= \sum_n \widehat{[t_{k_x^i}]^2} (q-n) \widehat{r_{k_x^i,-\Delta\xi}}(n)$$

$$= \sum_n \widehat{[t_{k_x^i}]^2} (q-n) \widehat{r_{k_x^i}}(n) \exp \frac{i2\pi n\Delta\xi}{\Lambda}.$$
(5.13)

The asymmetry signal used to quantify overlay in the incoherent case is the difference in intensities of Eqns. 5.10 and 5.13:

$$\Delta I_{incoh}(\Delta \xi) = \left| \widehat{\left[t_{k_x^i} \right]^2 r_{k_x^i, \Delta \xi}(q)} \right|^2 - \left| \widehat{\left[t_{-k_x^i} \right]^2 r_{-k_x^i, \Delta \xi}(-q)} \right|^2$$

$$= \left| \widehat{\left[t_{k_x^i} \right]^2 r_{k_x^i, \Delta \xi}(q)} \right|^2 - \left| \widehat{\left[t_{k_x^i} \right]^2 r_{k_x^i, -\Delta \xi}(q)} \right|^2$$

$$= \left| \sum_{n} \widehat{\left[t_{k_x^i} \right]^2}(q - n) \widehat{r}_{k_x^i}(n) \exp \frac{-i2\pi n \Delta \xi}{\Lambda} \right|^2$$

$$- \left| \sum_{n} \widehat{\left[t_{k_x^i} \right]^2}(q - n) \widehat{r}_{k_x^i}(n) \exp \frac{i2\pi n \Delta \xi}{\Lambda} \right|^2.$$
 (5.14)

Note that $\Delta I_{incoh}(\Delta \xi)$ is the asymmetry signal between the output direction q and -q, for incident wave-vector given by k_x^i and $-k_x^i$ respectively, when the gratings in the stack are displaced by $\Delta \xi$. If the gratings are not displaced then the total diffracted intensity in q and -q is identical. i.e.,

$$\Delta I_{incoh}(\Delta \xi) = 0, \text{ if } \Delta \xi = 0
\Delta I_{incoh}(\Delta \xi) \neq 0, \text{ if } \Delta \xi \neq 0$$
(5.15)

5.5 Asymmetry signal in coherent Fourier scatterometry

When an incident light wave interacts with the grating stack, several diffracted orders propagate in the directions given by the grating equation. In the event of multiple angle of incidence, the direction of the diffracted orders for few incidence angles may coincide owing to the period of the grating. In contrast to the incoherent case, where the intensity of the contributing orders in the diffraction direction is summed, in CFS, the total field in the diffraction direction is the sum over all the field contributions of the individual contributing orders in an identical direction.

5.5.1 Complex amplitude of diffracted orders for multiple coherent incident plane waves

Let there be two incident plane waves with x-component k_x^i and \tilde{k}_x^i , respectively. Suppose that the diffracted order q corresponding to the incident plane wave k_x^i

overlaps with the diffracted orders \tilde{q} of incident plane wave \tilde{k}_x^i , i.e,

$$k_x^i + 2\pi \frac{q}{\Lambda} = \tilde{k}_x^i + 2\pi \frac{\tilde{q}}{\Lambda}, \tag{5.16}$$

or,

$$\tilde{k}_x^i = k_x^i + \frac{2\pi}{\Lambda} \left(q - \tilde{q} \right). \tag{5.17}$$

Then the total complex amplitude in the direction specified by Eqn. 5.16 for relative shift $\Delta \xi$ of the two gratings is:

$$\hat{U}_{total}^{+}(\Delta \xi) \equiv \widehat{U_{k_{x}^{i},\Delta \xi}}(q) + \widehat{U_{\tilde{k}_{x}^{i},\Delta \xi}}(\tilde{q})$$

$$= \widehat{\left[t_{k_{x}^{i}}\right]^{2} r_{k_{x}^{i},\Delta \xi}}(q) + \left[t_{\tilde{k}_{x}^{i}}\right]^{2} r_{\tilde{k}_{x}^{i},\Delta \xi}(\tilde{q}).$$
(5.18)

The intensity is then given by:

$$I_{total}^{+}(\Delta \xi) \equiv \left| \hat{U}_{total}^{+}(\Delta \xi) \right|^{2}$$

$$= \left| \left[\widehat{t_{k_{x}^{i}}} \right]^{2} \widehat{r_{k_{x}^{i}, \Delta \xi}}(q) + \left[\widehat{t_{\tilde{k}_{x}^{i}}} \right]^{2} \widehat{r_{\tilde{k}_{x}^{i}, \Delta \xi}}(\tilde{q}) \right|^{2}. \tag{5.19}$$

Next, we consider incident plane waves of which the x-components of the wave vector are $-k_x^i$ and $-\tilde{k}_x^i$ and we consider the $-q^{th}$ and $-\tilde{q}^{th}$ diffracted orders, respectively. The total intensity in the diffraction direction specified by the wave vector whose x-component is $(-k_x^i-2\pi\frac{q}{\Lambda}=-\tilde{k}_x^i-2\pi\frac{\tilde{q}}{\Lambda})$, is given by:

$$I_{total}^{-}(\Delta\xi) = \left| \widehat{\left[t_{-k_x^i} \right]^2 r_{-k_x^i, \Delta\xi}(-q) + \left[t_{-\tilde{k}_x^i} \right]^2 r_{-\tilde{k}_x^i, \Delta\xi}(-\tilde{q})} \right|^2$$

$$= \left| \widehat{\left[t_{k_x^i} \right]^2 r_{k_x^i, -\Delta\xi}(q) + \left[t_{\tilde{k}_x^i} \right]^2 r_{\tilde{k}_x^i, -\Delta\xi}(\tilde{q})} \right|^2. \tag{5.20}$$

The asymmetry signal used to quantify overlay in the coherent case is the difference between Eqns. 5.19 and 5.20, i.e.,

$$\Delta I_{coh}(\Delta \xi) = I_{total}^{+}(\Delta \xi) - I_{total}^{-}(\Delta \xi)
= \left| \left[t_{k_{x}^{i}} \right]^{2} r_{k_{x}^{i}, \Delta \xi}(q) + \left[t_{\tilde{k}_{x}^{i}} \right]^{2} r_{\tilde{k}_{x}^{i}, \Delta \xi}(\tilde{q}) \right|^{2} - \left| \left[t_{k_{x}^{i}} \right]^{2} r_{k_{x}^{i}, -\Delta \xi}(q) + \left[t_{\tilde{k}_{x}^{i}} \right]^{2} r_{\tilde{k}_{x}^{i}, -\Delta \xi}(\tilde{q}) \right|^{2}
= \left| \left[t_{k_{x}^{i}} \right]^{2} r_{k_{x}^{i}, \Delta \xi}(q) \right|^{2} - \left| \left[t_{k_{x}^{i}} \right]^{2} r_{k_{x}^{i}, -\Delta \xi}(q) \right|^{2} + \left| \left[t_{\tilde{k}_{x}^{i}} \right]^{2} r_{\tilde{k}_{x}^{i}, \Delta \xi}(\tilde{q}) \right|^{2} - \left| \left[t_{\tilde{k}_{x}^{i}} \right]^{2} r_{\tilde{k}_{x}^{i}, -\Delta \xi}(\tilde{q}) \right|^{2}
+ 2 \Re \left[\left[t_{k_{x}^{i}} \right]^{2} r_{k_{x}^{i}, \Delta \xi}(q) \left[t_{\tilde{k}_{x}^{i}} \right]^{2} r_{\tilde{k}_{x}^{i}, \Delta \xi}(\tilde{q})^{*} \right] - 2 \Re \left[\left[t_{k_{x}^{i}} \right]^{2} r_{k_{x}^{i}, -\Delta \xi}(q) \left[t_{\tilde{k}_{x}^{i}} \right]^{2} r_{\tilde{k}_{x}^{i}, -\Delta \xi}(\tilde{q})^{*} \right]. \tag{5.21}$$

In case, when the two incident plane waves are mutually incoherent, then the difference signal that we use to quantify overlay becomes,

$$\Delta I_{incoh}(\Delta \xi) = \left| \widehat{\left[t_{k_x^i} \right]^2 r_{k_x^i, \Delta \xi}(q)} \right|^2 - \left| \widehat{\left[t_{k_x^i} \right]^2 r_{k_x^i, -\Delta \xi}(q)} \right|^2 + \left| \widehat{\left[t_{\tilde{k}_x^i} \right]^2 r_{\tilde{k}_x^i, \Delta \xi}(\tilde{q})} \right|^2 - \left| \widehat{\left[t_{\tilde{k}_x^i} \right]^2 r_{\tilde{k}_x^i, -\Delta \xi}(\tilde{q})} \right|^2.$$

$$(5.22)$$

Hence from the above,

$$\Delta I_{coh}(\Delta \xi) = \Delta I_{incoh}(\Delta \xi) + 2\Re \left(\widehat{\left[t_{k_x^i}\right]^2 r_{k_x^i, \Delta \xi}(q) \left[t_{\tilde{k}_x^i}\right]^2 r_{\tilde{k}_x^i, \Delta \xi}(\tilde{q})^* \right)} - 2\Re \left(\widehat{\left[t_{k_x^i}\right]^2 r_{k_x^i, -\Delta \xi}(q) \left[t_{\tilde{k}_x^i}\right]^2 r_{\tilde{k}_x^i, -\Delta \xi}(\tilde{q})^* \right)}.$$
 (5.23)

The incident field $(\exp(i\psi))$ can be chosen to maximize the interference term in Eqn. 5.23, giving the overlay signal dependent upon the incident field as,

$$\Delta I_{coh}(\Delta \xi) = \Delta I_{incoh}(\Delta \xi) + 2\Re \left\{ \exp \left(i\psi\right) \left(\widehat{\left[t_{k_x^i}\right]^2 r_{k_x^i, \Delta \xi}(q) \left[t_{\tilde{k}_x^i}\right]^2 r_{\tilde{k}_x^i, \Delta \xi}(\tilde{q})^* \right) \right\}$$

$$- 2\Re \left\{ \exp \left(i\psi\right) \left(\widehat{\left[t_{k_x^i}\right]^2 r_{k_x^i, -\Delta \xi}(q) \left[t_{\tilde{k}_x^i}\right]^2 r_{\tilde{k}_x^i, -\Delta \xi}(\tilde{q})^* \right) \right\}$$

$$(5.24)$$

5.5.2 Summary

We observe that the difference between the overlay signal in an incoherent and coherent Fourier scatterometry is the interference term. However, it should be highlighted here that the maximum sensitivity of the overlay signal in the coherent case can be reached by optimizing the phase difference between the incident waves such that the interference term in Eqn. 5.24 is maximum in the overlay signal. Hence, in case of different composition of structure for an overlay analysis, incident field engineering (entrance pupil engineering) can provide the best possible sensitivity for overlay measurement with CFS.

5.6. Simulations 81

5.6 Simulations

Figure 5.3 shows the geometry of the overlay stack used in RCWA simulations.

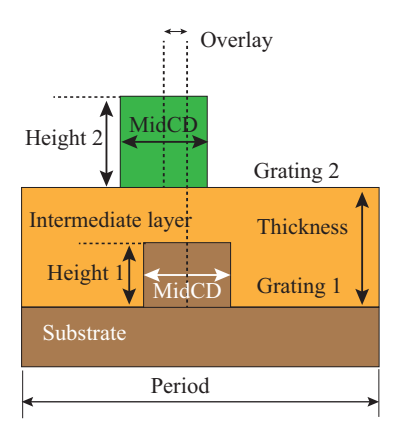
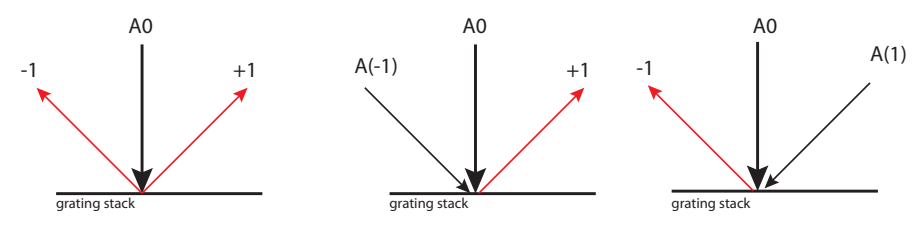


Figure 5.3: Geometry of grating stacks used for RCWA simulations. Grating 1 and 2 are the bottom and top grating respectively in the stacks separated by an intermediate layer. They are displaced by with respect to each other in the stack by the parameter mentioned overlay. Period and midCD of the two gratings in the stacks are identical.

The detailed specifications of the stack are:

- 1. Grating 1 (bottom grating in the stack).
 - (a) period $(\Lambda) = 500 \text{ nm}$
 - (b) height = 50 nm
 - (c) midCD = 250 nm
 - (d) material: resist
- 2. Grating 2 (top grating in the stack).
 - (a) period (Λ) = 500 nm
 - (b) height = 100 nm
 - (c) midCD = 250 nm
 - (d) material = silicon
- 3. Intermediate layer
 - (a) material = BARC
 - (b) thickness = 110 nm
- 4. substrate = silicon
- 5. wavelength = 405 nm



(a) Incoherent scatterometry scheme

(b) Coherent scatterometry scheme

Figure 5.4: Simulation scheme. (a) The incident wave is normal to surface of the grating stack and the asymmetry signal is the the difference between the intensities of +1 and -1 orders. (b) The individual incident waves are normal to the surface and at the angle of one of the orders, giving rise to diffracted orders in identical directions. The asymmetry signal is the difference between the intensities in the direction of +1 and -1 orders for normal incidence. The intensities are coherent superposition of the contributing fields.

Figure 5.4 shows the schemes of the simulations for asymmetry signal in an incoherent and coherent scatterometry setup. Figure 5.4(a), represents the case of incoherent scatterometry. Here an incident wave is normal to the surface of the grating stack giving rise to ± 1 orders. The asymmetry signal due to the overlay is the difference between the intensities of $+1^{st}$ and -1^{st} order. Figure 5.4(b), represents the case of coherent scatterometry. In the computation, two individual incident waves are used, which contributes in the same output direction. The individual incident waves are normal to the surface and at the angle of one of the orders, giving rise to diffracted orders in identical output direction. The asymmetry signal is then the difference between the intensities in the direction of +1 and -1 orders for normal incidence. The intensities are coherent superposition of the contributing fields. The simulations are done with RCWA at an incident wavelength of 405 nm.

5.6.1 Individual grating model

Here the individual gratings in the stack are not coupled to each other by the intermediate layer. Also, the phase change due to propagation of the orders between the gratings are neglected. The simulations are based on the mathematical analysis carried out in the chapter. Figure 5.5 shows the asymmetry signal for incoherent and coherent case. The displacement between the grating is denoted by $\Delta \xi$ and is shown on the horizontal axis and the asymmetry signal as difference in the intensity ΔI is shown on the vertical axis. It is evident from the Fig. 5.5 that the amplitude and slope of ΔI with $\Delta \xi$ for the coherent case is higher as compared to an incoherent case.

5.6. Simulations 83

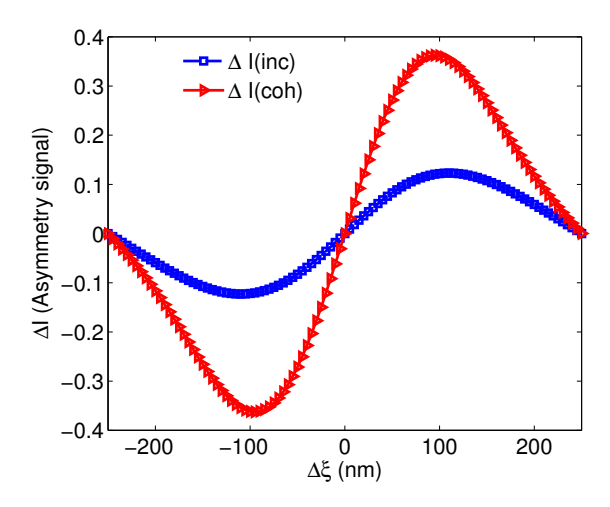


Figure 5.5: Overlay signal in optical scatterometry for incoherent (blue) and coherent (red) scatterometry for zero phase difference between the incident waves. ΔI is the asymmetry signal when the top and bottom grating in the stack are displaced by $\Delta \xi$. The period of the gratings is 500 nm each.

5.6.2 Rigorous simulations for real overlay target

In this section, simulation results are shown for Fig. 5.3, where the stack is rigorously solved and the overlay target in simulation is considered to be a single entity. In the semiconductor industry, for overlay metrology on grating stacks, typically larger wavelengths are used in order to benefit from the lower absorption (higher transparency) of the layer in between the two gratings of the grating stack. However, the use of a larger wavelength (red laser light) implies relatively large grating pitches in order to be able to detect 1st-orders of diffraction within the given NA of the lens. The overlay signal obtained in the incoherent and the coherent case is rigorously simulated by RCWA. Hence, the coupling between the gratings through the intermediate layers, the effects of the evanescent wave, and the phase change of the diffracted orders are considered in the computations. The rigorous simulation results in Fig. 5.6 also confirms the increase in asymmetry signal of coherent case compared to the incoherent analysis. The magnitude of the asymmetry signal in Fig. 5.6 is lower as compared to Fig. 5.5. This can be explained by the absorption by the intermediate layer in the stack.

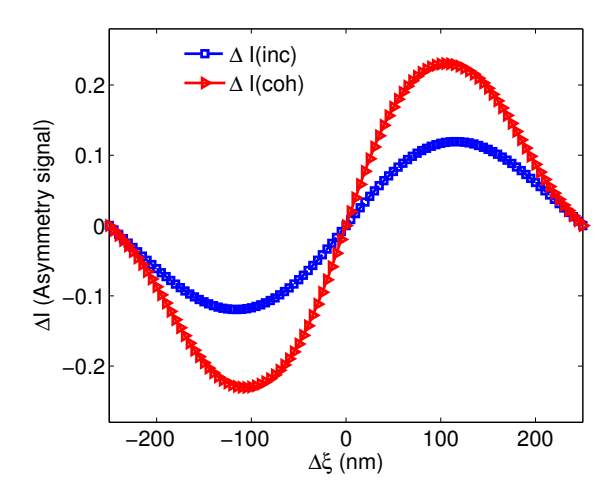


Figure 5.6: Rigorously simulated overlay signal in incoherent (blue) and coherent (red) scatterometry for zero phase difference between the incident waves. $\Delta \xi$ represents the shift in the bottom grating in the grating stacks. The period of the gratings are 500 nm each.

5.7 Conclusions

Mathematical analysis of overlay signal between two gratings in the stack for coherent and incoherent scatterometry shows that the sum of the product of the reflection and transmission coefficients plays an important role in deciding the magnitude of the asymmetry signal. Here we observe that the overlay signal in CFS is larger in magnitude than that of IOS. The direction of an overlay can be solved by carrying the same experiments in two different known overlay positions of the individual gratings in the grating stack, such that the asymmetry signal lies on the straight line part of the sinusoid. From simulations, we have shown that CFS is more sensitive to the overlay than compared to the incoherent case.

Application of μ -solid immersion lens in coherent Fourier scatterometry

6.1 Abstract

Optical resolution is limited by the incident wavelength and numerical aperture in a far field optical system. In semiconductor metrology, high resolution is required in order to resolve the diffracted orders from the grating. This can be achieved by decreasing the wavelength or increasing the numerical aperture of the system. Immersion lenses can be used for this purpose. In this chapter, we implement a micro solid immersion lens (SIL) to improve the resolution in a scanning near field microscope setup. It has been shown that micro-SIL can be used for metrology applications with high NA requirement. The idea and implementation of a Fourier scatterometer with a micro-SIL is also presented.¹

¹Most of the content in this chapter is based on the studies and results published in [67]

6.2. Introduction 87

6.2 Introduction

In an aberration-free optical system, the lateral spatial resolution is limited by the diffraction of light to $\approx \lambda_0/(2n_0\sin\theta_0)$. Here λ_0 is the incident wavelength in air, n_0 is the refractive index of the medium next to the investigated surface and θ_0 is the angular semi-aperture in the object space (the medium in which the lens is focusing), respectively. The numerical aperture (NA) of the system is defined by NA= $n_0\sin\theta_0$ and referred as the measure of the optical resolution, owing to the inverse proportionality to the lateral spatial resolution of the optical system. The refractive index in air is unity $(n_0 = 1)$, which limits the maximum NA= 1 and the optical resolution to $\approx \lambda/2$.

In principle, there are two parameters which have been used to improve the resolution: one is to increase the semi-aperture angle θ_0 and other the wavelength in the object space [50,53]. The maximum value of semi-aperture angle is $\theta_0 = 90^{\circ}$. Increasing θ_0 also increases the light collection efficiency of the optical system. The wavelength in the object space can be reduced by either using an incident light with low wavelength source or by increasing the refractive index in the focal region. For example, immersion systems use oil or water as a medium between the focusing lens and the focal spot increasing the spatial resolution by a factor equal to the refractive index (n_l) of the immersion, $(\approx \lambda/2n_l)$. However, immersion systems can contaminate the sample and in several applications is not suitable. An alternative to liquid immersion is the solid immersion lens (SIL). It is based on the principle of immersion lens since with the SIL, light beyond the critical angle is captured in the system. A SIL is a relatively simple optical component which is easy to use and integrate in the system to improve spatial resolution, light collection efficiency and magnification of the optical system. It was introduced by Mansfield and Kino in 1990 in the optical microscopy [68] and since then it has been used in several applications in nano-photonics [69–74]. The theoretical concept of SIL can be traced to the theory described by Born and Wolf in [50].

6.3 Solid immersion lens

"Light can be focused without aberrations at only two points within a high index sphere. These focal points are called aplanatic points of the sphere" [50]. The first focal point is the center of the high index sphere. This inspires the configuration of the hemisphere SIL (h-SIL) as shown in Fig. 6.1(a). An h-SIL increases the magnification of the system by factor n_{sil} . The second aplanatic point is located at a distance $z = R_{nsil}^{n_0}$ away from the center of the sphere as illustrated in Fig. 6.1(b). n_{sil} is the refractive index of the sphere, n_0 is that of the air and R is the radius of the sphere. SIL using this configuration is called super SIL (s-SIL) (Fig. 6.1(b)). Using s-SIL, magnification can be increased by a factor of n^2 . An s-SIL is more effective in increasing NA and magnification but as the focal point location depends on the refractive index of the sphere and the surrounding medium, it is wavelength sensitive. Hence, for different sets of incident wavelengths, there is no unique focal point. In contrast to s-SIL, an h-SIL works identical for all incident wavelengths, making it an attractive choice for multi wavelength incidence. For an

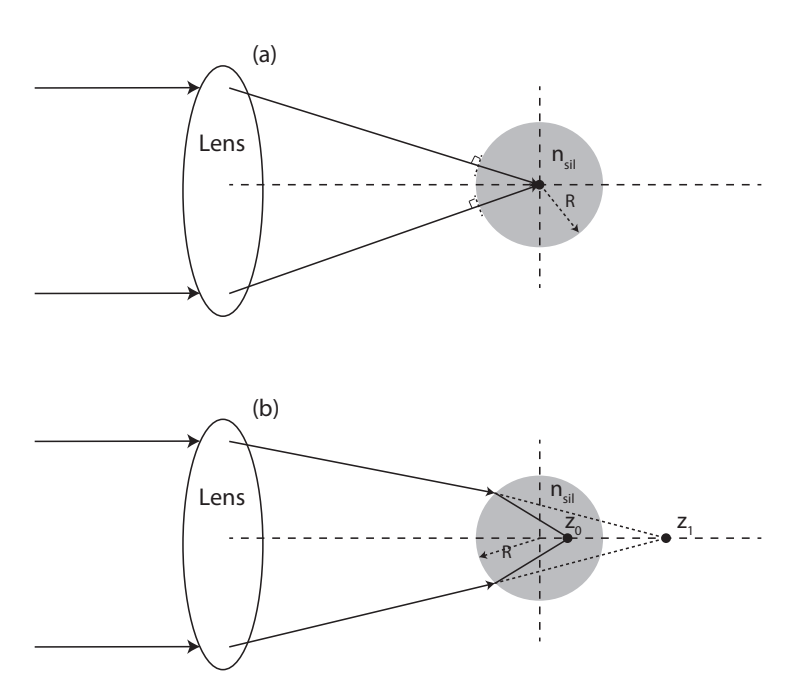


Figure 6.1: Aplanatic points in solid sphere. (a) h-SIL (b) S-SIL

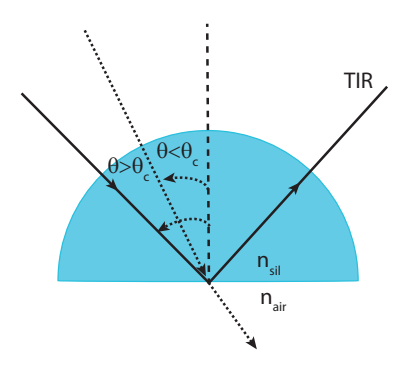


Figure 6.2: Schematics of the refraction and total internal reflection (TIR) at SIL bottom surface. θ_c is the critical angle beyond which all the light goes through total internal reflection.

h-SIL as shown in 6.2 it must be noted that, for incident angles greater than the critical angle in the SIL (θ_c) , there is no direct interaction of these incident angles to the surface beneath the SIL and the rays are reflected back by total internal reflection. The critical angle is proportional to the ratio of the SIL refractive index

to the medium (in our case, it is air), and is given as,

$$\theta_c = \sin^{-1} \left(\frac{n_{sil}}{n_{air}} \right) \tag{6.1}$$

The evanescent waves corresponding to these angles contributes to the interaction between light and object when the distance between the SIL and the surface beneath is a small fraction of incident wavelength [75]. The relative positioning of the SIL and sample is a major constraint in use of a SIL in practical applications as confocal scanning microscope and optical data storage. Beside that, for applications like optical metrology which we are interested, there is need of high speed movement of the SIL with respect to the wafer. This issue can be relaxed by using a micro-SIL (μ -SIL) [76–79]. Figure 6.3 shows the schematic of

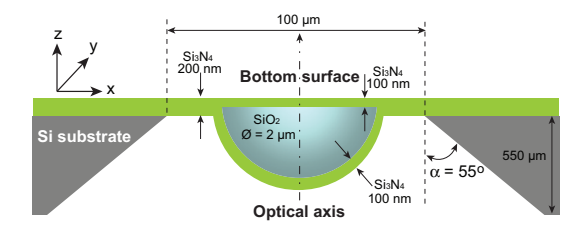


Figure 6.3: Schematics of the μ -SIL made of Si_3N_4 ($n_{Si_3N_4}=2$ at 405 nm). The μ -SIL has a diameter of 2 μ m. In the SIL used in our experiments, SiO_2 hemisphere is filled with Silicon Nitride.

the μ -SIL (2 μ m in diameter)². The μ -SIL was fabricated on a 200 mm Si wafer using standard microelectronic and micro-system tools. A hemispherical mould is formed by isotropic wet etching of Si through nano-metric hole, followed by the deposition of thin layer of 100 nm of silicon nitride (Si_3N_4) on the Si substrate. The thin layer of (Si_3N_4) forms the membrane, that holds the μ -SIL at the end of the molding process. The hemisphere mold is then filled with either (Si_3N_4) or (SiO_2), to form the body of the μ -SIL. A chemical-mechanical polishing process then planarize the structure. The spherical surface of the μ -SIL is then exposed to air by etching away the substrate form the back side. The μ -SIL are supported on a 100 μ m ×100 μ m membrane surrounded by a pillar like structure. Details of μ -SIL fabrication can be found in [80]. In this case, the lens is so light that it can be mounted in a cantilever typically used in atomic force microscopy (AFM) or scanning near field microscope.

In this chapter, we evaluate the performance of the μ -SIL by near field measurement of the focused spot and its applicability in CFS. In Section 6.3.1, we show direct near field measurements of the immersed spot in air achieved in a configuration where, 2 μ m (diameter) SIL made of Si_3N_4 ($n_{sil}=2$ at 405 nm), operates with a microscope objective of NA=0.6.

 $^{^2\}mathrm{We}$ acknowledge CEA LETI for providing the $\mu\text{-SIL}.$

6.3.1 Focal spot measurement of a μ -SIL

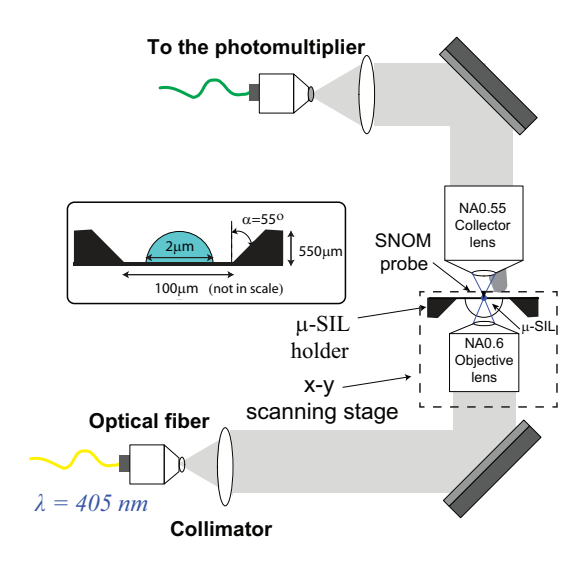


Figure 6.4: Schematics of the experimental setup used for near field measurement of the focused spot in absence and presence of μ -SIL respectively.

Figure 6.4 shows the schematics of the experimental setup for the near field measurement of the focused spot. Light from a diode laser ($\lambda = 405$ nm) is coupled into a single mode fiber and then to a scanning near field microscope (SNOM) (Witec Alpha 300 S). The μ -SIL is placed at the focal plane of the microscope objective of NA=0.6 as illustrated in Fig. 6.4. Figure 6.5 represents the immersion system and shows the simulated energy field distribution inside the μ -SIL. It is seen that the extent of energy distribution is limited to a small portion of the lens. This allows high incidence angle without loss of energy on the μ -SIL to obtain a higher numerical aperture of the optical system.

As shown in Fig. 6.4, the planar surface of the μ -SIL is probed by the SNOM tip (pyramidal structure of size ≈ 90 nm) and the signal is collected by the photomultiplier. The scanning window for the measurement is square area of $2 \times 2 \mu m^2$. The focus spot is measured in the plane at the bottom of the planar surface of μ -SIL for the microscope objective with NA=0.6 in the absence and the presence of the μ -SIL respectively. The incident collimated light of wavelength 405 nm, in the entrance pupil of the microscope objective with NA=0.6 is circularly polarized. The measured focused spot in the xy plane at z=0 is shown in Fig. 6.6. Figures. 6.6 (a) and (b) show the simulated focused spot at a distance of z=5 nm from the planar surface of the μ -SIL, in absence and presence of the immersion lens, while Figs. 6.6 (c) and (d) shows the measured focused spot in absence and presence of the the μ -SIL. The simulations are performed by rigorously solving Maxwell's equations for focused field in the near field of the μ -SIL. A detailed description of the simulation model is described in [81,82].

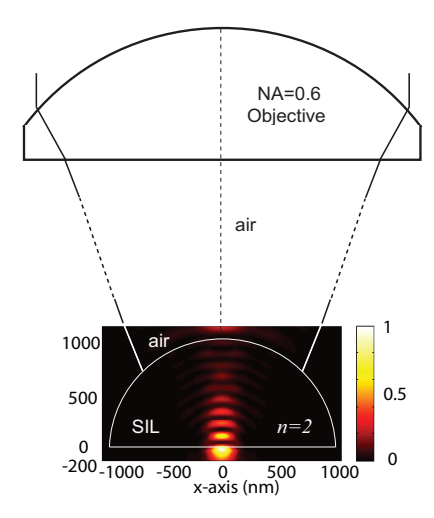


Figure 6.5: μ -SIL as an immersion system. The simulated electric field density is shown inside the immersion medium when the light is focused on the μ -SIL by a microscope objective of NA=0.6.

In Fig. 6.6, for the case when there is immersion, a significant reduction in focused spot size is obtained compared to that when there is no immersion present. A cross-section of the focused spot in xy plane along the x-axis at y=0 is presented in Fig. 6.7.

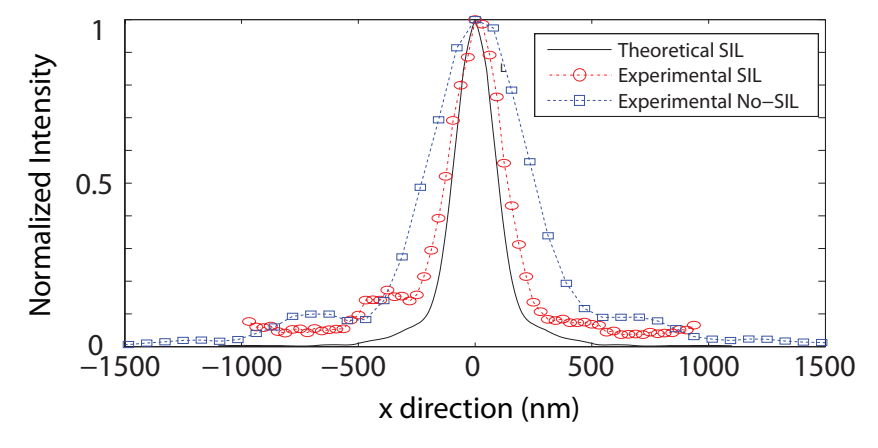


Figure 6.7: Intensity profiles along x axis at y=0 in the xy plane at z=5 nm for the simulated theoretical prediction of focus spot with μ -SIL and the measured experimental data in the absence and presence of the μ -SIL for a incident wavelength of 405 nm and light being circularly polarized in the entrance pupil of the microscope objective with NA=0.6.

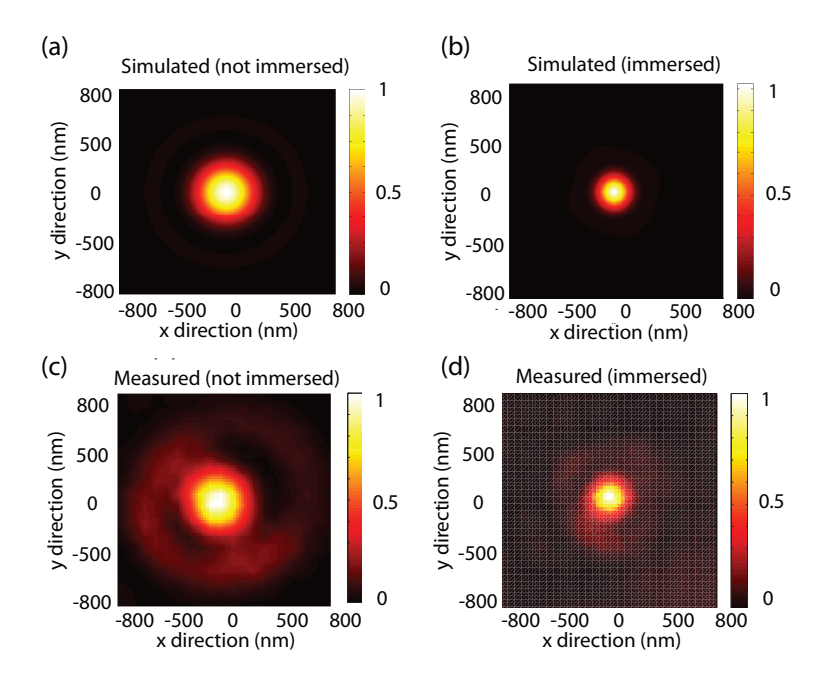


Figure 6.6: Focus spot in the focal plane at z=5 nm with NA=0.6. (a) Simulated focus spot without immersion, (b) Simulated focused spot with μ -SIL, (c) Experimental focus spot without immersion, (d) Experimental focused spot with μ -SIL.

In simulation, the full width at half maximum (FWHM) of the spot with immersion is ≈ 200 nm, where as the FWHM of the spot without the immersion is ≈ 360 nm. The reduction ratio is 1.8, slightly less than the refractive index of the μ -SIL. In experiment, the FWHM of the focused spot without the immersion is ≈ 450 nm, while with the immersion is ≈ 265 nm. The measured reduction in the spot is ≈ 1.7 times the focus spot obtained without the μ -SIL. It is to be noticed that the size of the measured spot is larger than the simulated ones. This can be attributed to the experimental conditions and the aberration of the optical system, primarily the positioning of the μ -SIL with respect to the focal plane. Nevertheless, the reduction in focused spot is observed in simulation and experiment. Hence, a tightly focused spot can be generated by use of a μ -SIL.

6.3.2 Visibility studies

The focused spot with the μ -SIL in the focal plane is characterized in section 6.3.1, and shows reduction of the point spread function by approximately the factor of the refractive index of the immersion system. In an imaging application, the reduced PSF is expected to provide improved image quality. In order to prove this hypothesis, we used this system to scan a periodic grating in reflection mode, as illustrated in Fig. 6.8.

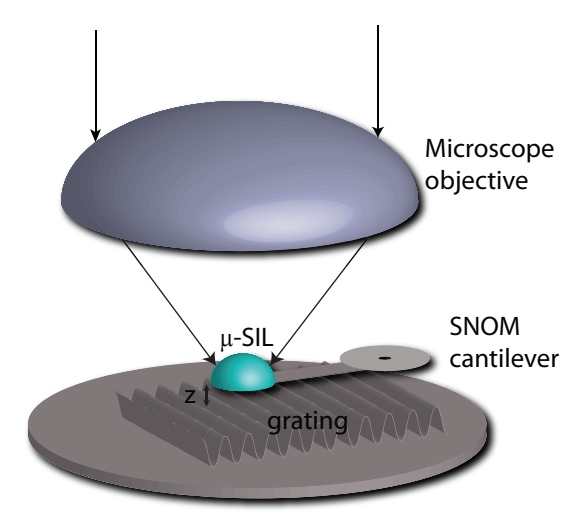


Figure 6.8: Schematics of the arrangement used for point to point scan measurement of the grating for visibility test in presence of μ -SIL.

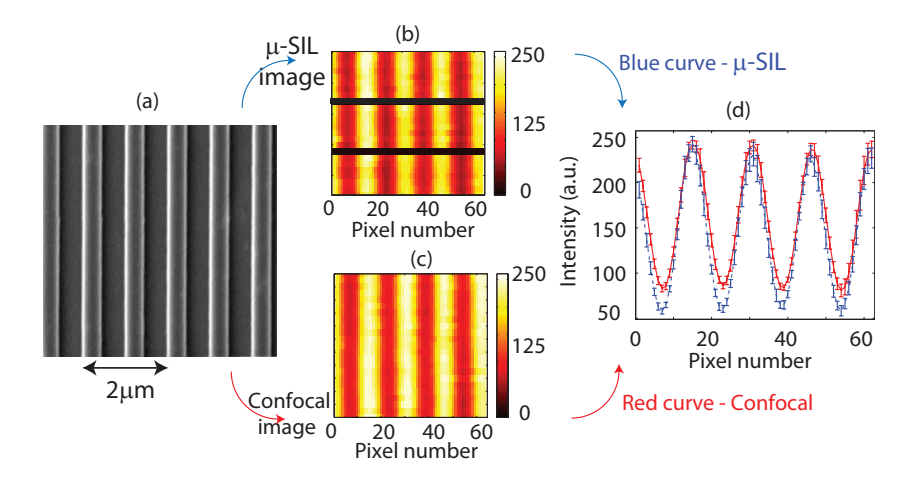


Figure 6.9: Imaging properties of the μ -SIL when point to point scanning is performed with μ -SIL and confocal microscopy. There is an enhancement in contrast with μ -SIL compared to confocal microscopy. (a) SEM image of the grating, (b) Image of point by point scanning by μ -SIL for different heights. Black lines separates the three sets of different scans. (c) Confocal image of point by point scanning of the grating without the μ -SIL, (d) Intensity signal averaged over the measurements.

The incident beam on the microscope objective is focused at the bottom planar surface of the μ -SIL, which is at distance z (with $z << \lambda$) from the grating. The reflected signal is measured. We use this configuration in order to use the μ -SIL arrangement to obtain the far field in CFS. Here the μ -SIL is mounted on the

SNOM cantilever and is used to scan the periodic grating. The grating under investigation is a chromium grating deposited on a glass substrate fabricated by focused ion beam. The period of the grating is 1 μ m with midCD=500 nm. Figure 6.9 (a) shows the SEM image of the sample grating. Whereas, Fig. 6.9 (b) represents the image of point by point scanning by μ -SIL for three different heights of the μ -SIL with respect to the sample surface. Black lines separates the three sets of different scans. Also, Fig. 6.9 (c) shows the confocal image of point by point scanning of the grating without the μ -SIL, here the scanning is performed by the focused spot formed by the microscope objective of NA=0.6 and Fig. 6.9 (d) is the intensity signal averaged line-per-line over the measurements.

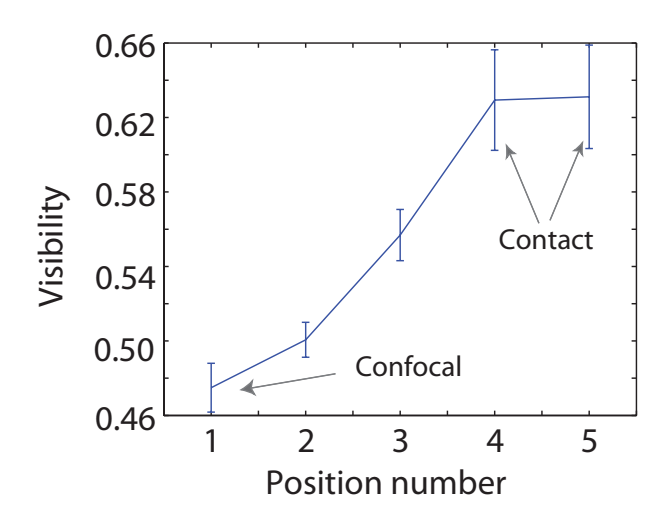


Figure 6.10: Visibility of the measured signal. Visibility of the data with μ -SIL is 30% higher than compared to confocal microscopy image.

We compare the image quality with and without the micro SIL by calculating the visibility of the scanned images for the confocal (no micro SIL) and with the micro SIL at different distances from the sample. The visibility can be computed using the difference of maximum signal on the groove height and the minimum signal recorded in the groove depth of the grating respectively normalized by the sum of the individual signals. In Fig. 6.10, visibility (on the vertical axis) is plotted corresponding to the confocal case and the μ -SIL. On the horizontal axis is the different position which means the relative height between the μ -SIL and the grating. The visibility corresponding to confocal microscopy (position1) is ≈ 0.48 , while the maximum visibility for the μ -SIL is ≈ 0.64 (positions 4 and 5). The last two positions namely positions 4 and 5 have identical visibility. This corresponds to the situation when the μ -SIL and the grating are in contact with each other. Position 2 and 3 are intermediate position between the grating and the μ -SIL. Consecutive positions in the plot of Fig. 6.10 (position number) correspond to a distance of approximately ≈ 250 nm.

6.4 SIL based scatterometer

High NA scatterometer is desirable to resolve the fine structures compared to the low NA scatterometer. In this chapter we introduce the idea of a SIL based scatterometer, where a solid immersion lens is the driving factor to achieve high NA while the increase in resolution is mainly attributed to the evanescent wave coupling. The increase in NA of the SIL scatterometer is multiple times the dry air NA of the the focusing objective, given by the refractive index of the SIL. But, the condition for evanescent wave coupling introduces the constraint on the distance between the solid immersion lens and the wafer under investigation.

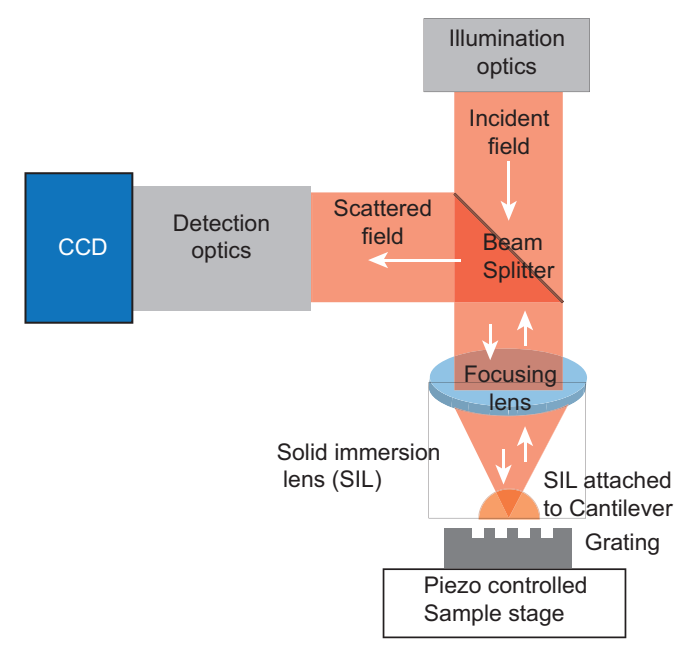


Figure 6.11: Schematic of the SIL scatterometer.

.

In Fig. 6.11, the idea of SIL scatterometer is shown. The basic layout of the solid immersion lens (SIL) scatterometer is similar to the Fourier scatterometer described in the thesis, with an additional SIL positioned between the sample and the MO. For the normal incidence of the ray on the SIL top surface from the MO, the position of SIL is fixed such that the flat bottom surface of the SIL is at the focal plane of the MO. This ensures the perpendicular incidence on the SIL from the MO, reducing the aberrations of the scatterometry system. This constraints the position of the SIL with respect to the MO. The SIL which can be used in SIL scatterometry is preferably as small as possible, so that control of the SIL positions can be easily controlled and monitored.

In CFS, the diffraction limited focused spot interacts with the sample and hence a micro-SIL is an optimal choice. In applications where an incoherent light is used

and a larger focused spot is desired, then a larger SIL is required to accommodate the large focus spot grating interaction. Although the SIL based scatterometer promises a highly sensitive scatterometer for smaller structures, there are few issues which need to be addressed for a SIL based working scatterometer. Some of the issues are listed here:

• SIL and MO optical axis alignment:

The optical axis of the MO and the SIL has to be aligned to coincide, to ensure perpendicular incidence on the SIL surface. At present this is done in imaging mode for the symmetric focus spot image. Unwanted Fringes might appear in case of misalignment.

- SIL distance control from the sample surface: SIL distance control requires sophisticated feedback piezo controllers. Due to the complexity in the setup, we place the SIL directly on the sample to guarantee contact between the SIL and the sample.
- SIL aberrations effects on the actual grating reconstruction:
 We expect the SIL aberrations combined with the optical aberrations in the system is crucial for data matching with simulations for the reconstruction. Hence, aberrations of the optical system with SIL should be taken into forward model to predict the experimental outcome.

6.4.1 μ -SIL CFS: test measurement

Using the experimental setup described in Fig. 4.5, we have obtained the signal, in the far field from a grating. The CFS scatterometer is first aligned without the SIL, then the SIL is placed underneath the MO. The SIL surface and the focused spot is imaged by the imaging arm in the scatterometer. When the SIL is in center and focus of the MO, then the imaged focused spot is symmetric and the symmetricity of the focused spot on the camera is used to align the SIL with respect to the MO. Some of the preliminary measurements performed are shown here.

Figure 6.12, shows the image of the Si_3N_4 membrane and the μ -SIL with the imaging arm in the coherent Fourier scatterometer described in Fig. 4.5 of the thesis. Figure 6.12 (a) is the image of the μ -SIL membrane and the μ -SIL, while Fig. 6.12 (b) is the focused spot imaged on the μ -SIL membrane from the main scatterometry arm. In Fig. 6.12 (c), it shows the image of the focused spot aligned on the μ -SIL. This ensures alignment of focused spot and μ -SIL for scatterometry applications.

6.5. Conclusions 97

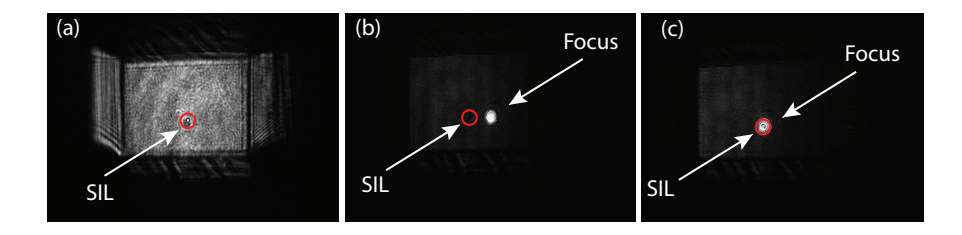


Figure 6.12: Image of the (a) μ -SIL and the membrane support, (b) the focused spot and μ -SIL separated from each other, (c) focused spot aligned on μ -SIL.

Figure 6.13 is the pupil image when the SIL is placed over the plane Si wafer sample (Fig.6.13(a)) and SIL over the grating of period 1.3 μ m (Fig.6.13(c)). Figure (Fig.6.13(b)) is the pupil image in absence of SIL for the grating. The fringes in the figures is due to the refractive index mismatch between the Si wafer and the SIL at the incident wavelength of 633 nm. From the figure it is clear that the SIL and the sample were not ideally in contact.

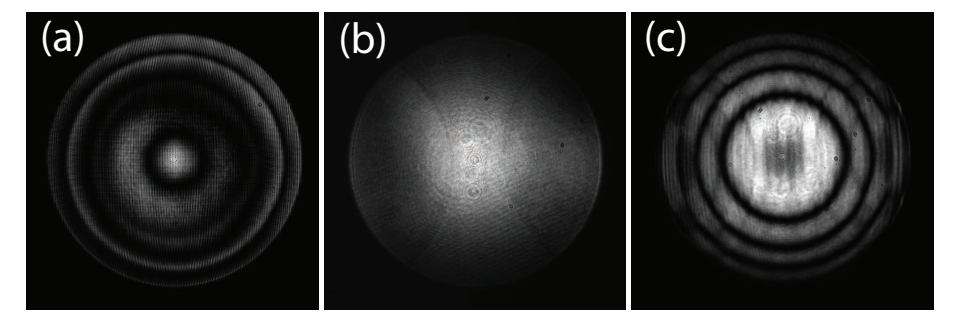


Figure 6.13: Pupil image for NA=0.4 with incident wavelength of 633 nm and period of the grating = $1.3~\mu m$. (a) Pupil image when the SIL is in contact with the planar surface, (b) Pupil image for grating in absence of SIL, (c) Pupil image for grating with SIL in contact with grating.

It can be seen from Fig. 6.13, that the overlapping between the diffracted orders in the far field in presence of the SIL is higher then without the SIL. Further study will be required to demonstrate the grating reconstruction from the far field data obtained from the scatterometer equipped with SIL.

6.5 Conclusions

We implement a μ -solid immersion lens to improve the resolution in a scanning near field microscope setup. Numerical and experimental results show the increased resolution, measured based on the focused spot size and visibility studies in the SIL based microscope compared to the confocal imaging. It has also been demonstrated that μ -SIL can be used as a near field probe in SNOM applications.

The applicability of micro-SIL for optical metrology applications is presented with the idea of high NA coherent Fourier scatterometer. The idea, implementation and challenges associated with a Fourier scatterometer with a μ -SIL is presented in the chapter.



Reconstruction of unintentional surface over-layer on Si grating

7.1 Abstract

The shape parameters are determined inversely from the far field intensity in grating reconstruction. When the feature size of the grating is in the tens of nanometers range, any unwanted surface layer of a few nm on the grating is expected to affect the far field intensity maps. Assuming that the distribution of the surface layers (for example: native silicon oxide, contamination and traces of resist removal) are identical on the wafer area with and without the structure, the effect of the thickness of oxide layer on the Si-etched grating can be studied and investigated using inverse grating reconstruction. The forward simulations have been performed by rigorous coupled wave analysis. Optical properties of the surface over-layer are measured by ellipsometry and the error, accuracy in grating parameters reconstruction in presence of oxide layer is presented.¹

¹This work will be published: N. Kumar, P. Petrik, S. F. Pereira and H. P. Urbach 'Reconstruction of unintentional surface over-layer on Silicon grating' (manuscript in preparation).

7.2. Introduction 101

7.2 Introduction

Solving inverse problems in grating reconstruction has attracted immense attention for its applicability in various fields, most importantly in the semiconductor industry. For this application high sensitivity, repeatability, high speed, nondestructiveness and high accuracy are desired. Recently, coherent Fourier scatterometry (CFS) has emerged as a new scatterometry technique, which under suitable conditions is very effective [32,33]. In CFS, a tightly focused spot interacts with the grating and the far field diffraction pattern is recorded for several scan positions. The diffraction efficiency of the propagating orders depends non-linearly on the material and shape parameters of the grating. The shape parameters are then determined inversely from the far field intensity [57]. An unintentional surface over-layer, that remains from the chemical process of grating fabrication can effect the grating reconstruction. This is important to understand the fabrication process and to fit the grating parameters with the expected structure. In Section 7.3, the model of the grating with oxide layer thickness is defined. In Section 7.4, ellipsometric characterization of the unwanted surface over-layer is presented and the grating parameters are reconstructed along with the thickness of the unwanted surface over-layer. The steps in the grating fabrication involve chemical treatment. Let us consider, an etched silicon (Si) grating on silicon wafer as substrate. For a reliable defect free fabrication process, a surface layer of few nano meters ($\approx 1.5 - 3$ nm) of native silicon oxide is present on the wafer (including the area where the grating is etched). This is common to any pristine silicon wafers. However, when the grating fabrication process is not perfect, then there is a possibility of formation or existence of an unwanted surface over-layer on the wafer surface. The layer thickness can be typically in the range up to few nanometers ($\approx 10 \text{ nm}$). The over-layer is either the mixed oxide, the residual or the contamination layer probably caused by the removal of the resist using plasma etching during the fabrication process. When the feature size of the grating is few tens of nanometers, then an unwanted surface over-layer of few nanometers on the grating is expected to affect the grating parameters reconstruction. The presence of the layer should be taken into account in the rigorous simulations. Assuming that the distribution of the surface over-layer (for example: native silicon oxide, contamination and traces of resist removal) is uniform on the wafer area with and without the structure, the effect of the thickness of the surface over-layer on the grating is studied and investigated using inverse grating reconstruction.

7.3 Native oxide over-layer effect

The presence of an unwanted surface over-layer on the grating structure in CFS is characterized by the change in the far field intensity compared to the case, when there is no surface over-layer present on the structure. In general, the presence of native oxide as a surface over-layer is unavoidable. In CFS, being a phase sensitive technique, one can expect that the thickness of the unwanted surface over-layer could be measured unambiguously, if the optical constants of the over-layer are known. To illustrate the effect of this layer on the structure, simulation studies

have been performed for changes in the far field intensity maps, when the height of an oxide surface over-layer is varied on the structure. The simulations were performed by the rigorous solver (RCWA). The model of the grating with native oxide as an over-layer, used in simulations is shown in Fig. 7.1. The nominal height of the grating is illustrated as $h_{grating}$ and the oxide surface over-layer thickness is denoted by h_{oxide} . It is assumed that the oxide surface over-layer distribution is identical at the bottom surface and the top surface of the grating, while there is negligible deposition of the oxide over-layer on the vertical SWA's as illustrated in Fig. 7.1. In the simulations, we consider a focused beam incident

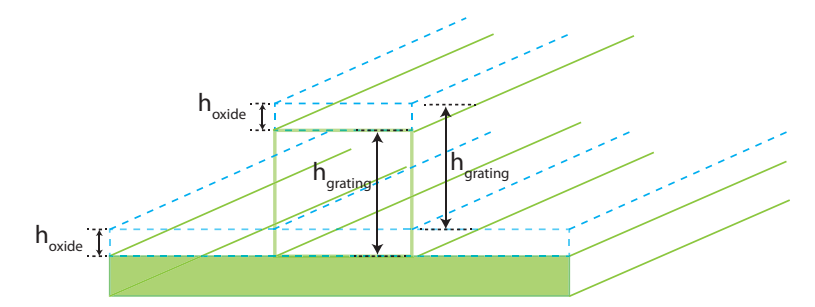


Figure 7.1: Cross-section of a one dimensional periodic grating (for one period) showing the presence of an oxide surface over-layer of thickness h_{oxide} on grating with height $h_{grating}$. The oxide surface over-layer distribution is identical at the bottom surface and the top surface of the grating.

on the grating and the reflected far field is recorded on a CCD detector in an epiillumination configuration i.e., the reflected light is collected by the same focusing lens. Figures 7.2 and 7.3 show the far field intensity maps simulated for a grating with nominal parameters. The nominal parameters are as follows: period, midCD, SWA and height as [300 nm, 100 nm, 90° (degrees), 80 nm], whereas, the oxide layer thickness in the simulations are varied up to 10 nm in a step of 2 nm. The noise in the simulation is a Gaussian, with zero mean and standard deviation of σ ($\sigma = 2.7 \times 10^{-4}$). The wavelength of illumination is 405 nm and the numerical aperture NA = 0.95. Figure 7.2 (a-f) shows the far field intensity maps when the incident light is TE-polarized in the entrance pupil of the focusing lens and the far field at the detector is of mixed polarization. The right-hand side column in Fig. 7.2 (a'-f') is the difference map of the intensities with and without oxide over-layer. It is observed that the magnitude of the difference map is higher than the noise level in the presence of an oxide over-layer of thickness as low as 2 nm, and hence can be distinguished from each other. This indicates that with a highly stable experimental setup, it is possible to retrieve the height of the oxide layer within nm accuracy on the structured surface, when the thickness of the overlayer is not correlated with the other grating parameters. Figure 7.3 shows similar behavior, when the incident polarization is TM. Also, it can be seen that in Fig. 7.3 (a'-f'), the difference is slightly higher compared to the difference intensity for TE incident polarization on the grating for the change in oxide layer thickness.

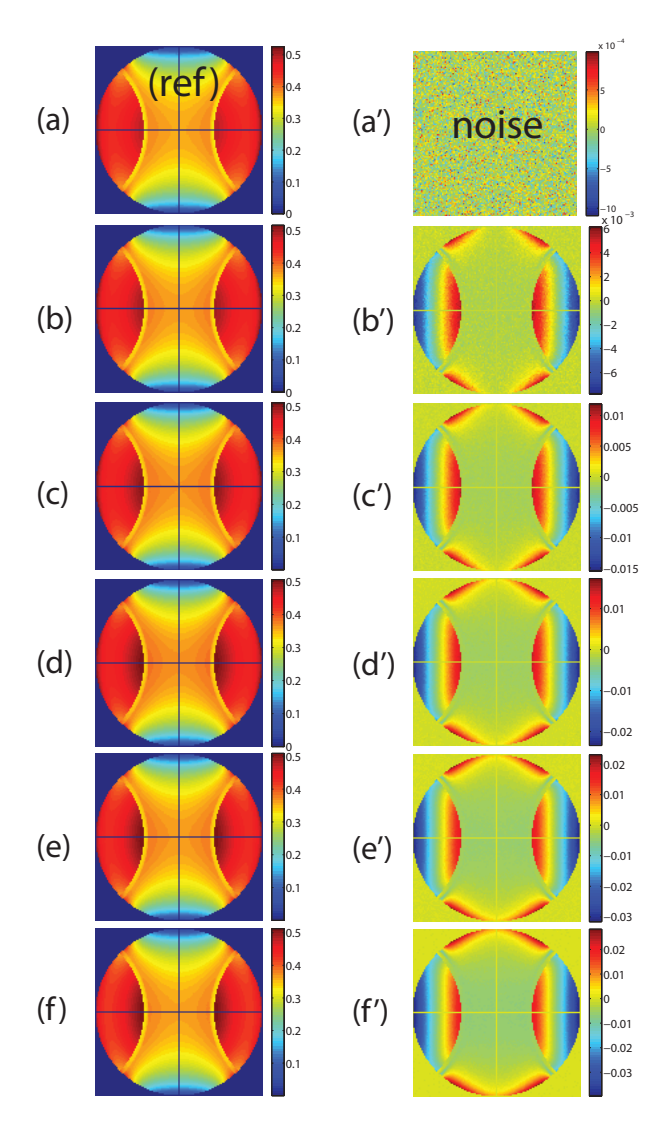


Figure 7.2: Far field intensity for varying oxide layer thickness and difference between the reference (without oxide layer) and intensity maps for varying oxide layer is shown. The numerical aperture of the focusing lens is 0.95 and the incident polarization in the entrance pupil is TE, and the output is of mixed polarization. The left-hand side column (a, b, c, d, e, f) represents the far field intensity maps for oxide layer thickness of 0 nm, 2 nm, 4 nm, 6 nm, 8 nm and 10 nm respectively. The right-hand side column (a',b', c',d', e', f') is the difference intensity of the reference (without oxide) and that of oxide layer thickness of 0 nm, 2 nm, 4 nm, 6 nm, 8 nm and 10 nm respectively.

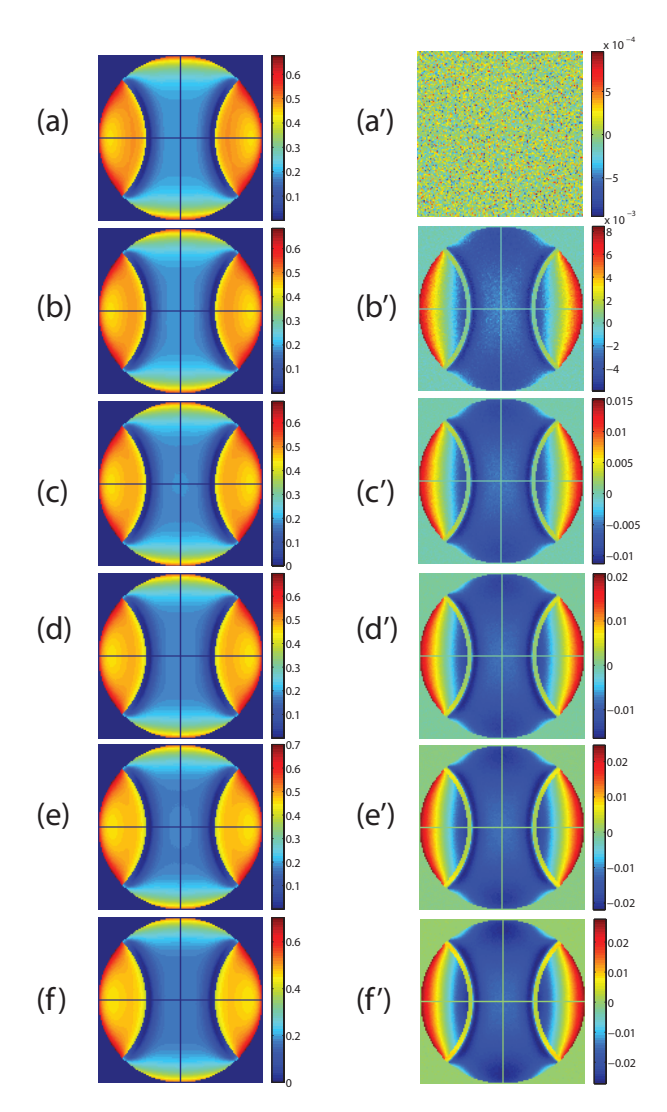


Figure 7.3: Far field intensity for varying oxide layer thickness and difference between the reference (without oxide layer) and intensity maps for varying oxide layer is shown. The numerical aperture of the focusing lens is 0.95 and the incident polarization in the entrance pupil is TM, and the output is of mixed polarization. The left-hand side column (a, b, c, d, e, f) represents the far field intensity maps for oxide layer thickness of 0 nm, 2 nm, 4 nm, 6 nm, 8 nm and 10 nm respectively. The right-hand side column (a',b', c',d', e', f') is the difference intensity of the reference (without oxide) and that of oxide layer thickness of 0 nm, 2 nm, 4 nm, 6 nm, 8 nm and 10 nm respectively.

The effect of an oxide over-layer thickness also depends upon the nominal height of the grating. To study the effect of an oxide over-layer for height (grating's nominal height) dependence with incident polarization, we choose gratings with fixed period, midCD and SWA and the nominal height of the grating is varied. The grating parameters are now given as: period, midCD, SWA and height as [300 nm, 100 nm, 90° (degrees), 40 - 80 nm]. At each nominal height of the grating an oxide layer is varied up to 10 nm. The illumination conditions are similar to the Figs. 7.2 and 7.3. The quantity quantifying the difference in the far field for I_{ref} and I_{oxide} is plotted on the vertical axis in Figs. 7.4 and 7.5, when the incident light above the microscope objective are TE and TM polarized respectively. In Figs. 7.4 and 7.5, different color-coded graphs represent the different nominal heights of the grating. The oxide over-layer thickness is plotted on the horizontal axis.

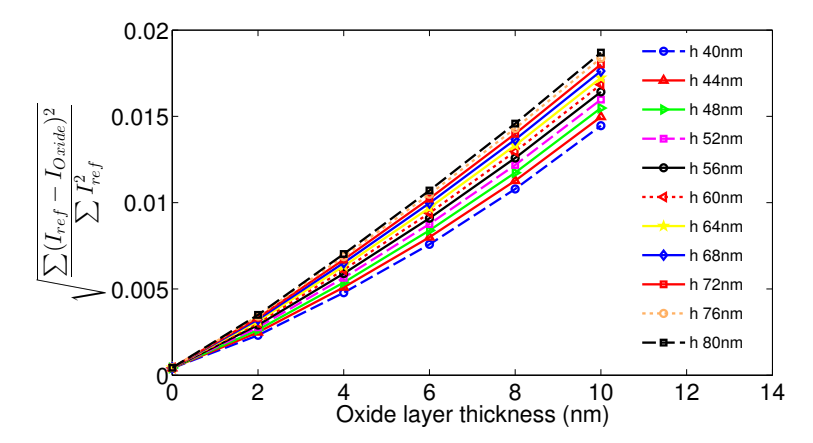


Figure 7.4: Relative difference between the far field intensities of structure with and without oxide for TE incident and mixed output polarizations. Different color coded graphs represent the different nominal heights of the grating. The nominal heights of the grating are varied from 40 nm to 80 nm. The oxide layer thickness is plotted on the horizontal axis and it is varied from 0 to 10 nm on the grating.

In Figs. 7.4 and 7.5, it can be seen that with an increase in thickness of the oxide over-layer there is a monotonic increase in the difference signal plotted on the vertical axis. Figure 7.4 shows that for TE incident polarization while Fig. 7.5 corresponds to TM incident polarization. For varying nominal height of the gratings, the difference due to presence of an oxide over-layer gets more prominent with an increase in its thickness. For TE incident polarization, the effect of oxide increases linearly for increasing nominal height for a constant oxide layer thickness. In Fig. 7.4, nominal height of 80 nm has the highest slope while for 40 nm it is minimum.

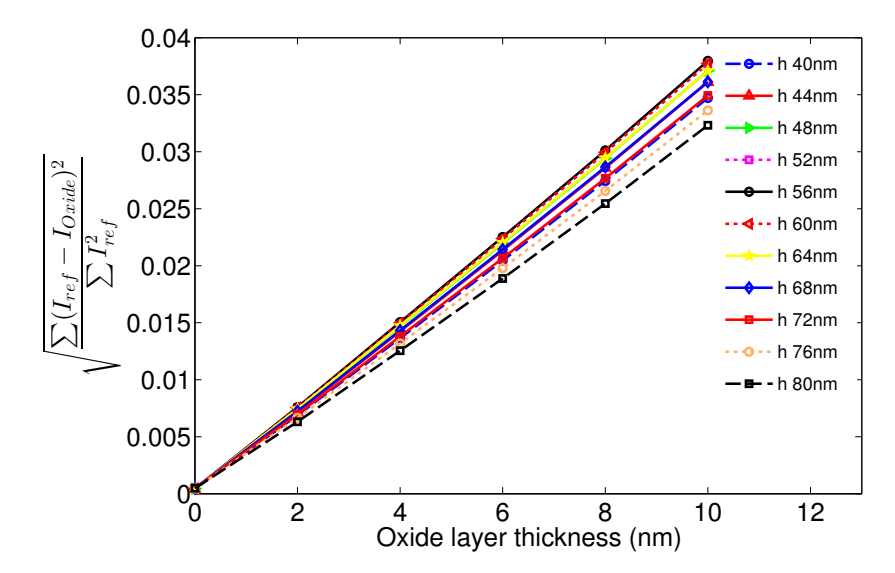


Figure 7.5: Relative difference between the far field intensities of structure with and without oxide for TM incident and mixed output polarizations. Different color coded graphs represent the different nominal heights of the grating. The nominal heights of the grating are varied from 40 nm to 80 nm. The oxide layer thickness is plotted on the horizontal axis and it is varied from 0 nm to 10 nm on the grating.

Figure 7.5 shows the difference signal for TM incident polarization and it is observed that the magnitude of the difference signal is approximately twice as large as that in Fig. 7.4, when the incident light is TE polarized. Also, the slope of the difference map is linearly dependent on the nominal height of the grating but is not maximum for the maximum height. Hence, it can be inferred that TM incident polarization is more sensitive to the presence of an surface oxide over-layer. If taken into account, it can be reconstructed in CFS. When the unintentional surface over-layers are not considered, it can lead to a wrong reconstruction of the grating parameters. In Section 7.4, optical properties of an etched Si grating is studied with ellipsometry, and then the grating parameters are reconstructed with CFS. The effect of the the presence of an unintentional layer in the accuracy of grating parameters reconstruction is shown for experimental data.

7.4 Characterization and reconstruction

Reflection and transmission of light from a medium is determined by the complex refractive indices. A planar structure can be characterized for its thickness, refractive index and dispersion by the change in the state of polarization in the reflected light from the surface [83]. The polarization state of light upon reflection or transmission from the surface changes and in the general case becomes elliptical. Ellipsometry characterizes this change in polarization by measuring Ψ and Δ [84]. These ellipsometric angles represent the amplitude ratio and phase difference be-

tween the p- and s-polarized reflected or transmitted waves. The ellipsometric measurements are characterized by the complex reflectance quantity ρ defined as,

$$\rho = \tan \Psi \exp(i\Delta)$$

$$= \frac{E_{rp}}{E_{ip}} / \frac{E_{rs}}{E_{is}},$$
(7.1)

where E_{rp} and E_{rs} are the reflected p- and s-polarized fields from the sample, while E_{ip} and E_{is} are the incident p- and s-polarized fields. The sample thickness or the refractive index are determined using optical models, in which one assumes a layer structure and the refractive index of each layer at each wavelength. Using such models, Ψ and Δ can be calculated (for a set of wavelengths and a range of angle of incidence) and are compared with the measured Ψ and Δ . The thickness, refractive index etc., are fitted based on this model. In Section 7.4.1, the measured Ψ and Δ are shown (for wafer with the grating to be reconstructed by CFS, but on the area not covered by the grating) and then compared to the simulated ones for different models of fitting. The refractive index obtained for the surface over-layer is then used in CFS reconstruction of the grating parameters and the thickness of the surface over-layer on the structured area of the wafer.

The measurements were performed on the one dimensional etched Si grating fabricated by Eulitha (Villigen, Switzerland). The substrate being crystalline Si (100)-orientation with typically 2 nm of native oxide on top. The measurement field has dimension of $10 \text{ mm} \times 10 \text{ mm}$. The nominal grating parameters are listen in Table 7.2.

7.4.1 Ellipsometry measurement

In case of a successful grating fabrication, surface over-layers can be accurately fitted by ellipsometry using a native oxide reference layer with a thickness of $\approx 1.5-3$ nm. The wafer surface with grating for CFS reconstruction was studied with ellipsometry and found to have an unintentional surface over-layer, as shown in Fig 7.6. The ellipsometry measurements were carried out on the wafer in the area with no structure, and hence in approximation described in Section 7.2 (distribution of the surface over-layer is uniform on the wafer surface both within and outside of the structured area). From the study which assumes a thermal oxide layer, the surface over-layer is equivalent to a SiO₂ thickness of 6.9 nm, but the experimental fit have large MSE (Mean square error ≈ 10) with this model, which indicates that the material of the surface layer is not purely SiO₂. The results show that there is an unintentional surface over-layer after grating processing (probably caused by the removal of the resist using plasma treatment), which is important to be taken into account in the simulation for the grating reconstruction.

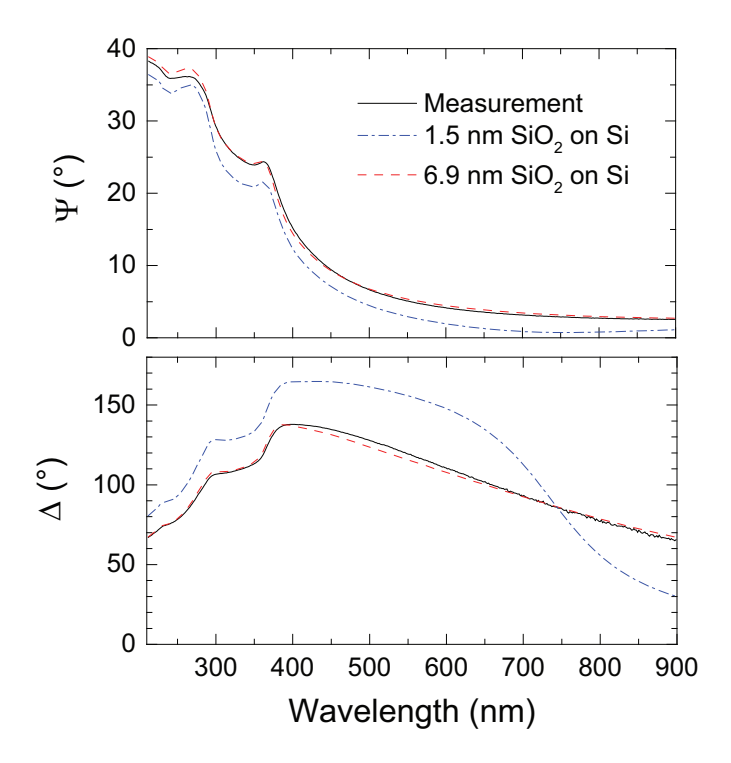


Figure 7.6: Measured and simulated ellipsometric angles. The measurement was made on a Si wafer with an etched grating, but measured on an area of the wafer that was not covered by the grating, in order to test the surface layer.

The unintentional surface over-layer has been investigated using different optical models, as shown in Table. 7.1; all models assume Si substrates. All of the models, SiO₂ (Model 1), Cauchy (Model 2) and EMA (Model 3) methods show relatively large deviations between the measured and fitted spectra (as revealed by Fig. 7.7). Model 1 uses the thermal SiO₂ reference of the ellipsometer manufacturer Wollam. The Cauchy formula of Model 2 calculates the refractive index using $n = A + \frac{B}{\lambda^2} + \frac{C}{\lambda^4}$ where λ is the incident wavelength. In the B-Spline approach of Model 3, several nodes can be defined in the spectrum, which are connected by polynomials, and the parameters are fitted between each node. Model 4 utilizes the effective medium approach using a single-crystalline Si (c-Si) component from the Woollam database and voids (n=1). Fitted height of the unintentional layer on the wafer surface based on the models is given in Table. 7.1.

Table 7.1: Optical models for the characterization of unintentional surface overlayers on gratings. Model 1 uses the thermal SiO_2 reference of the ellipsometer manufacturer Wollam. The Cauchy formula of Model 2 calculates the refractive index using $n=A+\frac{B}{\lambda^2}+\frac{C}{\lambda^4}$. In the B-Spline approach of Model 3, nodes can be defined in the spectrum, which are connected by polynomials, the parameters of which are fitted between each node. Model 4 utilizes the effective medium approach using a single-crystalline Si (c-Si) component from the Woollam database and voids (n=1).

Model 1: 6.9 nm SiO ₂	Model 2: 5.7 nm (Cauchy)
Model 3: 8 nm (B-Spline)	Model 4: 17.5 nm c-Si + 92 % voids

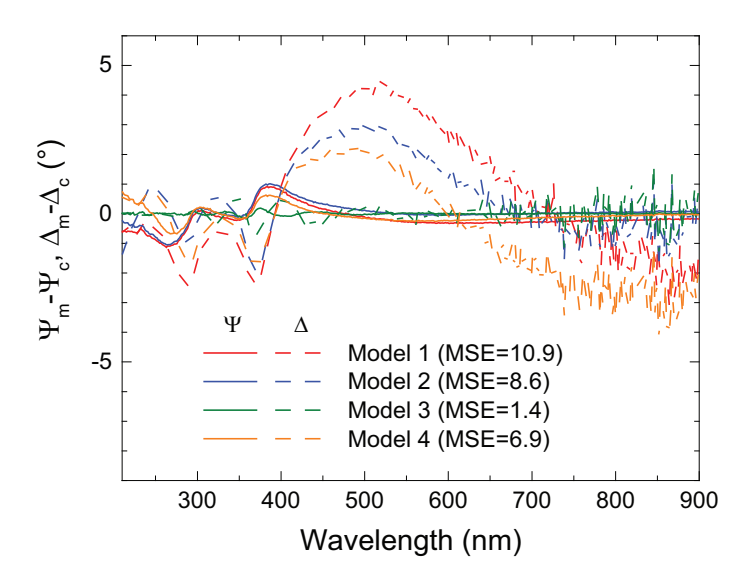


Figure 7.7: Difference between the measured and fitted Ψ and Δ spectra for the models shown in Table.7.1.

As it can be seen in Fig. 7.7, the fit quality of the B-Spline model is more accurate than compared to all the other models. The significant difference between the refractive indices calculated by the different models shows that the surface cannot be described by a single homogeneous layer accurately. The reason of the deviations is most probably the fact that the optical properties of the sample gradually change as a function of depth in a range of approximately 20 nm from the surface. Atomic force microscopy results show that the surface nano-roughness is in the range of 10 nm. In our models, this nano-roughness cannot be separated, because the unintentional surface layers are vertically inhomogeneous.

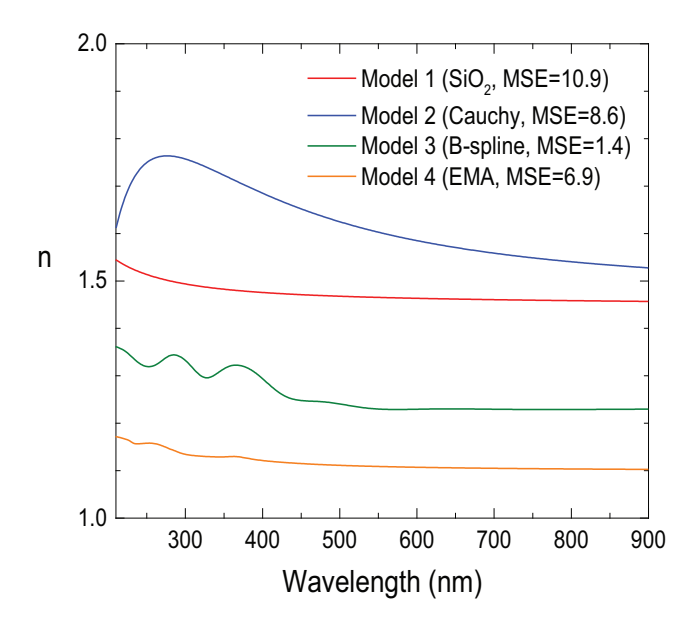


Figure 7.8: Refractive index spectra calculated from optical models shown in Table.7.1.

From the above analysis of fitting of the ellipsometry measurement on the wafer area for refractive index evaluation, we use the refractive index obtained from the B-Spline model. Hence, the refractive index of the unintentional surface over-layer used in RCWA simulation for grating reconstruction is n=1.23026-i0.00326 at an incident wavelength of 633 nm.

7.4.2 Reconstruction

The reconstructed grating shape parameters are presented in table 7.2. The height of the unintentional over-layer on the grating is also reconstructed based on the CFS far field data. The nominal grating parameters for the 1D grating as quoted by the manufacturer are: 301 nm midCD, 600 nm pitch and 345 nm etch depth. Moreover, the substrate is crystalline silicon in (100)-orientation with a native oxide layer of typically 2 nm thickness on top. Figure 7.9 and 7.10, show the experiment, simulation and the difference in the far field for TE and TM incident field in the entrance pupil respectively for the best fit solution of the grating parameters. The far fields shown in each figure correspond to 13 different scan positions with in a period of the grating separated by 50 nm each. The first and the last far field shown corresponds to a difference of one period of the grating and hence should be identical. The residuals in the difference map is attributed to the non-uniformity in phase and amplitude of the incident wave. In simulating the far field using RCWA from the grating, refractive index (n = 1.23026 - i0.00326 at

633 nm) of the unintentional surface layer (grating model described in Fig. 7.1) is used from section 7.4.1 for the best fit of the ellipsometric measurement. The experimental setup described in Fig. 4.5 is used to obtain the far field intensity maps.

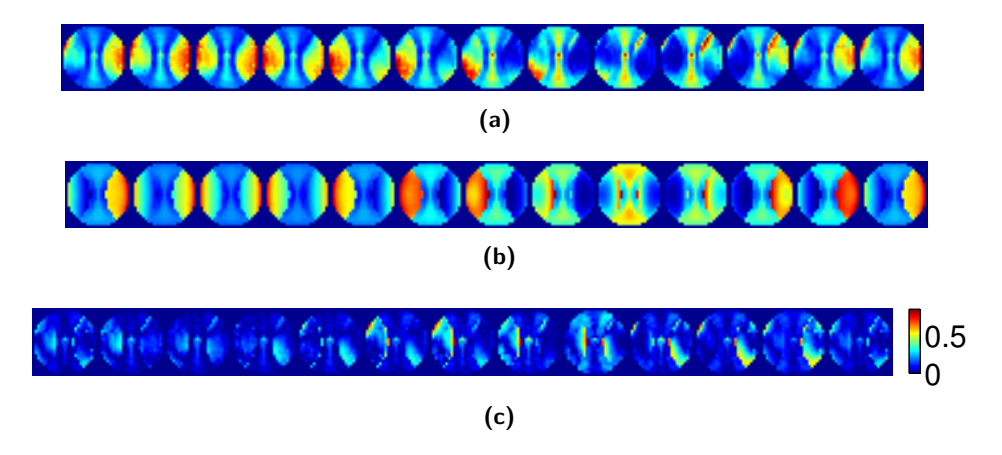


Figure 7.9: Far field intensity maps for scan positions separated by 50 nm within a single period of the grating for a grating of period 600 nm at illumination wavelength $\lambda=633$ nm and NA = 0.85. The incident light is TE polarized in the entrance pupil and the output is of mixed polarization. (a) Experimental far field intensity for bias position [0 nm - 600 nm] in the sequence from left to right in the row. (b) The simulated intensity maps for best fit parameters. (c) The difference between the simulation and the experiment.

Table 7.2: Grating parameter reconstruction in the presence of a surface over-layer on the grating structure

Grating parameters	CFS (with layer)	CFS (No layer)	DUV (PTB) [85]
midCD (nm)	298.8	296.6	301.5 ± 1.5
Height (nm)	363	360	361±1
SWA (degrees °)	85.4	88	83.8±0.3
Over-layer (nm)	5.17	0	4.9 ± 0.5

The difference between the simulation and the experiment is minimized by solving the non-linear least square for the set of grating parameters. Solving the optimization problem for the best fit of the experiment and simulations, the grating parameters are retrieved. In Table 7.2, the deviation in grating reconstruction with and without presence of the surface over-layer is shown. The reconstruction results on the Eulitha sample with DUV scatterometer performed at PTB (Germany), is also listed in Table 7.2 [85]. The thickness of the unintentional layer can be reconstructed with nm accuracy. It also shows that, if the thickness of the unintentional layer is not taken into account, then the optimization for grating pa-

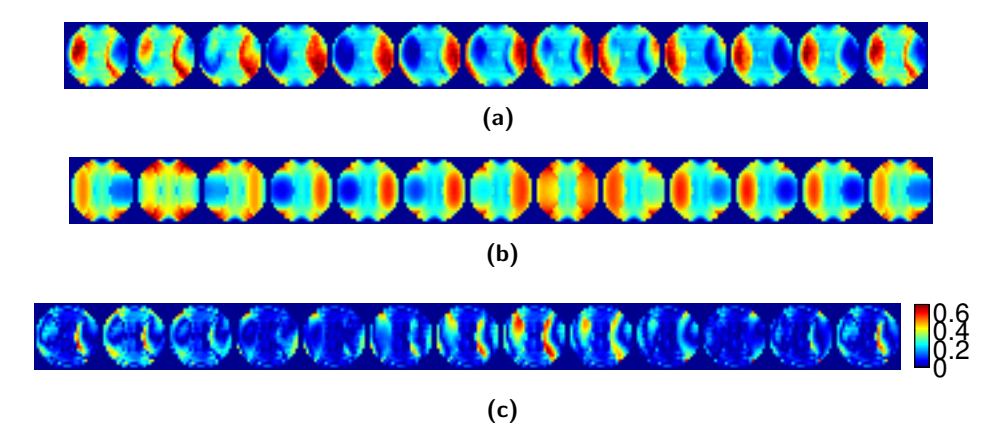


Figure 7.10: Far field intensity maps for focus positions separated by 50 nm within a single period of the grating for a grating of period 600 nm at illumination wavelength $\lambda=633$ nm and NA = 0.85. The incident light is TM polarized in the entrance pupil and the output is of mixed polarization. (a) Experimental far field intensity for bias position [0 nm - 600 nm] in the sequence from left to right in the row. (b) The simulated intensity maps for best fit parameters. (c) The difference between the simulation and the experiment.

rameters reaches a local minimum with different sets of grating parameters. There is also reasonable agreement with the reconstruction in [85], but not perfect.

7.5 Conclusions

The fabrication process for the grating can result in a surface over-layer. The presence of the unintentional surface over-layer of few nm of thickness, changes the far field of the grating compared to the far field in the absence of the surface over-layer. The changes in the far fields are studied for the TE and TM incident polarization in the entrance pupil of the microscope objective for varying oxide layer thickness over the gratings of several nominal height. Increase in the thickness of the surface over-layer results in an increased difference between the far fields corresponding to reference far field (grating with no oxide layer). Optical properties of the surface over-layers are measured by ellipsometry and the error, and the accuracy and sensitivity of grating parameters reconstruction in presence of oxide layer is discussed. Finally the grating parameters reconstruction shows that effect of the surface over-layer is crucial for the reconstruction of right set of grating parameters. The accuracy in determination of the refractive index of the over-layer is a critical issue for the actual height determination of the over-layer. Once determined, CFS is able to resolve few nano meters of unintentional surface over-layer on the grating structure.

Conclusions and Outlook

8.1 Conclusions

In the thesis a new method, coherent Fourier scatterometry (CFS), based on coherent illumination is introduced for optical metrology. After considering a specific model for the grating and the illumination, the estimated uncertainties of incoherent optical scatterometry (IOS) and CFS were compared under the assumption of the Gaussian distribution of the measurement noise with $\sigma = 2.7 \times 10^{-4}$. Based on the simulations, we conclude that CFS is more sensitive to change in grating shape parameters compared to IOS when there is an overlap between the diffracted orders in the exit pupil. In the event of no overlap between the diffracted orders the performance of the IOS and CFS are identical. CFS sensitivity is dependent on the initial position called bias in the thesis, when there is no scanning of focused spot on the grating. With increasing number of scanning positions within a period of the grating, the bias dependence of sensitivity can be avoided. It is also observed that there is an optimum number of scanning positions for a given period of the grating which depends on the number of overlapping orders in the exit pupil. Scanning is the most important aspect of CFS. Also, the incident polarization plays an important role in the sensitivity analysis and the different grating parameters respond to it in a non-linear, non-monotonic way.

There is phase information available in CFS owing to the coherent illumination. Intensity data with phase between scattered orders is the maximum information that can be extracted in CFS, as we have the amplitude and phase of all the four components of the scattering matrix except for an overall phase. The applicability of temporal phase shifting interferometry in coherent Fourier scatterometry with a scanning spot is presented to retrieve the partial phase information between the scattered orders. An analytical relation is derived and illustrated for the phase difference between two overlapping orders in the exit pupil and the results are compared with rigorous simulations. The polarization dependent phase sensitivity of the grating parameters is presented. Also, the importance of phase information in inverse problem of grating reconstruction is highlighted.

Grating reconstruction with CFS has been demonstrated experimentally. The

experimental setup is capable of illuminating and measuring the response of the sample simultaneously over a broad range of incident and reflected angles and for two orthogonal incident polarizations. The capabilities of the tool were demonstrated by reconstructing the parameters of grating with 1300 nm period using a wavelength of 633 nm and a microscope objective of NA = 0.4. The reconstruction was performed through a non-linear real time optimization. The uncertainties in reconstructed parameters are found to be comparable with the applied reference metrology techniques (SEM and AFM). Additionally, ± 1 nm accuracy in lateral positioning is shown, which corresponds to only 0.08% of the pitch of the grating used in the experiment. Simulation studies show that positioning accuracy of the order of 10 picometer with NA = 0.95 and wavelength in the UV can be achieved. Also, accurate nano-positioning in combination with the reconstruction shape parameters of the grating can be done in a single tool which is not possible with conventional optical scatterometry.

Mathematical analysis of overlay between two symmetric gratings of identical periods in the stack for coherent and incoherent scatterometry shows that the sum of the product of the reflection and transmission coefficients decides the magnitude of the asymmetry signal. Simulations studies show that the overlay signal in CFS is larger in magnitude than that of IOS. For the considered case, 2 times increase in asymmetry peak signal is observed in simulations. It is also inferred from the analysis that pupil engineering can enhance the capability of CFS for the overlay signals.

A micro solid immersion lens (SIL) is implemented to improve the resolution in a scanning near field optical microscope (SNOM) setup. Numerical and experimental results show the increased resolution based on the focused spot size and visibility studies in the SIL based microscope compared to the confocal imaging. The results shows that micro SIL can be used as a probe in SNOM setup. The applicability of micro-SIL for optical metrology applications is presented with the idea of high NA coherent Fourier scatterometer. The idea, implementation and challenges associated with a Fourier scatterometer with a micro-SIL is presented.

The presence of an unintentional surface over-layer of few nano meters thickness as a result of fabrication error in gratings, results in change in the far field compared to the nominal parameters. Optical properties of the surface over-layers are measured by ellipsometry and shows that effect of the surface over-layer is crucial for the reconstruction of right set of grating parameters. The accuracy in determination of the refractive index of the over-layer is a critical issue for the actual height determination of the over-layer. Once determined, CFS is able to resolve few nano meters of unintentional surface over-layer on the grating structure.

8.2 Remarks and Future works

The advantage of using CFS for periodic structures is limited by the existence of overlapping diffracted orders, which sets a requirement on the minimum value of period of the grating for a fixed incident wavelength and numerical aperture. Hence, any improvement in the direction of minimizing period of the grating is highly desired. There are several ways in which it can be achieved. Nevertheless, CFS can also be used as an optical metrology tool for non periodic structures.

8.2.1 Interferometric CFS

In CFS, further utilization of coherence is possible by making additional measurements using the principle of interferometry (for example: temporal phase shifting interferometry). Through numerical simulation, we show how scanning and interferometry can be coupled together to improve the sensitivity of CFS, to extend its range of applicability and to obtain sufficient information to calculate the complex scattering matrix for all angles of incidence inside the numerical aperture of a microscope objective [86]. An improvement of sensitivity in grating parameters is shown with interferometric CFS compared to CFS. In a comparison with coherent goniometric scatterometry, we showed that even though these two systems contain the same physical information about the sample, with scanning, interferometric CFS shows superior sensitivity. This is desirable for fast convergence of any optimization algorithm, a fact that is important for industrial applications. Extension of CFS tool to an interferometric configuration is easily achievable and the experimental implementation of the interferometric CFS is highly recommended in future for the validation of the simulation studies, and if demonstrated, CFS can be used for gratings with sub-wavelength pitch.

8.2.2 Ellipsometric CFS

Ellipsometric Fourier scatterometry: an extension of Fourier scatterometry is aiming at increasing the sensitivity by measuring the phase difference between the reections polarized parallel and perpendicular to the plane of incidence [87]. It can be applied by modulating the polarizations and analyzing the signal at each pixel of the CCD. This approach can also be applied to IOS. The ellipsometric approach requires no additional hardware elements compared with conventional Fourier scatterometry. Additionally for the forward computation of the far field, measurement of the incident amplitude and phase is not required. Ellipsometric CFS can further be extended for multi-wavelength analysis, which allows to build more complex models and investigate complex samples. Again, the experimental proof of the ellipsometric CFS should be a step forward in realizing the usability of polarization mixing in CFS.

8.2.3 Pupil engineering in CFS

The diffracted far field is obtained for the incident field interaction with the sample. Using beam shaping, the interaction between the incident field and the sample can be optimized for individual parameter of interest. Hence, pupil engineering for amplitude, phase, polarizations or in combination is worth investigating in future with CFS for increased sensitivity in grating parameters. Pupil engineering can also be used to enhance the capability of CFS while investigating non-periodic isolated structures.

In addition to the above mentioned topics, CFS can also be used with immersion techniques for parameter reconstruction of smaller gratings or smaller non-periodic objects. The immersion techniques may include liquid or solid immersion lens to increase the numerical aperture of the optical system.



Bucket algorithm for analytical reconstruction of the phase difference of overlapping orders

Let 1 < F < 2, and let the input and output polarizations be denoted by index μ and ν , respectively, where $\mu = \xi, \eta; \nu = \xi, \eta$. Then for a translation Δx of the grating, the total reflected field in a point of the exit pupil where the 0 and 1th reflected orders overlap is given by:

$$I_{\mu\nu}^{\Delta x} = \left| \underline{\widetilde{\underline{r}}}_{0,\mu\nu} \vec{a}_{\mu}^{i,0} \right|^2 + \left| \underline{\widetilde{\underline{r}}}_{1,\mu\nu} \vec{a}_{\mu}^{i,1} \right|^2 + 2 \left| \underline{\widetilde{\underline{r}}}_{0,\mu\nu} \vec{a}_{\mu}^{i,0} \right| \left| \underline{\widetilde{\underline{r}}}_{1,\mu\nu} \vec{a}_{\mu}^{i,1} \right| \cos \left(\Delta \Phi_{\mu\nu}^{(0,1)} + 2\pi \frac{\Delta x}{\Lambda} \right)$$
(A.1)

where the superscripts 0 and 1 of the incident field are to indicate that the incident field has to be evaluated in the pupil points corresponding to the 0th and 1st reflected orders. If the grating is scanned within one period such that $2\pi\frac{\Delta x}{\Lambda} = \frac{\pi}{2}$, π , $\frac{3\pi}{2}$ and 2π , the measured intensities are

$$I_{\mu\nu}^{x_0} = \left| \underline{\widetilde{r}}_{0,\mu\nu} \vec{a}_{\mu}^{i,0} \right|^2 + \left| \underline{\widetilde{r}}_{1,\mu\nu} \vec{a}_{\mu}^{i,1} \right|^2 + 2 \left| \underline{\widetilde{r}}_{0,\mu\nu} \vec{a}_{\mu}^{i,0} \right| \left| \underline{\widetilde{r}}_{1,\mu\nu} \vec{a}_{\mu}^{i,1} \right| \cos \left(\Delta \Phi_{\mu\nu}^{(0,1)} \right)$$
(A.2)

$$I_{\mu\nu}^{x_1} = \left| \widetilde{\underline{r}}_{0,\mu\nu} \vec{a}_{\mu}^{i,0} \right|^2 + \left| \widetilde{\underline{r}}_{1,\mu\nu} \vec{a}_{\mu}^{i,1} \right|^2 - 2 \left| \widetilde{\underline{r}}_{0,\mu\nu} \vec{a}_{\mu}^{i,0} \right| \left| \widetilde{\underline{r}}_{1,\mu\nu} \vec{a}_{\mu}^{i,1} \right| \sin \left(\Delta \Phi_{\mu\nu}^{(0,1)} \right)$$
(A.3)

$$I_{\mu\nu}^{x_2} = \left| \underline{\widetilde{r}}_{=0,\mu\nu} \vec{a}_{\mu}^{i,0} \right|^2 + \left| \underline{\widetilde{r}}_{=1,\mu\nu} \vec{a}_{\mu}^{i,1} \right|^2 - 2 \left| \underline{\widetilde{r}}_{=0,\mu\nu} \vec{a}_{\mu}^{i,0} \right| \left| \underline{\widetilde{r}}_{=1,\mu\nu} \vec{a}_{\mu}^{i,1} \right| \cos \left(\Delta \Phi_{\mu\nu}^{(0,1)} \right) \quad (A.4)$$

$$I_{\mu\nu}^{x_3} = \left| \widetilde{\underline{r}}_{0,\mu\nu} \vec{a}_{\mu}^{i,0} \right|^2 + \left| \widetilde{\underline{r}}_{1,\mu\nu} \vec{a}_{\mu}^{i,1} \right|^2 + 2 \left| \widetilde{\underline{r}}_{0,\mu\nu} \vec{a}_{\mu}^{i,0} \right| \left| \widetilde{\underline{r}}_{1,\mu\nu} \vec{a}_{\mu}^{i,1} \right| \sin \left(\Delta \Phi_{\mu\nu}^{(0,1)} \right) \quad (A.5)$$

Rearranging the above equations, we can retrieve the phase difference of the contributing reflected orders for the chosen polarizations as:

$$\Delta\Phi_{\mu\nu}^{(0,1)} = \arctan \frac{I_{\mu\nu}^{x_3} - I_{\mu\nu}^{x_1}}{I_{\mu\nu}^{x_1} - I_{\mu\nu}^{x_0}}$$
(A.6)

В

Experimental laboratory setup

Experiemtnal setup for coherent Fourier scatterometry



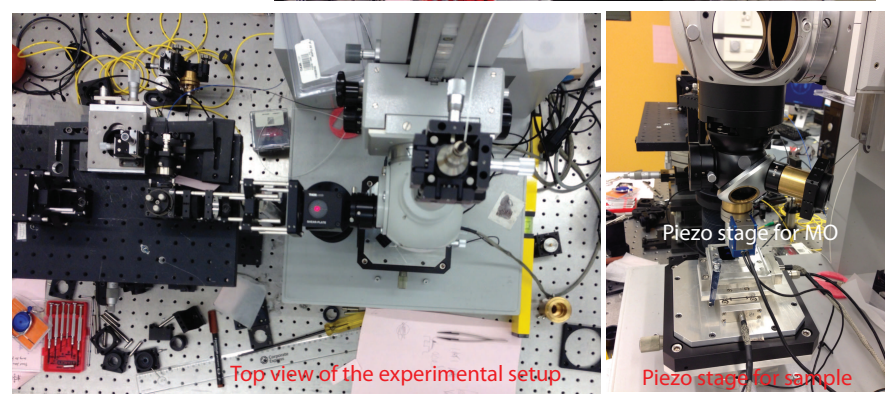


Figure B.1: Experimental setup for coherent Fourier scatterometry in the cleanroom facilty at VLL, TU Delft.

- [1] "International technology roadmap for semiconductors," 2012, available from http://www.itrs.net/Links/2012ITRS/2012Chapters/2012Overview.pdf.
- [2] C. Edwards, A. Arbabi, G. Popescu, and L. L. Goddard, "Optically monitoring and controlling nanoscale topography during semiconductor etching," *Light: Science and Applications*, vol. 1, p. e30, 2012.
- [3] E. Vogel, "Technology and metrology of new electronic materials and devices," *Nature Nanotechnology*, vol. 2, pp. 25–32, 2007.
- [4] J. Lindberg, "Mathematical concepts of optical superresolution," *Journal of Optics*, vol. 14, no. 8, p. 083001, 2012.
- [5] H. P. Baltes, Inverse source problems in optics / edited by H. P. Baltes; with contributions by H. P. Baltes et al.; with a foreword by J. F. Moser. Springer-Verlag, Berlin; New York, 1978.
- [6] C. Raymond, "Overview of scatterometry applications in high volume silicon manufacturing," AIP Conference Proceedings, vol. 788, no. 1, pp. 394–402, 2005.
- [7] H. T. Huang and F. L. Terry-Jr, "Erratum to 'Spectroscopic ellipsometry and reflectometry from gratings (Scatterometry) for critical dimension measurement and in situ, real-time process monitoring'," *Thin Solid Films*, vol. 468, no. 1-2, pp. 339–346, 2004.
- [8] Q. Zhan and J. R. Leger, "High-resolution imaging ellipsometer," *Applied Optics*, vol. 41, no. 22, pp. 4443–4450, 2002.
- [9] P. Boher, J. Petit, T. Leroux, J. Foucher, Y. Desieres, J. Hazart, and P. Chaton, "Optical Fourier transform scatterometry for LER and LWR metrology," Proceedings of SPIE, vol. 5752, pp. 192–203, 2005.
- [10] H. Gross, J. Richter, A. Rathfeld, and M. Bär, "Investigations on a robust profile model for the reconstruction of 2D periodic absorber lines in scatterometry," *Journal of the European Optical Society Rapid Publications*, vol. 5, no. 2, p. 10053, 2010.

[11] H. Gross, R. Model, M. Bär, M. Wurm, B. Bodermann, and A. Rathsfeld, "Mathematical modelling of indirect measurements in scatterometry," *Measurement: Journal of the International Measurement Confederation*, vol. 39, no. 9, pp. 782–794, 2006.

- [12] M. Wurm, F. Pilarski, and B. Bodermann, "A new flexible scatterometer for critical dimension metrology," *Review of Scientific Instruments*, vol. 81, no. 2, p. 023701, 2010.
- [13] V. F. Paz, S. Peterhänsel, K. Frenner, and W. Osten, "Solving the inverse grating problem by white light interference Fourier scatterometry," *Light: Science and Applications*, vol. 1, p. e36, 2012.
- [14] L. Asinovski, D. Beaglehole, and M. T. Clarkson, "Imaging ellipsometry: quantitative analysis," *Physica Status Solidi* (a), vol. 205, no. 4, pp. 764–771, 2008.
- [15] E. Halter, P. Montgomery, D. Montaner, R. Barillon, M. D. Nero, C. Galindo, and S. Georg, "Characterization of inhomogeneous colloidal layers using adapted coherence probe microscopy," *Applied Surface Science*, vol. 256, no. 21, pp. 6144 6152, 2010.
- [16] D. G. Stavenga, H. L. Leertouwer, P. Pirih, and M. F. Wehling, "Imaging scatterometry of butterfly wing scales," *Optics Express*, vol. 17, pp. 193–202, 2009.
- [17] B. K. Minhas, S. A. Coulombe, S. S. H. Naqvi, and J. R. McNeil, "Ellipsometric scatterometry for the metrology of sub-0.1- μ m-linewidth structures," *Applied Optics*, vol. 37, no. 22, pp. 5112–5115, 1998.
- [18] H. J. Patrick, T. A. Germer, Y. Ding, H. W. Ro, L. J. Richter, and C. L. Soles, "Scatterometry for in situ measurement of pattern reflow in nanoimprinted polymers," *Applied Physics Letters*, vol. 93, no. 23, p. 233105, 2008.
- [19] M. G. Moharam and T. K. Gaylord, "Rigorous coupled-wave analysis of planar-grating diffraction," *Journal of the Optical Society of America*, vol. 71, no. 7, pp. 811–818, 1981.
- [20] M. G. Moharam, D. A. Pommet, E. B. Grann, and T. K. Gaylord, "Stable implementation of the rigorous coupled-wave analysis for surface-relief gratings: enhanced transmittance matrix approach," *Journal of the Optical Society of America A*, vol. 12, no. 5, pp. 1077–1086, 1995.
- [21] L. Li, "Use of Fourier series in the analysis of discontinuous periodic structures," *Journal of the Optical Society of America A*, vol. 13, no. 9, pp. 1870–1876, 1996.
- [22] P. Lalanne and G. M. Morris, "Highly improved convergence of the coupled-wave method for TM polarization," *Journal of the Optical Society of America A*, vol. 13, no. 4, pp. 779–784, 1996.

[23] M. Born and E. Wolf, *Principles of Optics: Electromagnetic Theory of Propagation, Interference and Diffraction of Light*, 7th ed. Cambridge University Press, 1999.

- [24] M. van Kraaij and J. Maubach, "A more efficient rigorous coupled-wave analysis algorithm," in *Progress in Industrial Mathematics at ECMI 2004*, ser. Mathematics in Industry. Springer Berlin Heidelberg, 2006, vol. 8, pp. 164–168.
- [25] J. Hartmann, "Bemerkungen ueber den bau und die justierung von spktrographen," Zeitschrift fuer Instrumentenkunde, vol. 20, no. 47, 1900.
- [26] A. J. E. M. Janssen, J. J. M. Braat, and P. Dirksen, "On the computation of the nijboer-zernike aberration integrals at arbitrary defocus," *Journal of Modern Optics*, vol. 51, no. 5, pp. 687–703, 2004.
- [27] A. J. E. M. Janssen, "Extended nijboer–zernike approach for the computation of optical point-spread functions," *Journal of Optical Society of America A*, vol. 19, no. 5, pp. 849–857, 2002.
- [28] S. van Haver and A. J. E. M. Janssen, "Advanced analytic treatment and efficient computation of the diffraction integrals in the extended nijboer-zernike theory," *Journal of the European Optical Society Rapid publications*, vol. 8, no. 0, p. 13044, 2013.
- [29] A. P. Konijnenberg, L. Wei, N. Kumar, L. C. C. P. Filho, L. Cisotto, S. F. Pereira, and H. P. Urbach, "Demonstration of an optimised focal field with long focal depth and high transmission obtained with the extended nijboer-zernike theory," Optics Express, vol. 22, no. 1, pp. 311–324, 2014.
- [30] O. El Gawhary, A. Wiegmann, N. Kumar, S. F. Pereira, and H. P. Urbach, "Through-focus phase retrieval and its connection to the spatial correlation for propagating fields," *Optics Express*, vol. 21, no. 5, pp. 5550–5560, 2013.
- [31] A. C. Assafrao, N. Kumar, A. J. H. Wachters, S. F. Pereira, and H. P. Urbach, "Experimental and numerical analysis of the super resolution near-field effect on an insb sample," *Japanese Journal of Applied Physics*, vol. 53, no. 4, p. 042001, 2014.
- [32] O. El Gawhary, N. Kumar, S. F. Pereira, W. M. J. Coene, and H. P. Urbach, "Performance analysis of coherent optical scatterometry," *Applied Physics B*, vol. 105, no. 4, pp. 775–781, 2011.
- [33] N. Kumar, O. El Gawhary, S. Roy, V. G. Kutchoukov, S. F. Pereira, W. Coene, and H. P. Urbach, "Coherent Fourier scatterometry: tool for improved sensitivity in semiconductor metrology," *Proceedings of SPIE*, vol. 8324, pp. 83240Q-8, 2012.
- [34] S. Roy, O. El Gawhary, N. Kumar, S. F. Pereira, and H. P. Urbach, "Scanning effects in coherent Fourier scatterometry," *Journal of the European Optical Society Rapid Publications*, vol. 7, no. 0, p. 12031, 2012.

[35] R. Silver, T. Germer, R. Attota, B. M. Barnes, B. Bunday, J. Allgair, E. Marx, and J. Jun, "Fundamental limits of optical critical dimension metrology: a simulation study," *Proceedings of SPIE*, vol. 6518, pp. 65180U–17, 2007.

- [36] W. H. Press, S. A. Teukolsky, W. T. Vetterling, and B. P. Flannery, *Numerical recipes in C (2nd ed.): the art of scientific computing*. New York, NY, USA: Cambridge University Press, 1992.
- [37] H. M. L. Faulkner and J. M. Rodenburg, "Movable aperture lensless transmission microscopy: A novel phase retrieval algorithm," *Physical Review Letters*, vol. 93, no. 2, pp. 023 903–1, 2004.
- [38] A. M. Maiden, M. J. Humphry, F. Zhang, and J. M. Rodenburg, "Superresolution imaging via ptychography," *Journal of the Optical Society of America A*, vol. 28, no. 4, pp. 604–612, 2011.
- [39] N. Kumar, O. El Gawhary, S. Roy, S. F. Pereira, and H. P. Urbach, "Phase retrieval between overlapping orders in coherent Fourier scatterometry using scanning," *Journal of the European Optical Society - Rapid Publications*, vol. 8, no. 0, p. 13048, 2013.
- [40] R. M. Silver, B. M. Barnes, A. Heckert, R. Attota, R. Dixson, and J. Jun, "Angle resolved optical metrology," *Proceedings of SPIE*, vol. 6922, pp. 69221M–12, 2008.
- [41] M. Wurm, S. Bonifer, B. Bodermann, and M. Gerhard, "Comparison of far field characterisation of DOEs with a goniometric DUV-scatterometer and a CCD-based system," *Journal of the European Optical Society - Rapid Publi*cations, vol. 6, p. 11015s, 2011.
- [42] J. R. Fienup, "Phase retrieval algorithms: A comparison." *Applied Optics*, vol. 21, no. 15, pp. 2758–2769, 1982.
- [43] P. Hariharan, *Basics of interferometry*, 2nd ed. Academic Press, Amsterdam, 2007.
- [44] D. Malacara, Optical Shop Testing, 2nd ed. Wiley-Interscience, 1992.
- [45] M. Kujawinska, "Fresnel-field analysis of double-grating systems and their application in phase-stepping grating interferometers," *Journal of the Optical* Society of America A, vol. 5, no. 6, pp. 849–857, 1988.
- [46] M. R. Teague, "Irradiance moments: their propagation and use for unique retrieval of phase," *Journal of the Optical Society of America*, vol. 72, no. 9, pp. 1199–1209, 1982.
- [47] A. Barty, K. A. Nugent, D. Paganin, and A. Roberts, "Quantitative optical phase microscopy," *Optics Letters*, vol. 23, no. 11, pp. 817–819, 1998.
- [48] T. Gureyev and K. Nugent, "Rapid quantitative phase imaging using the transport of intensity equation," *Optics Communications*, vol. 133, no. 1-6, pp. 339 346, 1997.

[49] J. Miao, D. Sayre, and H. N. Chapman, "Phase retrieval from the magnitude of the Fourier transforms of nonperiodic objects," *Journal of the Optical Society of America A: Optics and Image Science, and Vision*, vol. 15, no. 6, pp. 1662–1669, 1998.

- [50] M. Born and E. Wolf, Principles of Optics. CambridgeUniversity Press, 1998.
- [51] D. W. Robinson, G. T. Reid, and P. D. Groot, "Interferogram analysis: Digital fringe pattern measurement techniques," *Physics Today*, vol. 47, no. 8, pp. 66–66, 1994.
- [52] R. R. Cordero, J. Molimard, A. Martínez, and F. Labbe, "Uncertainty analysis of temporal phase-stepping algorithms for interferometry," *Optics Communications*, vol. 275, no. 1, pp. 144–155, 2007.
- [53] L. Novotny and B. Hecht, *Principles of Nano-Optics*. Cambridge University Press, 2006.
- [54] V. S. Ignatowsky, "Diffraction by lens of arbitrary aperture," *Trans. Opt. Inst. petrograd*, vol. 1 (4), pp. 1–36, 1919.
- [55] E. W. B. Richards, "Electromagnetic diffraction in optical systems ii. structure of the image field in an aplanatic system," *Proceedings of the Royal Society of London. Series A. Mathematical and Physical Sciences*, vol. A 253, pp. 253–358, 1959.
- [56] M. G. Moharam, D. A. Pommet, E. B. Grann, and T. K. Gaylord, "Stable implementation of the rigorous coupled-wave analysis for surface-relief gratings: enhanced transmittance matrix approach," *Journal of the Optical Society of America A: Optics and Image Science, and Vision*, vol. 12, no. 5, pp. 1077–1086, 1995.
- [57] N. Kumar, P. Petrik, G. K. P. Ramanandan, O. El Gawhary, S. Roy, S. F. Pereira, W. M. J. Coene, and H. P. Urbach, "Reconstruction of subwavelength features and nano-positioning of gratings using coherent fourier scatterometry," Optics Express, vol. 22, no. 20, pp. 24678–24688, 2014.
- [58] O. El Gawhary and S. Petra, "Method and apparatus for determining structure parameters of microstructures," European patent (WO/2012/126718) and US patent US 20120243004 A1, 2012.
- [59] J. Goodman, *Introduction to Fourier Optics*, 3rd ed. Roberts and Company Publishers, 2004.
- [60] W. H. Swann, "A survey of non-linear optimization techniques," *FEBS Letters*, vol. 2, Supplement 1, pp. S39 S55, 1969.
- [61] H. Levinson, Principles of Lithography, ser. Press Monographs. SPIE Press Monograph, 2005, vol. PM198.

[62] J. T. Neumann, J. Lee, K. Yang, B. Lee, T. Lee, J. Park, C.-m. Lim, D. Yim, S. Park, E. Janda, K. Bhattacharyya, C.-h. Ryu, Y.-H. Min, K. Rhe, and B. Geh, "Overlay metrology for low-k₁: challenges and solutions," *Proceedings* of SPIE, vol. 8326, pp. 832602–21, 2012.

- [63] C. Mack, Fundamental Principles of Optical Lithography: The Science of Microfabrication. Wiley, 2008.
- [64] M. Ebert, H. Cramer, W. Tel, M. Kubis, and H. Megens, "Combined overlay, focus and CD metrology for leading edge lithography," *Proceedings of SPIE*, vol. 7973, pp. 797311–14, 2011.
- [65] H.-J. H. Smilde, M. Jak, A. den Boef, M. van Schijndel, M. Bozkurt, A. Fuchs, M. van der Schaar, S. Meyer, S. Morgan, K. Bhattacharyya, G.-T. Huang, C.-M. Ke, and K.-H. Chen, "Sub-nanometer in-die overlay metrology: measurement and simulation at the edge of finiteness," *Proceedings of SPIE*, vol. 8788, pp. 87881N-6, 2013.
- [66] D. Laidler, K. D'havé, A.-L. Charley, P. Leray, S. Cheng, M. Dusa, P. Vanoppen, and P. Hinnen, "A single metrology tool solution for complete exposure tool setup," *Proceedings of SPIE*, vol. 7638, pp. 763809–10, 2010.
- [67] A. C. Assafrao, N. Kumar, A. J. H. Wachters, S. F. Pereira, H. P. Urbach, M. Brun, and S. Olivier, "Application of micro solid immersion lens as probe for near-field scanning microscopy," *Applied Physics Letters*, vol. 104, no. 10, pp. 101 101–101 103, 2014.
- [68] S. M. Mansfield and G. S. Kino, "Solid immersion microscope," Applied Physics Letters, vol. 57, no. 24, pp. 2615–2616, 1990.
- [69] K. A. Serrels, E. Ramsay, P. A. Dalgarno, B. Gerardot, J. O'Connor, R. H. Hadfield, R. Warburton, and D. Reid, "Solid immersion lens applications for nanophotonic devices," *Journal of Nanophotonics*, vol. 2, no. 1, pp. 021854–021854–29, 2008.
- [70] S. B. Ippolito, B. B. Goldberg, and M. S. Ünlü, "Theoretical analysis of numerical aperture increasing lens microscopy," *Journal of Applied Physics*, vol. 97, no. 5, p. 053105, 2005.
- [71] L. P. Ghislain, V. B. Elings, K. B. Crozier, S. R. Manalis, S. C. Minne, K. Wilder, G. S. Kino, and C. F. Quate, "Near-field photolithography with a solid immersion lens," *Applied Physics Letters*, vol. 74, no. 4, pp. 501–503, 1999.
- [72] S. M. Mansfield, W. R. Studenmund, G. S. Kino, and K. Osato, "High-numerical-aperture lens system for optical storage," *Optics Letters*, vol. 18, no. 4, pp. 305–307, 1993.
- [73] G. M. Lerman, A. Israel, and A. Lewis, "Applying solid immersion near-field optics to raman analysis of strained silicon thin films," *Applied Physics Letters*, vol. 89, no. 22, p. 223122, 2006.

[74] F. Zijp, "Near field optical data storage," Ph.D. dissertation, Delft University of Technology, 2007.

- [75] A. Yurt, A. Uyar, T. B. Cilingiroglu, B. B. Goldberg, and M. S. Ünlü, "Evanescent waves in high numerical aperture aplanatic solid immersion microscopy: Effects of forbidden light on subsurface imaging," *Optics Express*, vol. 22, no. 7, pp. 7422–7433, 2014.
- [76] M.-S. Kim, T. Scharf, M. T. Haq, W. Nakagawa, and H. P. Herzig, "Subwavelength-size solid immersion lens," *Optics Letters*, vol. 36, no. 19, pp. 3930–3932, 2011.
- [77] D. A. Fletcher, K. B. Crozier, C. F. Quate, G. S. Kino, K. E. Goodson, D. Simanovskii, and D. V. Palanker, "Near-field infrared imaging with a microfabricated solid immersion lens," *Applied Physics Letters*, vol. 77, no. 14, pp. 2109–2111, 2000.
- [78] T. Knieling, M. Shafi, W. Lang, and W. Benecke, "Microlens array production in a microtechnological dry etch and reflow process for display applications," *Journal of the European Optical Society - Rapid Publications*, vol. 7, no. 0, p. 12007, 2012.
- [79] D. R. Mason, M. V. Jouravlev, and K. S. Kim, "Enhanced resolution beyond the abbe diffraction limit with wavelength-scale solid immersion lenses," *Optics Letters*, vol. 35, no. 12, pp. 2007–2009, 2010.
- [80] M. Brun, S. Mimoumi, S. Nicoletti, P. Poupinet, and H. Moriceau, "Solid immerson lens and related method for making same," U.S. patent, 2010.
- [81] M.-S. Kim, T. Scharf, and H. P. Herzig, "Small-size microlens characterization by multiwavelength high-resolution interference microscopy," *Optics Express*, vol. 18, no. 14, pp. 14319–14329, 2010.
- [82] A. C. Assafrao, M.-S. Kim, A. J. H. Wachters, T. Scharf, H. P. Herzig, S. Olivier, M. Brun, S. F. Pereira, and H. P. Urbach, "Experimental and theoretical investigation on the misalignment tolerance of a micron-sized solid immersion lens," *Journal of Optics*, vol. 15, no. 2, p. 025706, 2013.
- [83] A. Shan, M. Fried, G. Juhasz, C. Major, O. Polgar, A. Nemeth, P. Petrik, L. Dahal, J. Chen, Z. Huang, N. Podraza, and R. Collins, "High-speed imaging/mapping spectroscopic ellipsometry for in-line analysis of roll-to-roll thinfilm photovoltaics," *IEEE Journal of Photovoltaics*, vol. 4, no. 1, 2014.
- [84] P. Petrik, "Ellipsometric models for vertically inhomogeneous composite structures," physica status solidi (a), vol. 205, no. 4, pp. 732–738, 2008.
- [85] J. Endres, N. Kumar, P. Petrik, M. Henn, S. Heidenreich, S. F. Pereira, H. P. Urbach, and B. Bodermann, "Measurement comparison of goniometric scatterometry and coherent Fourier scatterometry," *Proceedings of SPIE*, vol. 9132, pp. 913 208–9, 2014.

[86] S. Roy, N. Kumar, S. F. Pereira, and H. P. Urbach, "Interferometric coherent Fourier scatterometry: a method for obtaining high sensitivity in the optical inverse-grating problem," *Journal of Optics*, vol. 15, no. 7, p. 075707, 2013.

[87] P. Petrik, N. Kumar, M. Fried, B. Fodor, G. Juhasz, S. F. Pereira, and H. P. Urbach, "Fourier ellipsometry: an ellipsometric approach to Fourier scatterometry," *Submitted*, 2014.



Acknowledgements

I am at the doorstep of defending my PhD thesis and earning the title 'doctor', and this moment would not have arrived without the help and cooperation of many people, whom I would like to acknowledge here.

First and foremost, I would like to express profound gratitude to my promoter Prof. Paul Urbach for his valuable supervision, and interesting discussions from which I benefited immensely. I highly appreciate and value his insight in the field of theoretical optics, which has helped to shape the course and output of my research.

I thank Dr. Silvania F Pereira for her constant support and daily supervision throughout my PhD. Her willingness to come to the lab, whenever required was of great help. Her experimental expertise and pro-active approach led to many interesting results and the timely completion of the thesis.

I acknowledge Prof. Wim M. J. Coene for his constructive involvement in the project and the critical discussions during the project meetings. Special thanks to all the committee members for carefully reading the thesis and providing feedback.

I would like to thank Omar El Gawhary for mentoring me in the the initial years of the project, and for his clear and comprehensible explanations of the doubts I had. His approach towards science and his readiness to discuss, help and contribute not only helped me academically, but has also made me a better person. I was fortunate to work with Peter Petrik during the final year of my PhD. I thank him for his encouragement, and for reading and correcting my thesis. I will cherish the time we spent together on the scatterometry research, and hopefully the collaboration will continue!

My sincere thanks to the trio of Roland, Rob and Thim, for software, mechanical and technical lab-issues. They quickly understood the problem and helped to find the solutions at the earliest, which has been of great value to me. Yvonne, I cannot have survived here, if not your constant help for the entire duration of my stay in Delft. Whether it was an issue with residence permit, visa or salary payment, you were always there standing behind to solve those. A big Thank you!

I was lucky enough to get a chance to work with some really talented and fun

loving people in the lab. Axel, thank you for teaching few tricks of experimental optics in the lab and your readiness to help even after leaving the group. Sander, Luca, Emilien and Luiz, thank you for the good times and the lessons we learnt about the SLM in the lab. It was also fun working with Sarathi and Alberto. Thank you for being good friends!

I acknowledge the patience and kindness of Prof. Joseph Braat, who always lend an ear to listen to our research problems. I thank Nandini for her continuous support, encouragement and friendship. I thank Aurèle for the fun times and the social activities in Optica. I also acknowledge Florian Bociort and Prof. Paul Planken for the academic discussions.

I cherish the time spent with Wouter and Adonis as office-mates for so long. Thank you guys! Our discussions in the office on the academic and non-academic matters were extremely necessary to get through our PhD life. Wouter, it was an honour to be your paranymph during your thesis defense. Also, I am thankful to Adonis and Luca for being ready to be my paranymphs during the defense ceremony. I place special thanks to Sander for translating the summary. I also thank Peter Somers for his willingness to help and for scrutinizing the samenvatting.

I thank Lei Wei for some intense academic discussion and his funny one liners (after a beer, and if you can understand it) was absolutely hilarious. Andreas Hänsel and Luca Cisotto: It is absolute fun to spend time with both of you, and I enjoyed very much all the dinner events and movie times. I thank Edgar for the warm friendship with us. Pura Vida, Mae! Nishant has been the first I would approach for any kind of help for the past few years. Thank you for everything, especially the help to submit my PROM forms and dealing successfully the appointment problems with the beadle.

I acknowledge the friendship and the good relations I built in Optica with Morris, Gopakumar, Mounir, Alessandro, Gerward, Kate, Mahsa, Nick Schilder, Yifeng, Jeff, Hamed, Zhe, Olaf, Marco, Daniel, Ying, Matthias and others. I thank for the comforting environment, when I joined Optica to Reshmi, Olaf, Aura, Pascal and Sven. I thank José-Luis, Manish, Arnab and Mani for being wonderful friends, even from a distance. I am extremely grateful to Ma'am and Sir for their kindness and encouragement.

At the end, I would like to specially thank my parents, Bhaiya and Bhabhi for their limitless confidence in me. Without their inspiration, support and encouragement, I would not have been able to achieve whatever I have achieved. Thank you for what you have done for me to understand myself and moreover to make me an honest and good human being. I also thank Achan and Amma, Malu and Muthu, and Paro for the love and care. Last but not least I thank my loving wife Gopika for her support, understanding and commitment.

Nitish Kumar, December 2014



About the Author

Nitish Kumar was born in Patna, India. In 2008, he completed a five-year integrated MSc degree in Photonics at the Center of Excellence in Lasers and Optoelectronic Sciences, Cochin University of Science and Technology, India. His master thesis was on the "Interferometric and elasto-optic tomography for 3D phase reconstruction" for which he worked at Warsaw University of Technology, Warsaw, Poland. In 2008, he was awarded the Erasmus Mundus scholarship for dual Master degree course in *OpSciTech* program, of which he spent his first year in Warsaw, Poland and then the second year in Delft, the Netherlands, where he



worked on Fourier scatterometry and phase retrieval. He graduated with *Master in Automatics and Robotics specialized in Photonics Engineering* from Warsaw University of Technology, Warsaw, Poland and as *Master of Science in Applied Physics* from Delft University of Technology, Delft, The Netherlands.

Subsequently in 2010, he joined PhD program at the Optics Research Group in Delft, partially funded by the European project called **S**urface **P**hysics for **A**dvanced **M**anufacturing (S. P. A. M) within FP7 Marie-Curie research and initial training program and by ASML, The Netherlands. He was awarded the SPIE educational scholarship in 2008. His research work has been presented at several international conferences and published in conference proceedings and peer-reviewed journals.

He is currently working at ASML research in Sensors, Metrology and Control group in the Netherlands.

Peer Reviewed Journal Publications

N. Kumar, P. Petrik, G. KP Ramanandan, O. El Gawhary, S. Roy, S. F. Pereira, W. M. J. Coene, H. P. Urbach Reconstruction of sub-wavelength features and nano-positioning of gratings using coherent Fourier scatterometry, Optics Express 22 (20), 24678-24688 (2014)

N. Kumar, O. El Gawhary, S. Roy, S. F. Pereira, H. P. Urbach *Phase retrieval between overlapping orders in coherent Fourier scatterometry using scanning*, Journal of European Optical Society Rapid Publications, **8**, 13048 (2013)

- N. Kumar, W. M. J. Coene, H. P. Urbach Overlay analysis with coherent Fourier scatterometry (manuscript in preparation)
- N. Kumar, P. Petrik, S. F. Pereira, H. P. Urbach Effect of unintentional surface layers in grating reconstruction with coherent Fourier scatterometry (manuscript submitted)
- N. Kumar, L. Cisotto, S. Roy, S. F. Pereira, H. P. Urbach Determination of complete scattering matrix with interferometric coherent Fourier scatterometry (manuscript in preparation)
- P. Petrik, N. Kumar, M. Fried, B. Fodor, G. Juhasz, S. F. Pereira, H. P. Urbach Fourier ellipsometry: an ellipsometric approach to Fourier scatterometry (manuscript submitted)
- S. Roy, N. Kumar, S. F. Pereira, H. P. Urbach Interferometric coherent Fourier scatterometry: a method for obtaining high sensitivity in the optical inverse-grating problem Journal of Optics, 15, 075707 (2013)
- S. Roy, O. El Gawhary, N. Kumar, S. F. Pereira, H. P. Urbach Scanning effects in coherent Fourier scatterometry, Journal of European Optical Society Rapid Publications, 7, 12031 (2012)
- O. El Gawhary, A. Wiegmann, N. Kumar, S. F. Pereira, H. P. Urbach *Through-focus phase retrieval and its connection to the spatial correlation for propagating fields* Optics Express **21** (5), 5550-5560 (2013)
- A P. Konijnenberg, L. Wei, N. Kumar, L. CCP Filho, L. Cisotto, S. F. Pereira, H. P. Urbach Demonstration of an optimised focal field with long focal depth and high transmission obtained with the Extended Nijboer-Zernike theory, Optics Express 22 (1), 311-324 (2014)
- A.C. Assafrao, N. Kumar, S. F. Pereira, H. P. Urbach Application of micro solid immersion lens as probe for near-field scanning microscopy, Applied Physics Letters 104, 101101 (2014)
- A.C. Assafrao, N. Kumar, A. J. H. Wachters, S. F. Pereira, H. P. Urbach *Experimental and numerical analysis of the super resolution near-field effect on an InSb sample*, Japanese Journal of Applied Physics, **53**, 04 (2014)
- T. Kozacki, R. Krajewski, M. Kujawinska, N. Kumar, H. Thienpont Studies on polymer optical microstructures refractive index distribution by means of interferometric tomography system, Przeglad Elektrotechniczny, 84 (05), 161-164 (2008)

Conference Proceedings

- N. Kumar, O. El Gawhary, S. Roy, V. G. Kutchoukov, S. F. Pereira, W. Coene, H. P. Urbach Coherent Fourier scatterometry: tool for improved sensitivity in semiconductor metrology, Proceedings of SPIE 8324, 83240Q (2012)
- S. F. Pereira, A. Wiegmann, N. Kumar, A. da Costa Assafrao, A. Polo, L. Wei, S. van Haver Experimental techniques for aberration retrieval with through focus intensity images, Proceedings of SPIE 8557, 855706 (2012)
- A. Wiegmann, S. van Haver, N. Kumar, S.F. Pereira Experimental Validation of the Extended-Nijboer-Zernike (ENZ) based Aberration Retrieval Method for Microscope Objectives, DGAO proceedings (2012)

N. Kumar, O. El Gawhary, S. Roy, S. F. Pereira, H. P. Urbach *Phase information in coherent Fourier scatterometry*, Proceedings of SPIE 8788, 87881P (2013)

- N. Kumar, S. Roy, O. El Gawhary, S. F. Pereira, W. M. J. Coene, H. P. Urbach Towards Grating Reconstruction in Coherent Fourier Scatterometry, Fringe, 591-594 (2013)
- S. Roy, N. Kumar, S. F. Pereira, H. P. Urbach Lowering the cross correlation between different shape parameters of the inverse grating problem in coherent Fourier scatterometry, Fringe, 43-38 (2013)
- J. Endres, N. Kumar, P. Petrik, S. Heidenreich, S. F. Pereira, H. P. Urbach, B. Bodermann Measurement comparison of goniometric scatterometry and coherent Fourier scatterometry, Proceedings of SPIE 9132, 913208 (2014)
- P. Petrik, N. Kumar, E. Agocs, B. Fodor, S. F. Pereira, T. Lohner, M. Fried, H. P. Urbach Optical characterization of laterally and vertically structured oxides and semiconductors, Proceedings of SPIE 8987, 89870E (2014)
- S. Mavila, T. K. Jhony, R. Mandamparambil, N. Kumar, P. A. Cheriyan, V. P. N. Nampoori, R. Padmanabhan, *Laser emission from dye mixture doped polymer optical fiber*, proceedings of SPIE, 6698, 66981O(2007)
- N Kumar, M Kujawinska, P Kniazewski, 3D investigation of photonics elements by means of interferometric and photoelastic tomography, Proceedings of SPIE 7155, 71551Q (2008)
- M. Kujawinska, R. Krajewski, N. Kumar, J. Mohr, H. Thienpont Tomographic studies of 3D refractive index and birefringence distribution in M-O elements replicated by hot embossing technology, Proceedings of SPIE 7064, 70640H (2008)
- M. Kujawiska, N. Kumar, A. Michalkiewicz Digital phase shifting holography and holographic interferometry, Fringe, 1-7 (2009)

Conference Contributions

- N. Kumar, O. El Gawhary, S. F. Pereira, W. Coene, H. P. Urbach Coherent Fourier Scatterometry (CFS): A new way to achieve high accuracy in lithography inspection, 37th International Conference on Micro and Nano Engineering, 19 - 23 September, Berlin, Germany (2011)
- N. Kumar, O. El Gawhary, S. Roy, V. G. Kutchoukov, S. F. Pereira, W. Coene, H.P. Urbach Coherent Fourier scatterometry: tool for improved sensitivity in semiconductor metrologys, SPIE Advanced Lithography, 12 16 February, San Jose, USA (2012)
- N. Kumar, O. El Gawhary, S. Roy, S. F. Pereira, W. M. J. Coene, H. P. Urbach *Performance analysis of Coherent Fourier Scatterometry in semiconductor metrology*, 13th ASML Technology Conference, June 21, Veldhoven, Netherlands (2012)
- O. El Gawhary, A. Wiegmann, N. Kumar, S.F. Pereira, H.P. Urbach Spatial correlation for propagated fields and the phase problem, 8th EOS Topical Meeting on Diffractive Optics, 27 February 1 March, Delft, Netherlands (2012)
- N. Kumar, O. El Gawhary, S.F. Pereira, W. Coene, H.P. Urbach Semiconductor metrology with inverse diffraction approach Coherent Fourier Scatterometry, 8th EOS Topical Meeting on Diffractive Optics, 27 February 1 March, Delft, Netherlands (2012)
- N. Kumar, S. Roy, O. El Gawhary, S. F. Pereira, H. P. Urbach Analytic Phase retrieval in Coherent Fourier Scatterometry from the far field intensity maps, EOSAM, 25 28 September, Aberdeen, Scotland (2012)

S. Roy, N. Kumar, S. F. Pereira, H. P. Urbach *Polarization Effects in Coherent Fourier Scatterometry*, EOSAM 2012, 25 - 28 September, Aberdeen, Scotland (2012)

- N. Kumar, O. El Gawhary, S. Roy, S. F. Pereira, H. P. Urbach *Phase information in coherent Fourier scatterometry*, SPIE Optical Metrology, 1316 May, Munich, Germany (2013)
- N. Kumar, P. Petrik, S. F. Pereira, H. P. Urbach Influence of unintentional surface layers on the grating characterization in coherent Fourier scatterometry, 8th Workshop Ellipsometry, 1012 March, Dresden, Germany (2014)
- N. Kumar, P. Petrik, L. Cissoto, S. Roy, S. F. Pereira, H. P. Urbach Solving inverse problems in scatterometry for grating reconstruction in semiconductor metrology, EOSAM 2014, 15-19 September, Berlin, Germany (2014)
- S. F. Pereira, A. da Costa Assafrao, N. Kumar, H. P. Urbach Application of micro solid immersion lens as probe for near-field scanning microscopy, EOSAM 2014, 15-19 September, Berlin, Germany (2014)
- P. Petrik, N. Kumar, M. Fried, B. Fodor, G. Juhasz, S. F. Pereira, H. P. Urbach Fourier ellipsometry-phase retrieval in Fourier scatterometry using polarization modulation, EOSAM 2014, 15-19 September, Berlin, Germany (2014)
- A P. Konijnenberg, L. Wei, N. Kumar, L. Cisotto, S. F. Pereira, H.P. Urbach Demonstration of optimised focal field with long focal depth and high transmission obtained with extended Nijboer-Zernike theory, EOSAM 2014, 15-19 September, Berlin, Germany (2014)